OPTICAL CHARACTERIZATION OF WIDE-BAND GAP BULK CRYSTALS AND EPITAXIAL LAYERS

by

Madhu H. Gowda
A Dissertation
Submitted to the
Graduate Faculty
of
George Mason University
In Partial fulfillment of
The Requirements for the Degree
of
Doctor of Philosophy
Electrical and Computer Engineering

Committee:

Dr. Mulpuri V. Rao, Dissertation Director

Dr. Alok K. Berry, Committee Member

Dr. William G. Sutton, Committee Member

Dr. Yuri Mishin, Committee Member

Dr. Jaime A. Fretias Jr., Committee Member

Dr. Andrzej Z. Manitius, Department Chair

Dr. Lloyd J. Griffiths, Dean, The Volgenau School of Information Technology and Engineering

Date: OCTOBER 1st 2008

Fall Semester 2008
George Mason University
Fairfax, VA

Optical Characterization of Wide-band gap Bulk crystals and Epitaxial layers

A dissertation submitted in partial fulfillment of the requirements for the degree of Doctor of Philosophy at George Mason University

By

Madhu H. Gowda
Master of Science
Tuskegee University, 2005

Director: Mulpuri, V. Rao, Professor
Department of Electrical and Computer Engineering

Fall Semester 2008
George Mason University
Fairfax, VA

Copyright 2008 Madhu H. Gowda
All Rights Reserved

DEDICATION

This dissertation is dedicated to my parents, Dr. Hanume Gowda and Mrs. Leela Manjula for their love, affection and encouragement.

ACKNOWLEDGEMENTS

To quote Henry Adams, "A teacher affects eternity; he can never tell, where his influence stops." I consider myself to be one among the fortunate few, to stumble upon numerous individuals who have had a tremendously positively influence on me in the last few years, inspiring, motivating and teaching me the nuances of scientific research and, life in general in leading by example.

As a graduate student during my Masters program, the thoughts of pursuing a doctoral program, would cross my mind often, which; I would instantaneously dismiss, as something beyond my reach. The motivation and encouragement provided by Dr. Mulpuri V. Rao convinced me to undertake this journey in my academic career, which, I now feel has been the most satisfying and, also a prominent milestone in my life; not just academics. I sincerely thank Dr. Rao for motivating me to join the doctoral program.

Dr. Jaime A. Freitas, who as my mentor taught me more than I could ever give him credit for here. In him, I have observed numerous qualities of a good scientist (and person), which have left a lasting impression on me, which I wish to emulate in future.

I express my deepest thanks to other members on my Dissertation Committee, Dr. Alok Berry, Dr. William Sutton, and Dr. Yuri Mishin.I would like to extend my thanks to Dr. B.N. Feigelson (NRL), Dr. R.M. Frazier (NRL), Dr. S. Maximenko (NRL), Dr. J. –H. Kim (NRL), Dr. J.G. Tischler (NRL), Dr. C. Eddy (NRL), Dr. Y.-L. Tian (LT), M.A. Mahadik (GMU), Dr. S.G. Sundaresan (GMU), and G. Aluri (GMU) for their help and support in various stages of my dissertation.

Deepest appreciation goes to my parents for their love throughout the journey of my life. I would like to thank my mother, who always had an ear to listen to my frustrations and joys. I am grateful to my father, who instilled within me with his own example, the importance of hard work and a good education. I thank my brother and sister-in-law for patiently listening to my "Ph.D. woes" for years, with a smile and, my little nephew and niece for reminding me what "never ending enthusiasm" and "perseverance" is, through their "unknowingly profound" actions. In addition, I would like to thank Jayashree and Rajagopal for their constant support during the completion of my Ph.D.

In conclusion, I recognize that this research would not have been possible without the financial assistance of National Science Foundation # ECS-0330226 .

TABLE OF CONTENTS

	Page
List of Tables	vii
List of Figures	viii
Abstract	xii
1. INTRODUCTION	1
1.1 Importance of Wide bandgap materials	1
1.2 Existing issues with Gallium nitride	3
1.3 Existing issues with Silicon carbide	5
1.4 Optical Characterization	6
1.4.1 Photoluminescence Spectroscopy	10
1.2.2 Photoluminescence Imaging	12
1.5 Objective of this work	15
1.5 Thesis Organization	16
2. CHARACTERIZATION OF BULK GALLIUM NITRIDE	17
2.1 Semi-insulating Fe-doped GaN substrate grown from HVPE method	17
2.1.1 Experimental Details	18
2.1.2 Experimental Results and Discussion	20
2.1.2.1 X-ray Characterization	20
2.1.2.2 Photoluminescence Imaging	21
2.1.2.3 Photoluminescence Spectroscopy	23
2.1.2.4 Electrical Characterization	29
2.1.2.5 Summary	30
2.2. Bulk GaN crystals grown from solution at moderate pressure and temperature	31
2.2.1 Growth technique and sample information	33
2.2.2 Experimental Results and Discussion	35
2.2.3 Summary	53
3. CHARACTERIZATION OF *n*-TYPE GALLIUM NITRIDE FILMS	55
3.1 Experimental samples and approach	56
3.2 Surface morphology of a UID and Si-doped GaN	59
3.3 Secondary ion mass Spectrometry	60
3.4 Photoluminescence Spectroscopy	64
3.5 Summary	69
4. CHARACTERIZATION OF *p*-TYPE GALLIUM NITRIDE FILMS	70
4.1 Study of Mg-doped GaN homoepitaxial layers grown by MBE	70
4.1.1 Experimental Details	72
4.1.2 Photoluminescence Spectroscopy	73

4.1.3 Optical detected magnetic resonance 77
4.1.4 Summary 81
4.2 Microwave annealing of *in-situ* Mg doped GaN films grown by MOCVD 82
4.2.1 Experimental Details 83
4.2.2 X-Ray Photoelectron Spectroscopy 85
4.2.3 Structural characterization of microwave annealed samples 86
4.2.4 Optical Characterization 89
4.2.5 Electrical Characterization 93
4.2.6 Summary 94
4.3 Microwave annealing of *in-situ* Be doped GaN films grown by MBE 96
4.3.1 Experimental Details 96
4.3.2 X-Ray Photoelectron Spectroscopy 97
4.3.3 Secondary ion mass spectrometry 98
4.3.4 Optical Characterization 101
4.3.5 Summary 103
4.4 Microwave annealing of Mg-implanted GaN films grown on sapphire 104
4.4.1 Experimental Details 104
4.4.2 X-Ray Photoelectron Spectroscopy 105
4.4.3 Secondary ion mass spectrometry 106
4.4.4 Atomic Force Microscopy 108
4.4.5 X-Ray Diffraction and rocking curve measurements 109
4.4.6 Optical Characterization 110
4.4.7 Electrical Characterization 114
4.4.8 Summary 115
5. NONDESTRUCTIVE CHARACTERIZATION OF DISLOCATIONS AND MICROPIPES IN 4H-SiC USING PHOTOLUMINESCENCE IMAGING 116
5.1 Experimental Details 117
5.2 Results and Discussion 118
5.3 Summary 131
6. CONCLUSIONS AND FUTURE WORK 132
6.1 Conclusions 132
6.2 Future work 134
7. Appendices 135

LIST OF TABLES

Table Page
Table I: Comparison of the material properties of inorganic semiconductors..................... 2
Table II: SIMS data on OMVPE GaN film grown on HVPE- FS GaN substrate showing the concentration (cm^{-3}) of Si, O and C in the substrate and in the film...... 62
Table III: SIMS data of UID- MBE GaN film grown on HVPE-FS GaN substrate with concentrations (cm^{-3}) of Si, O and C in the substrate and in film....................... 63
Table IV: Multiple energy Mg implant schedule perfomed on undoped GaN............... 105

LIST OF FIGURES

Figure Page

Figure 1: Figure 1. E-k diagrams for: (a) Direct bandgap semiconductor; (b) Indirect bandgap Semiconductor 7
Figure 2: Schematic diagram of radiative transitions between the conduction band (EC), the valence band (EV) and exciton (EE), donor (ED) and acceptor (EA) levels in a semiconductor 8
Figure 3: A schematic of the photoluminescence spectroscopic set-up 11
Figure 4: A schematic of the photoluminescence imaging set-up 13
Figure 5: A schematic of photoluminescence imaging set-up having an inverted microscope 14
Figure 6: XRD spectrum of one of the Fe-doped thick freestanding GaN substrate 20
Figure 7: (a) RGB PL imaging of UID GaN film grown on AlN/Sapphire template. (b) Panchromatic PL imaging of the sample shown in (a). The inserts (1) and (2) shows the SEM/ CL and SEM/imaging of the region highlighted in 2(a), respectively 22
Figure 8: (a) RGB PL imaging of a Fe-doped GaN substrate. (b) Panchromatic PL imaging of the sample represented in (a). Note the bright "palm tree leaves" shape defects 23
Figure 9: Low-resolution and low temperature PL spectra of undoped and iron doped samples. Note the reduction of all luminescence bands in the iron doped samples ... 25
Figure 10: High-resolution and low temperature PL spectra of the samples represented in Figure 9, in the near band-edge spectral region 26
Figure 11: Low temperature NIR-PL spectra of the two Fe-doped samples. The intense emission line at 1.299 eV is related to substitutional Fe impurities 28
Figure 12: Fe-doped GaN resistivity as a function of 1000/T as determined by Hall Effect measurements 29
Figure 13: A schematics of the technical approach to GaN growth from solution 32
Figure 14: A schematic of the solution based growth reactor 34
Figure 15: LT PL spectra of spontaneously-nucleated GaN crystal (sample I) 35
Figure 16: High-resolution PL spectra of spontaneously-nucleated GaN crystal (sample I) 38

Figure 17: Schematic view and optical images of (a) the crucible with GaN source, solvent and HVPE GaN polycrystalline aggregate as seed, (b) the seed - HVPE GaN polycrystalline aggregate before growth run, (c) the seed - HVPE GaN polycrystalline aggregate after growth run with grown GaN crystals, (d) and (e) zoomed images of the crystals shown on the Figure 17(c), arrow indicates m direction 40
Figure 18: XRD rocking curve of the (0004) reflection for the GaN crystal grown on the polycrystalline GaN seed 41
Figure 19: Room temperature micro-Raman spectrum of the GaN crystal grown on the polycrystalline GaN seed in the backscatter geometry 43
Figure 20: LT PL spectra of a HVPE GaN polycrystalline aggregate crystal seed (substrate) and the seed grown crystal (sample II) 44
Figure 21: High-resolution PL spectra of grown crystal on HVPE GaN polycrystalline aggregate crystal seed (sample II) 45
Figure 22: Photographic images of the HVPE GaN template used as a seed with epitaxially grown GaN layer (a) nitrogen face, (b) gallium face 47
Figure 23: Omega-2theta space map of the symmetric (0004) reflection for the (a) as-received GaN seed and (b) Ga-face of the GaN grown crystal 48
Figure 24: Cross-sectional Raman spectrum of homoepitaxial GaN layer (sample III) . 49
Figure 25: LT PL spectra of homoepitaxial GaN layer (sample III) 51
Figure 26: High-resolution PL spectra of homoepitaxial GaN layer (sample III) 52
Figure 27: Low temperature high-resolution PL spectra of the two typical HVPE substrates, which were subjected to epi-growth processes 59
Figure 28: AFM of UID GaN deposited on FS-HVPE GaN substrate by MBE technique 60
Figure 29: SIMS depth profiles of the GaN homoepitaxial film grown by OMVPE on FS- HVPE GaN substrate (Si: OMVPE/HVPE-FS) 61
Figure 30: SIMS depth profiles of the homoepitaxial film deposited on a FS-HVPE GaN substrate by RF-plasma-assisted MBE technique (UID-O:MBE/HVPE-FS) 63
Figure 31: Low temperature PL spectra of the Si-doped OMVPE (Si: OMVPE/HVPE-FS) and the UID MBE (UID-O: MBE/HVPE-FS) homoepitaxial GaN films. The spectrum of an HVPE-FS GaN reference substrate is also shown 66
Figure 32: Spectra taken at 5K in the 2ES region of all three samples 67
Figure 33: PL spectrum of the Si: OMVPE/HVPE-FS GaN sample showing the A^0X intensity dependence with power excitation 68
Figure 34: High-resolution PL at 5K in the bandgap region from two Mg-doped GaN homoepitaxial films and one undoped GaN homoepitaxial reference layer. The spectra are displaced vertically for clarity 74
Figure 35: PL (< 3.4 eV) recorded at 2K from several Mg-doped GaN homoepitaxial layers. 76

Figure 36: ODMR spectra at 24 GHz observed on the 3.27 eV SD-SA PL from a homoepitaxial GaN layer doped with [Mg] of 1 x 10^{17} cm^{-3} for several orientations of **B** with respect to the c-axis ... 78
Figure 37: g-values of ODMR feature Mg_{Ga} in this work (triangles) and those reported previously for shallow acceptors in Si-doped GaN homoepitaxial layers (circles) and for Mg shallow acceptors in Mg-doped GaN heteroepitaxial films (squares). Dashed curves are fits to the data as described in the text ... 80
Figure 38: XPS survey scans of: (a) AlN as-capped GaN sample, (b) AlN capped sample after 1400 °C/5 s annealing, and (c) after removal of the AlN cap at the conclusion of annealing ... 86
Figure 39: Tapping mode AFM images of: (a) an as-grown GaN surface (RMS roughness = 0.3 nm); after 1300 ºC / 5 s microwave annealing of GaN layers with (b) no cap (RMS roughness = 9.2 nm), (c) MgO cap (RMS roughness = 0.8 nm), and (d) AlN cap (RMS roughness = 1 nm); (e) after 1400 ºC / 5 annealing with MgO cap (RMS roughness = 7.2 nm); and (f) after 1500 ºC/5 s annealing with AlN cap (RMS roughness = 0.6 nm) ... 88
Figure 40: Low-temperature (5 K) PL spectra of as-grown Mg:GaN on sapphire; and of AlN capped samples subjected to 5 s microwave annealing at 1300 ºC and 1500 ºC ... 91
Figure 41: Low-temperature (5 K) PL spectra of as-grown Mg:GaN on sapphire; and of MgO capped Mg-doped GaN samples after 5 s microwave annealing at 1300 ºC and 1350 ºC ... 92
Figure 42: Hole concentration (*p*) as a function of annealing temperature for 5 s duration microwave annealing on uncapped, MgO capped, and AlN capped in-situ Mg-doped MOCVD-GaN ... 94
Figure 43: XPS of Be in-situ doped GaN films after AlN cap (a) unannealed, and (b) annealed at 1400 ^{0}C/5s ... 97
Figure 44: SIMS results of the Be doped GaN films (a) before annealing, and after (b) 1300 ºC /5 s, (c) 1400 ºC / 5 s, and (d) 1500 ºC / 5 s microwave annealing ... 100
Figure 45: Low-temperature (5 K) PL spectra from an un-implanted GaN epilayer, and GaN epilayers before and after 1300 ºC / 5 s ,1400 ºC / 5 s, 1500 ºC / 5 s and 1600 ºC / 5 s microwave annealing ... 102
Figure 46: XPS survey scans of: (a) Mg: GaN sample annealed at 1400 ºC/15 s , and (b) Mg:GaN sample annealed at 1500 ºC/15 s ... 106
Figure 47: SIMS depth profiles of the Mg implanted GaN before and after 1300 ºC /5 s and 1400 ºC / 5 s microwave annealing ... 107
Figure 48: Tapping mode AFM images Mg:GaN of: (a) after 1300 0C/15s annealing (RMS roughness = 3.387 nm), and (b) after 1500 0C/15s annealing (RMS roughness = 9.724 nm) ... 108
Figure 49: XRD scans of the GaN (004) as-implanted and microwave annealed films ... 109
Figure 50: XRD scans of the GaN (104) as-implanted and microwave annealed films ... 110
Figure 51: Low-temperature (5 K) PL spectra from an un-implanted GaN epilayer, and multiple energy Mg implanted GaN epilayers before and after 1400 ºC / 5 s and 1500 ºC / 5 s microwave annealing ... 112

Figure 52: Low-temperature (5 K) PL spectra of as-implanted (unannealed) and annealed Mg-implanted GaN for 15s annealing at 1300 ^{0}C, 1400 ^{0}C, and 1500 ^{0}C 114
Figure 53: Comparison of the (a) photographic image of the 3-inch wafer and (b) PL panchromatic image. The overall distribution of defects is clearly seen in the panchromatic PL image 118
Figure 54: Comparison between PL image and SWBXT. (a) RGB PL image of a 3’’ SiC wafer discussed in Fig. 53; (b) (11-2.12) grazing-incidence SWBXT of the same wafer. (c) PL image of another 3-inch wafer and the corresponding (d) SWBXT 120
Figure 55: A higher magnification PL image (a) showing the detailed low angle grain boundary configuration and the (b) SWBXT image corresponding to the same area 121
Figure 56: Higher magnification (a) Gray scale and (b) Green PL images of a polycrystalline region, which have shown high concentration of micropipes and micro-crystallites 122
Figure 57: Higher magnification RGB-PL images of a thick 4H-SiC homoepitaxial layer showing the presence of individual SF, BPD, and micropipes 123
Figure 58: Large area real-color PL imaging of Schottky devices on SiC showing (a) front side and (b) backside 124
Figure 59: Large area real-color PL imaging (cont.) of defects distribution in device surrounding area taken at front surface 125
Figure 60: RGB PL imaging of individual devices (after removing the contacts) 126
Figure 61: PL imaging of device A102-2 after removing the metal contacts 127
Figure 62: SEM, EBIC and CCL of device A102-2 with metal contacts 128
Figure 63: CCL of device A102-2 after removing the metal contacts) 129
Figure 64: Current-voltage (I-V) characterizations of the selected devices.......................... 130

ABSTRACT

OPTICAL CHARACTERIZATION OF WIDE-BAND GAP BULK CRYSTALS AND EPITAXIAL LAYERS

Madhu H. Gowda, Ph.D.

George Mason University, 2008

Dissertation Director: Prof. Mulpuri, V. Rao

This dissertation describes the non-destructive optical characterization of undoped/doped GaN and SiC bulk crystals and epitaxial layers. These materials have applications for optoelectronic devices that are operational in the UV to green regions of the spectrum and also for electronic devices operating at high-temperature, high-frequency and high-power. The primary tool used for the characterization of GaN is low temperature photoluminescence (PL) spectroscopy and for the characterization of SiC is photoluminescence imaging. Non-optical characterization techniques such as secondary ion mass spectrometry (SIMS), X-ray diffraction, Raman spectroscopy, etc., were also used to support the results obtained from optical characterization techniques.

In this thesis work, bulk GaN substrates: (1) grown by hydride vapor phase epitaxy (HVPE) method and (2) grown from solution at moderate temperature and pressure (SMTP) were used. Thick iron doped GaN substrate grown by HVPE showed no

evident degradation in material properties due to iron doping, when compared to the thick unintentionally doped GaN substrate grown by the same method. Low temperature PL measurements performed on GaN crystals grown by SMTP at 800 ^{0}C and 0.25 MPa showed relatively sharp and intense exciton peaks, indicating good crystalline quality. Also, the good crystalline quality of these GaN crystals were verified using room temperature X-Ray diffraction and Raman scattering spectroscopy measurements. In addition, the low free carrier concentration was verified by Raman scattering spectroscopy measurements.

Low-temperature PL studies were also carried out on unintentionally doped and Si-doped homoepitaxial films grown by molecular beam epitaxy (MBE) and metalorganic chemical vapor deposition (MOCVD) methods, respectively, to confirm the identification of O and Si as the dominant shallow donors in GaN films. Based on the PL spectroscopy, the intense peaks at 3.4716 eV and 3.4723 eV are associated with the neutral O and Si donors, respectively. Also the chemical nature of these background impurities and dopants were verified using high sensitivity secondary ion mass spectrometry.

High-resolution PL experiments carried out at 5K on a series of MBE grown Mg-doped (10^{17} – 10^{20} cm^{-3}) GaN homoepitaxial layers revealed intense bandedge emission with narrow linewidth (0.2-0.4 meV), attributed to annihilation of excitons bound to shallow Mg acceptors. Optically detected magnetic resonance study of the emission from a sample doped with [Mg] of 10^{17} cm^{-3} revealed the first evidence of highly anisotropic *g*-tensor ($g_{\|}$ ~2.19, $g_{\perp}$ ~0) for Mg shallow acceptors in wurtzite GaN.

PL characterization was performed on in-situ (Mg and Be) doped and Mg ion-implantation doped GaN films. These films were subjected to microwave annealing, in the temperature range of 1300 ^{0}C - 1600 ^{0}C for a duration of 5 s/15 s, to activate the impurities. Different caps (AlN and MgO) were employed to protect to the GaN surface during annealing. In case of in-situ Mg doped GaN, AlN caps were more effective as compared to MgO caps. Low temperature PL spectra and Hall measurements performed on the Mg in-situ doped or Mg ion-implanted GaN samples indicated that the 5-15s duration microwave annealing at 1500 ^{0}C is more effective in activating Mg acceptors than 1300 ^{0}C microwave annealing. The microwave annealing performed on in-situ Be doped GaN samples showed pronounced Be out- and in- diffusion with increasing annealing temperature.

Real color (Red/Green/Blue) and monochromatic PL imaging experiments were performed on 4H-SiC wafers to investigate the potential of PL imaging technique in identifying sub-micron and microscopic size defects in commercial wafers. PL imaging results are compared with grazing-incidence synchrotron white beam X-ray topography (SWBXT), secondary electron microscopy in combination with electron beam induced current and color cathodoluminescence. PL images of low angle grain boundaries correlate well with SWBXT images. This validation indicates that the PL imaging technique provides a rapid way of detecting low angle grain boundary structures in large-scale SiC wafers. The PL imaging was also performed on device structures to correlate device current-voltage characteristics with defects in the device area.

1. INTRODUCTION

1.1 Importance of Wide bandgap materials

Wide bandgap semiconductors exhibit a unique combination of physical and chemical properties [1,2] that allows the formation of alloys and heterostructures that have become increasingly important for the fabrication of optical devices for full color displays, white light illumination, UV/deep UV light sources, and blue-violet laser diodes for high density DVDs [3]. Similarly wide bandgap semiconductors play a major role in the electronic industry due to its capability to work at high power and high frequency, and/or under extreme environmental conditions.

The wide bandgap semiconductors considered for this study are Silicon Carbide (SiC), and Gallium Nitride (GaN). The energy gaps of these semiconductors in comparison with other inorganic semiconductors are given in Table I.

Table I: Comparison of the material properties of inorganic semiconductors [4].

Inorganic solids	Type	Energy gap (300 K) (eV)	Melting point (K)	Electron mobility (cm^2/ V-s)	Hole mobility (cm^2/ V-s)	Breakdown electric field (V/cm)	Thermal conductivity (W/cmK)	Lattice constant (Å)
Si	Indirect	1.12	1685	1350	470	6×10^5	1.5	5.431
4H-SiC	Indirect	3.26	2700	6000	120*	3.5×10^6	0.46	a=3.073, c=10.053
GaAs	Direct	1.42	1510	800	400	6.5×10^5	3.5	5.653
GaN (wz)	Direct	3.36	1500	1500	30	3.5×10^6	1.7	a=3.189, c=5.185

*Reference [5]

Gallium nitride (GaN) is a stable compound and exhibits significant hardness. Its chemical stability combined with its hardness makes GaN an attractive material for protective coatings [1]. Moreover, it is environmentally friendly and is resistive to harsh environments. Nitride semiconductors (GaN, AlN, AlGaN, InGaN, etc) have seen enormous success in a wide-range of applications encompassing green, blue, violet, and ultraviolet (UV) emitters and detectors, and high power amplifiers. Like GaN, Silicon Carbide (SiC) is also a wide bandgap semiconductor material, which has received attention due to technological interest in devices operating at high-temperatures, high-powers, high frequencies and in harsh environments [2]. Due to a strong Si-C bonding energy, SiC has high chemical stability and mechanical strength. Also SiC *pn* junctions are used for fabricating blue LEDs operating in the 460-470 nm wavelength ranges. Due to the above mentioned electronic applications, SiC technology has rapidly advanced in the past 10 years. Because of its near match lattice constant and thermal expansion co-efficient, SiC have been employed as substrate for templates used to fabricate of optical and microwave devices.

1.2 Existing issues with Gallium nitride

While nitride devices have enjoyed much success, many of the basic problems, which are given below, still remain. It is necessary to find permanent solutions to these problems so that nitride device technology may continue to prosper.

a. Lack of a suitable substrate: One of the largest stumbling blocks in GaN film growth has been the lack of bulk substrates for homoepitaxial growth. Researchers have been forced to use alterative foreign substrates since there is no well established growth technology for synthesize of high quality bulk GaN. Unfortunately, there is no substrate available that is physically and thermally matched to GaN. Hence, GaN has been grown heteroepitaxially on a wide variety of substrates like Si, NaCl, GaP, InP, ZnO, GaAs, SiC and Al_2O_3[6]. Most common substrate has been Al_2O_3 due to its wide availability, ease of cleaning and handling, and stability at high temperatures.

b. High background electron density: Recent studies have shown that unintentionally doped GaN has high n-type background carrier concentration, often between $10^{16} – 10^{17}$ cm^{-3} [7] but there have been no report on high resistivity uncompensated GaN films. High *n*-type background conduction originates mostly from substitution residual impurities such as O and Si and in some case due to nitrogen vacancies [8,9]. Origin of oxygen may happen during the growth process: as an impurity in the NH_3 precursor in metal-organic chemical vapor deposition (MOCVD); as a residual moisture background in molecular beam epitaxy (MBE); from dissociation of the sapphire substrate; or from

leaching of the quartz tube in many plasma sources. The background concentration of electrons can also have a detrimental effect on *p*-type doping. The residual electrons need to be overcompensated to achieve *p*-type conduction. This problem can be overcome by proper purification of source materials and by improving vacuum conditions.

c. Ineffectiveness of p-type doping: It is easier to achieve *n*-type conductivity because the donors are much shallower than the acceptors. Although compensation by the residual electron concentration has become much less of an issue, successful and reproducible *p*-type doping has become an issue.

One set of candidates for *p*-type doping in III-V materials are the Group IV elements like C, Si, and Ge. For *p*-type doping, these elements substitute for an N atom resulting in an excess of conducting holes. C is an amphoteric impurity and has been used to produce high-resistivity GaN material [10]. The Group II elements are also obvious choices for *p*-type dopants, but elements such as Zn and Ca have a d-shell of electrons and form a resonance with the lower valence bands of the crystal and consequently a deeper level in the valence band [11]. Neither Mg or Be have a d-shell and they may be considered as a potential shallow acceptor impurities for *p*-type GaN [6].

It is reported that Mg is a *p*-type dopant with an acceptor activation energy of ~200 meV [12]. Room temperature hole concentration greater than 10^{18} cm^{-3} have been achieved. The results obtained on *p*-type GaN, show low hole mobility (1-10 cm^2/V-sec) and consequently limits the maximum achievable conductivity. The lack of high *p*-type conduction leads to high resistivity contacts that are the limiting factor in many electronic

devices. For example, the *p*-type layer accounts for nearly the entire voltage drop in GaN-based laser diodes leading to high turn-on voltages and severely limiting the device lifetime. Other problems include the necessity of post-growth processing to activate the Mg that is compensated during growth with hydrogen [1]. This can be performed either by low-energy electron beam irradiation (LEEBI) [13] or thermal annealing [14,15]. Similarly, Be also seems to be a promising *p*-type dopant. The acceptor level was theoretically predicted to be as low as 60-100 meV above the valence band [16,17].

1.3 Existing issues with Silicon carbide

During the past 10 years, SiC technology had advance remarkable progress, but one key question still remains unanswered: how to control the SiC crystal growth to reduce micropipes formation? It has been experimentally demonstrated that micropipes nucleate from the crystalline regions that incorporate defects such as inclusions, polytype disturbances, thermally induced stress, low-angle grain boundaries, partial dislocations, voids, etc and are mostly formed at the initial stage of growth. There are many theories or mechanisms that have been proposed to explain the formation of micropipes in SiC. But, there are questions on their total applicability to a wide variety of experimental observations of micropipe formation.

Luminescence imaging is one of the most versatile and useful techniques, which can be used in the analysis of micropipes and other types of defects such as polytype inclusions, grain boundaries, and dislocations. Hence, in this work luminescence imaging

was employed to characterize bulk SiC crystals. A detailed description of the equipment used for this purpose is given later.

1.4 Optical Characterization

Our understanding of the nature of the crystal defects has been increasing over the past 50 years or more owing to the development of refined experimental techniques. A variety of techniques are used to probe the optical and electrical signatures associated with the point defects. Luminescence is a powerful tool used in the detection and identification of point defects present in semiconductor materials. It finds application especially in case of wide-band-gap semiconductors, where electrical characterization is limited, because of the large activation energies of the defect centers that are beyond the reach of normal experimental thermal means. The following is a brief introduction of luminescence spectroscopy, with a special emphasis on the analysis of semiconductors.

Luminescence can be described as the process of emission of photons when certain form of energy is supplied to a solid. The wavelength of each photon is directly related to the energy of the transition by $E = h\nu = hc/\lambda$. Luminescence phenomena in direct and indirect bandgap semiconductors have some differences [Shown in Fig. 1]. In a direct bandgap material, the most likely transitions are across the minimum – energy gap, between the most probably filled states at the minimum of the conduction band and the states most likely to be unoccupied at the maximum of the valence band. Radiative recombination between electrons and holes is relatively likely in such transitions. But in an indirect bandgap material, phonon participation is required. Thus, the recombination of electron-hole pairs must

be accompanied by the simultaneous emission of a photon and a phonon. Therefore, fundamental emission in indirect bandgap semiconductors is relatively weak.

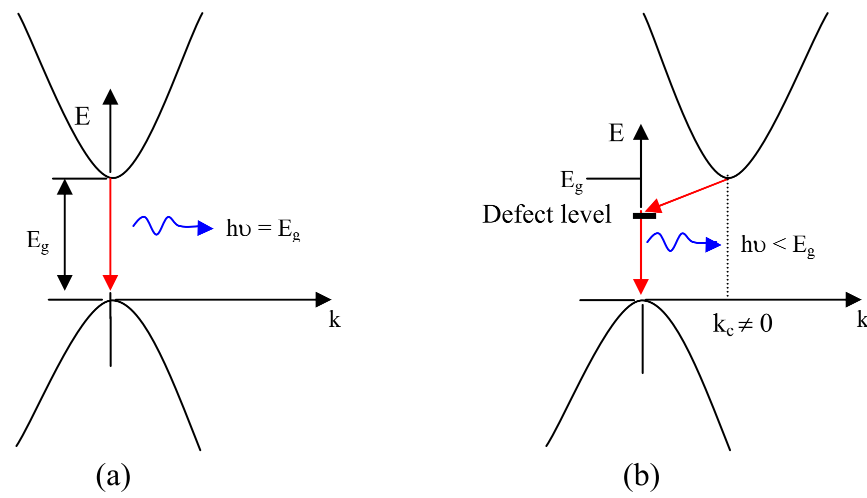

Figure 1: E-k diagrams for: (a) Direct bandgap semiconductor; (b) Indirect bandgap semiconductor.

Depending on the source of excitation, the luminescence can be categorized as, photoluminescence (photon excitation), cathodoluminescence (excitation by energetic electrons, or cathode rays), chemiluminescence (energy supplied by chemical reaction), electroluminescence (excitation by application of an electric field) and thermoluminescence (emission of light when the sample is heated). The most important experimental methods used for the investigation of defects in wide-band-gap materials are photoluminescence and cathodoluminescence. It is also possible to investigate the

nature of defects, defect concentrations and other relevant parameters by many other techniques such as X-ray diffraction (XRD), Photoconductance spectroscopy, nuclear magnetic resonance (NMR) etc, all of which can provide important information.

When an electron is excited from the valance band into the conduction band, the electron and hole become free and they can move independently in corresponding bands. A simplified set of radiative transitions that lead to emission in semiconductors when an electron is promoted are shown in Fig. 2. It gives a clear picture of the radiative processes that occur between the conduction and valance bands involving the impurity/defect states.

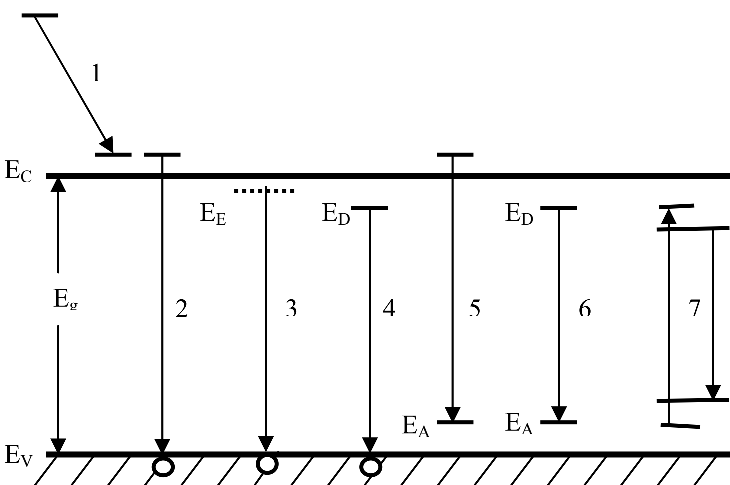

Figure 2: Schematic diagram of radiative transitions between the conduction band (E_C), the valence band (E_V) and exciton (E_E), donor (E_D) and acceptor (E_A) levels in a semiconductor [18].

General properties of these transitions are given below.

1- Intraband transition: An electron excited well above the conduction-band edge dribbles down and reaches thermal equilibrium with the lattice. This process may lead to phonon-assisted photon emission or just phonon emission.

2- Interband transition: It produces intrinsic luminescence. Here direct recombination occurs between the electron in the conduction band and a hole in the valence band resulting in the emission of a photon of energy E_g. Although this recombination occurs from states close to the corresponding band edges, the thermal distribution of carriers in these states will lead, in general, to a broad emission spectrum.

3- Exciton decay observable at low temperature: Both free excitons and excitons bound to an impurity may undergo such transitions. For bound excitons, one of the charge carriers is localized at a center that can assist in conserving momentum during the transition.

   Free exciton recombination is denoted by X, and recombination of an exciton bound to a neutral donor is denoted by D^0X, and to a neutral acceptor by A^0X, and excitons bound to the corresponding ionized impurities by D^+X and A^-X, respectively.

4,5,and 6- These transitions start and/or finish on localized states of impurities (donors and acceptors) in the gap; producing extrinsic luminescence. These three processes account for most of the luminescence processes in a wide variety of

semiconductors. These transitions are designated with the symbols given below.

4 → donor-to-free-hole transition - D^0h

5 → free-electron-to-acceptor transition – eA^0

6 → donor-acceptor pair (DAP)

7- Represents the excitation and radiative deexcitation of an impurity with incomplete inner shells, such as in a rare earth ion or a transition metal.

These luminescence bands provide information about the kinds of defects present in the unintentionally/intentionally-doped nitrides and other semiconductors. Photoluminescence (PL) has been the most widely used experimental method for the investigation of defects in bulk unintentionally doped GaN and intentionally/unintentionally doped nitride epitaxial layers.

1.4.1 Photoluminescence Spectroscopy

In photoluminescence, a photon is absorbed by the semiconductor, creating an electron-hole pair, which then recombines, emitting another photon. PL is conveniently used for characterizing materials in which contact or junction technology is not adequately developed or in high-resistivity materials where electroluminescence would be inefficient or impractical. It permits flexibility in the configuration of the excited region and in the choice of the location on the crystal. Also the PL is a sensitive and non-destructive technique, helpful in the detection and identification of impurities under controlled conditions. The binding energy obtained from the spectral positions or

thermal-ionization studies can be used to identify the localizing center. Unfortunately, due to a simultaneous presence of a number of defects in the material and their competitions at different rates for the photo-excited carriers, resulting in radiative and non-radiative recombination processes, PL has a limited value as a quantitative technique. A schematic of the low temperature PL setup used in this study is shown in Fig. 3. where the samples were in the chamber of a continuous Helium (He) flow cryostat. The 325 nm line of HeliumCadmium (HeCd) laser was used to photo-excite the carriers. The light emitted by the sample was dispersed by an 85 cm double-grating spectrometer fitted with 1800 groves/mm gratings. Data acquisition was performed using a UV-sensitive GaAs photomultiplier tube coupled to a computer-controlled photon counter.

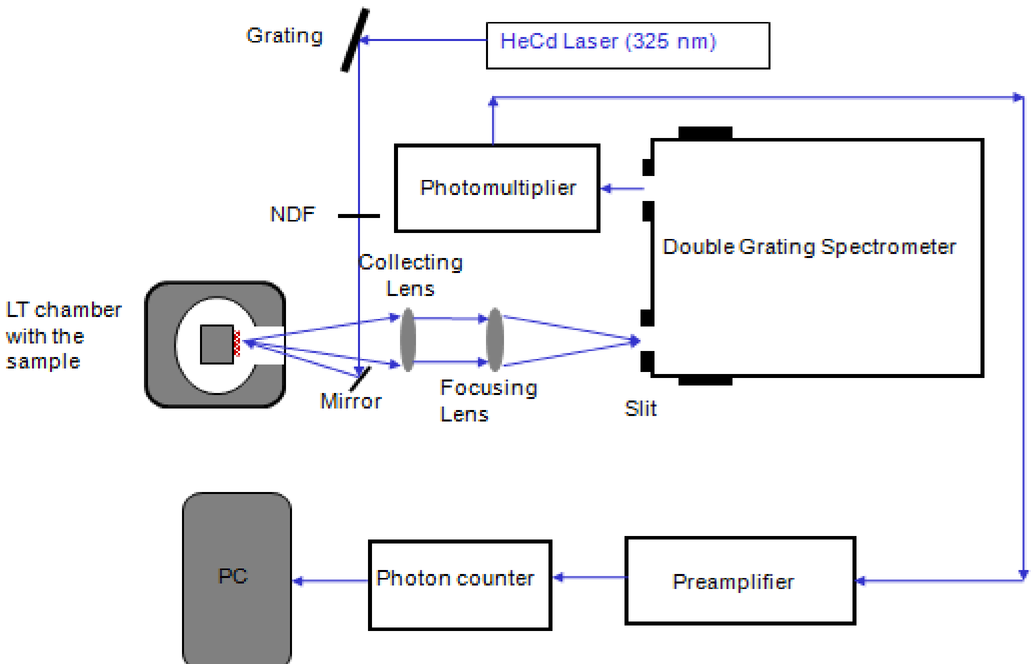

Figure 3: A schematic of the photoluminescence spectroscopic set-up.

1.4.2 Photoluminescence Imaging

Devices made of wide bandgap materials are facing various issues related to defects nucleated in the substrate or epitaxial layers. Device-killing defects like micropipes reduce the breakdown voltage. Similarly, low angle grain boundaries (consisting of a mixture of basal plane dislocations and threading edge dislocations) act as nucleation sites for stacking faults in bipolar devices. Various imaging techniques have been used to understand the nature of these defects, but each technique has its own limitations. For example:

- Transmission electron microscopy (TEM) is a destructive technique and provides small field of view.
- Information collected by molten potassium hydroxide (KOH) etching is extremely limited since etching occurs only at the sample surface.
- Synchrotron white beam X-ray topography (SWBXT) requires synchrotron X-ray source, which is not widely available.

In this work, visible and ultra-violet (UV) photoluminescence (PL) imaging was employed to record the defect structures present in GaN films and SiC epilayers. Its both a non-contact and a non-destructive technique to image dislocations and other extended defects in SiC epilayers.

The PL imaging system used in this work comprises of:

- 325 nm line of HeCd laser.
- Combination of UV-corrected lenses and mirrors are used to expand the laser beam to achieve the required uniform wafer illumination.

- A near UV-extended CCD with built-in wheel filters, fitted with a collecting lens, are employed to acquire the real color [combination of Red, Green and Blue (RGB)] and monochromatic color (Red, Green or Blue) images individually.
- External filters with specific band-passes can be conveniently used to map the spatial distribution of specific defects.

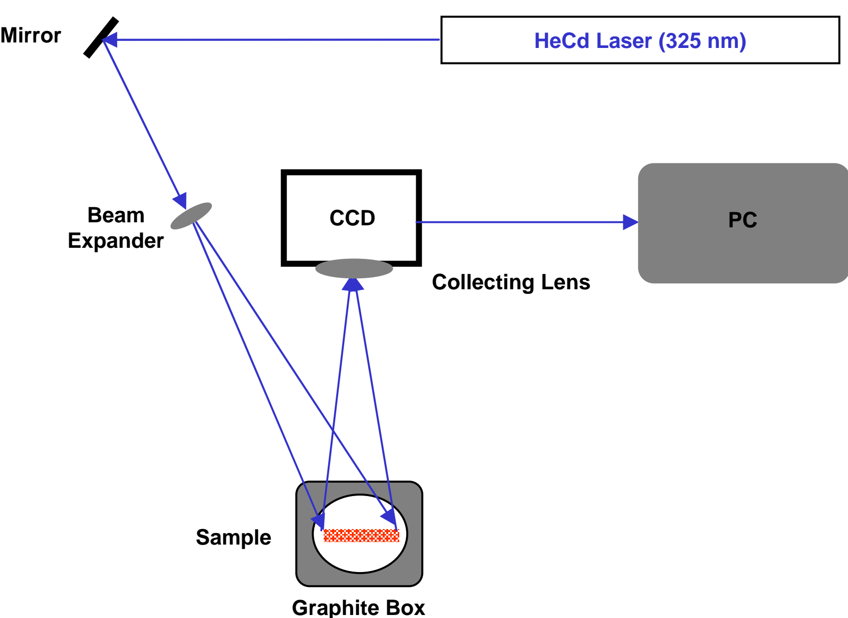

Figure 4: A schematic of the photoluminescence imaging set-up.

The laser power density is controlled by calibrated neutral density filters. PL imaging set-up shown in Fig. 4 can be used to acquire images at room temperature as well as at low temperatures. The low temperature imaging were captured with the sample been placed in liquid nitrogen dewar. This set-up was used for wafers with a size of 2 to 3

inch diameter. The luminescence image is collected using a CCD, connected to a computer.

An inverted microscope was employed to obtain high magnification images, as shown in Fig. 5. Magnification up to 100X can be achieved with this setup.

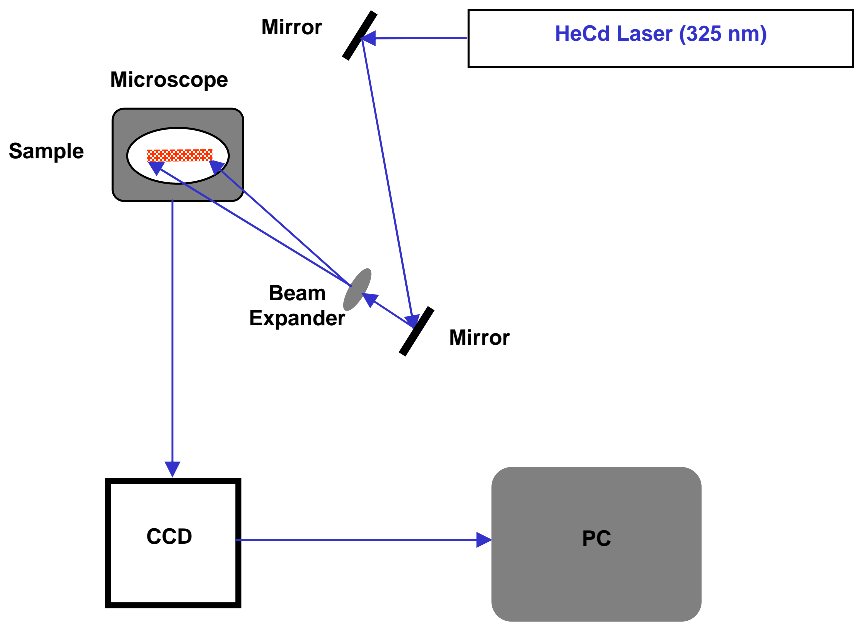

Figure 5: A schematic of photoluminescence imaging set-up using an inverted microscope.

1.5 Objective of this work

This thesis work is mainly focused on identifying of dopant and defect related centers in wide band-gap semiconductors, GaN and SiC, using non-destructive optical characterization techniques. Results of this work are useful for optimizing the growth and annealing conditions for improving GaN and SiC based device processing. The samples considered for this study were bulk crystals and epitaxial nitride films grown by different techniques such as MOCVD, MBE and growth from solution at moderate temperatures and pressures. Along with the optical characterization, structural and electrical characterizations were performed to understand the nature of defects.

In-situ Mg doped and Be doped GaN epilayer samples were subjected to high temperature microwave annealing in the temperature range of 1300 –1600 ^{0}C for an interval of 5-15 s in N_2 gas ambient. Characterization of these microwave annealed in-situ doped epilayers showed improved crystal quality of the epilayer and enhanced activation of the Mg acceptor. Similar studies were performed on Mg ion-implanted GaN samples for a better understanding of activation behavior of Mg acceptors in GaN epilayer.

This work was extended to understand luminescence of defects in SiC wafers. Comparative studies of defect microstructures in 4H-SiC wafers have been carried out using PL imaging technique and synchrotron white beam X-ray topography (SWBXT). The PL imaging is most capable of revealing defects like micropipes, low angle grain boundaries, and dislocations.

1.6 Thesis Organization

This thesis is divided into six chapters (including the Introduction chapter). Chapter 2, is about the characterization performed on bulk GaN grown by HVPE and GaN grown from solutions at moderate temperature and pressure.

Chapter 3 is divided into two parts. The first part is about the structural and optical characterization of freestanding GaN grown by HVPE method and the second part is about residual impurities present in GaN substrates and epitaxial layers grown by organic metallic vapor-phase epitaxy (OMVPE) and molecular beam epitaxy (MBE) methods.

Chapter 4 is divided into four parts. In the first part, results obtained from characterizing Mg-doped GaN grown by MBE method are presented. In the second part, structural and optical characterization results of microwave annealed in-situ Mg doped GaN films grown by MOCVD are presented. Similarly in the third part, secondary ion mass spectroscopy and optical characterization results of microwave annealed in-situ Be doped GaN are presented, and finally in the fourth part results of microwave annealing on Mg ion-implanted GaN are discussed.

In chapter 5, non-destructive characterization of dislocations and micropipes in 4H-SiC using PL imaging in comparison to other techniques such as synchrotron white beam X-ray topography, electron beam induced current and color cathodoluminescence are presented. Also PL imaging was performed on device structures and the results were correlated with device current-voltage characteristics. Finally chapter 6, summarizes the results.

2. CHARACTERIZATION OF BULK GALLIUM NITRIDE

In the past 10 years [19,20], significant progress has been made on III-nitrides based semiconductors, specially GaN, which provides potential for both electronic (e.g., HEMTs) [21] and optoelectronic (light-emitting diodes and laser diodes) [22] device applications. Presently, the development of devices with low leakage current, higher breakdown voltage, and high room-temperature carrier mobility is highly desired. It's possible to achieve such requirements by depositing GaN films on native GaN substrates than on foreign substrates such as sapphire and silicon carbide. To evaluate the quality of bulk GaN, structural, optical and electrical characterization is performed on bulk GaN grown by two different techniques. The two techniques are:

1. Hydride vapor-phase epitaxial (HVPE) growth method
2. Growth from solution at moderate temperature and pressure.

Results obtained from the characterization of bulk GaN samples can be used by the growers to optimize the growth process to produce higher quality GaN films.

2.1 Semi-insulating Fe-doped GaN substrate grown from HVPE method

To mitigate the relatively high intrinsic concentration of free carriers, a number of growers have used impurities such as Be, C, Fe, and Zn to compensate the pervasive

shallow donors in GaN, to achieve the desirable semi-insulting (SI) substrate characteristics [23-25]. Among these impurities, Fe seems to be the most suitable impurity because the $Fe^{3+/2+}$ acceptor level is only about 0.34 eV below the bottom of the conduction band [26]. It is expected that this deep acceptor level will efficiently compensate the GaN free carriers at typical device operating temperatures. In fact, it has been demonstrated that iron doped HVPE GaN substrates can have reproducible resistivity of about $3x10^5$ Ω·cm at 250 °C [27]. Also detailed studies investigating the dilution limits and doping efficiency of iron in GaN based on the GaN morphology and iron doping uniformity have been reported [28].

This study was performed to understand the optical and electronic properties of freestanding (FS) bulk HVPE GaN substrates, both undoped and iron doped, which were originally grown on sapphire substrates.

2.1.1 Experimental Details

The GaN samples used in this study were grown at Kyma Technologies, Inc., Raleigh, NC. The growth was performed using a vertical HVPE hot-wall reactor, at sub-atmospheric pressure. The GaCl precursor was produced by reaction between HCl and liquid Ga in the upstream part of the reactor, which is kept at 915 °C. Bis (cyclopentadienyl) iron (Cp_2Fe) was used as the iron source for the Fe-doped GaN crystals, which was introduced into the reactor via a N_2 carrier gas. The GaN films were deposited on c-plane (0001) sapphire substrates with an AlN nucleation layer, in the

downstream part of the reactor where the GaCl and the NH_3, transported by N_2 gas, react. The GaN growth was carried out at substrate temperatures of approximately 1000 °C. The growth rate of the films was 150 μm/h. Thick layers (1-2mm) were grown and removed from the underlying sapphire to create freestanding, bulk material. The layers were characterized in the as-grown state, i.e. without polishing or surface preparation. Polar and non-polar GaN layers grown using this process have been previously shown to possess very good structural properties [29,30]. The doping level of similarly grown Fe-doped crystals in the same system was measured via secondary ion mass spectrometry (SIMS) to be around $1x10^{18}$ cm^{-3}.

The crystalline properties of the undoped and iron doped samples were probed by X-ray diffraction (XRD) measurements using a Philips X'pert MRD triple axis diffracted beam system at Kyma Technologies, Inc. The morphologies of these samples were verified by SEM and SEM panchromatic cathodoluminescence imaging (SEM/CLi) techniques, and by real color (Red, Green and Blue – RGB) photoluminescence imaging (PLi) using a HeCd laser to excite the samples, at room temperature. Low temperature PL spectroscopy was employed to verify the optical and electronic properties of the samples. The PL system comprised of an 1800 grooves/mm double gratings spectrometer and an UV-extended GaAs photomultiplier coupled to a computer controlled photon-counter. The samples were placed in a continuous flow He cryostat, which allows temperature variations between 1.5 K and 330K. The luminescence was excited with the 325 nm line of a HeCd laser, whose power density was controlled with calibrated neutral density filters.

The incorporation of the iron impurity and the activation of $Fe^{3+/2+}$ compensating acceptors were corroborated by low temperature near infrared (NIR) PL spectroscopy. The samples were placed in a cold-finger cryostat and excited with the 808 nm line of a diode laser. The light emitted by the samples was dispersed by a Princeton/Acton Trivista 557 triple spectrometer fitted with liquid nitrogen cooled OMA V InGaAs linear array detector.

2.1.2 Experimental Results and Discussion

2.1.2.1 X-Ray Characterization

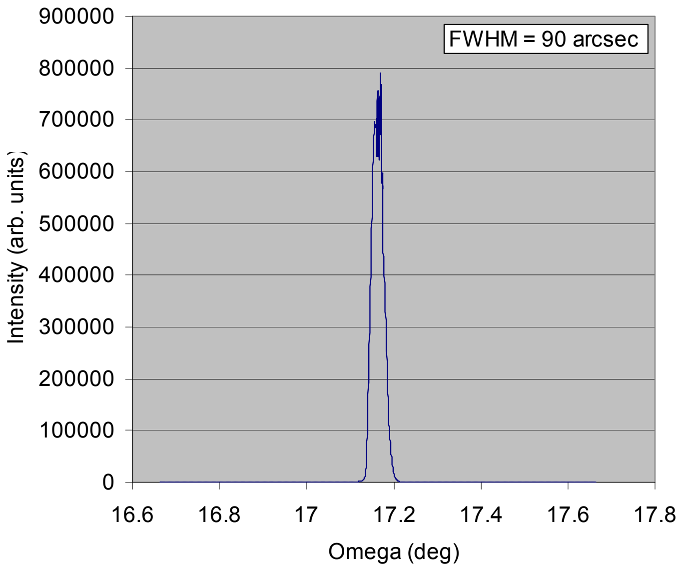

Figure 6: XRD spectrum of one of the Fe-doped thick freestanding GaN substrate.

The full width at half maximum (FWHM) of the (0002) XRD peak recorded on the Fe-doped GaN (sample # AE492.7) is only 90 arcsec as shown in Fig. 6 and the FWHM of the $(10\underline{1}2)$ XRD peak is 146 arcsec, which is consistent with a high crystalline quality material and is a representative of the X-ray linewidth of other measured samples.

2.1.2.2 Photoluminescence Imaging

Real-color PL imaging of the unintentionally doped (UID) GaN substrate AE498.11, represented in Fig. 7(a), has an intense red color hue emission. Fundamental colors imaging show that red is the dominant emission, with an intense green and weak blue contribution. The color and intensity distribution is quite uniform, and only two hexagonal base pyramid defects are observed at the sample surface. The PL panchromatic imaging of this sample, represented in Fig. 7(b), also shows a quite uniform distribution of intensity, with few dark spots. The panchromatic SEM/CLi of the white boundary rectangular region indicated in the sample imaging, insert (1), confirms the good sample uniformity. SEM imaging of the same highlighted region depicted on insert of Fig. 7(b), due to high current contrast, shows clearly the presence of pits, which are weakly observed in the SEM/CLi picture. Similar experiments were performed on the iron-doped samples. Fig. 8(a) shows the RGB PL imaging of the iron doped sample AE492.7. This imaging shows a green-yellow color hue, which results from the mixture of a relatively weak green contribution with less intense red and an extremely weak blue emissions component. It is clearly seen in Fig. 8(a) a non-uniform distribution of luminescence

intensity across the sample. Bright regions with "palm tree leaves" shape appear across the samples. Such features, not yet identified, are not related to the iron doping, because they have been observed in UID substrates. Panchromatic imaging of this sample, depicted in Fig. 8(b), reveals the same features observed in the RGB PL image. The SEM and SEM/CL images of this sample (not shown) clearly demonstrated that the morphology of this sample is similar to that of the UID sample.

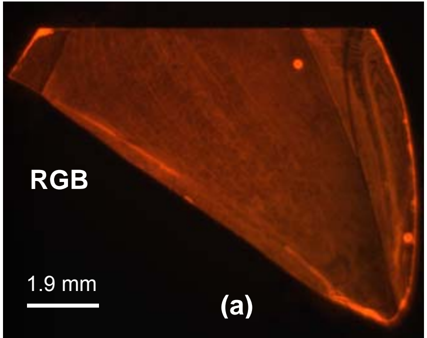

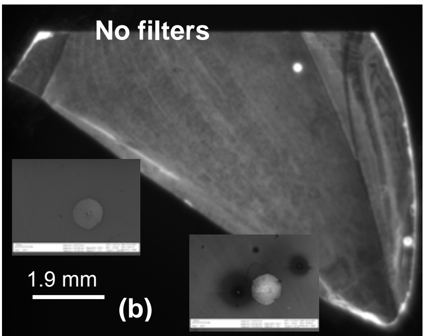

Figure 7: (a) RGB PL imaging of UID GaN film grown on AlN/Sapphire template. (b) Panchromatic PL imaging of the sample shown in (a). The inserts (1) and (2) show the SEM/ CL and SEM/imaging of the region highlighted in 2(a), respectively.

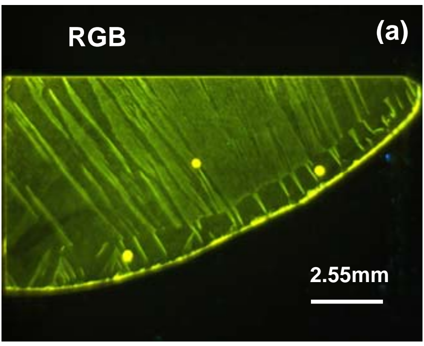

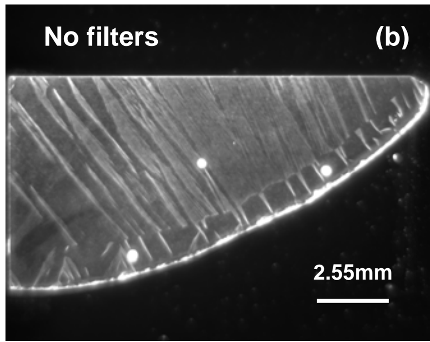

Figure 8: (a) RGB PL imaging of a Fe-doped GaN substrate. (b) Panchromatic PL imaging of the sample represented in (a). Note the bright "palm tree leaves" shape defects.

2.1.2.3 Photoluminescence Spectroscopy

To probe changes in the electronic properties of HVPE GaN substrates with iron doping, we performed a detailed low temperature PL measurements on one UID (AE498.11) and two iron doped (AE486.3 and AE492.7) samples, which are represented in Fig. 9, in the spectral range between 1.97eV and 3.57 eV. Iron doping concentration of sample # AE 486.3 and sample # AE492.7 is around 1×10^{18} cm^{-3}. The spectra of the UID substrate (AE498.11), spectra #1 in Fig. 9, shows the typically intense and dominant recombination emission lines associated with annihilation of excitons bound to neutral donors (D^0X, leaving the donor in the ground state after the annihilation) near 3.47 eV, and their phonon replicas (nLO-D^0X) [31]. Also observed are the less intense zero-phonon lines of shallow-donor/shallow-acceptor pair (DAP) recombination near 3.29 eV and their phonon replicas (nLO-DAP), a weak broad luminescence band around 3.0 eV,

and the so called yellow band at 2.25 eV. We also observe a relatively intense red band, which peaks around 1.75 eV. Note that all bands observed in the spectrum of the UID sample are reproduced in the spectra of the iron-doped samples. However, it is important to point out that the relative intensity of all these bands decreases in the doped samples. This observation is consistent with the change in the room temperature PL imaging intensity.

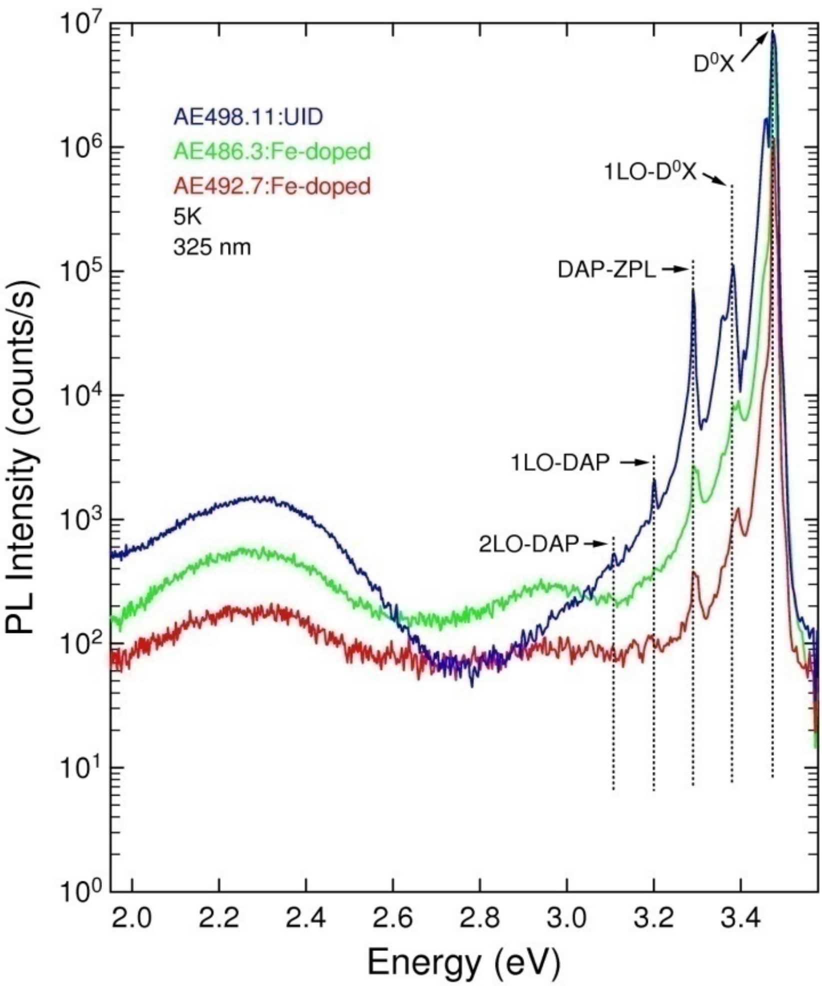

Figure 9: Low-resolution and low temperature PL spectra of undoped and iron doped samples. Note the reduction of all luminescence bands in the iron doped samples.

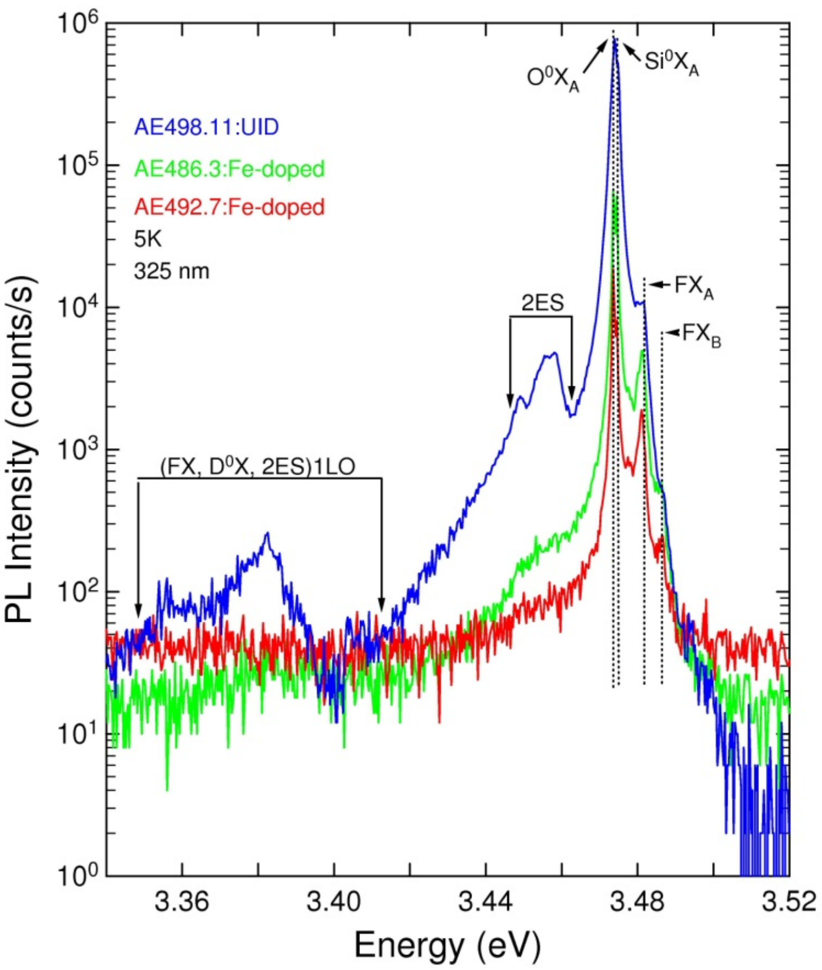

Figure 10: High-resolution and low temperature PL spectra of the samples represented in Figure 9, in the near band-edge spectral region.

Fig. 10 depicts the PL spectra of all samples represented in Fig. 9, in the near and-edge spectral region between 3.34 eV to 3.52 eV. The spectrum of UID sample show emission lines related to the ground state of the free-exciton B (FX_B), the ground state of

the free-exciton A (FX_A), and the dominant exciton bound to neutral Si and O donors ($S_i^0X_A$ and O^0X_A). Around 3.45 eV, the so-called two-electron satellite (2ES) spectrum resulting from the recombination processes that leave neutral donors in an excited state after the exciton annihilation is detected. Spectral separations between D^0X and 2ES lines yield the intra-center transition energies of the impurities. Note that for energies below 3.42 eV, we observe the one-phonon replicas of all features listed above, represented as (FX, D^0X_A, 2ES) 1LO. All the features observed in the spectrum of the UID samples are replicated in the spectrum of the iron doped samples. Again, note that their relative intensities reduce with increasing iron doping. In addition, the relative intensities of the FX_A and FX_B lines to the intensity of the D^0X line also increases in the doped samples. This is consistent with the compensation of the neutral shallow Si and O donors by the deep acceptor iron, which moves the Fermi level from the bottom of the conduction band towards the center of forbidden band-gap.

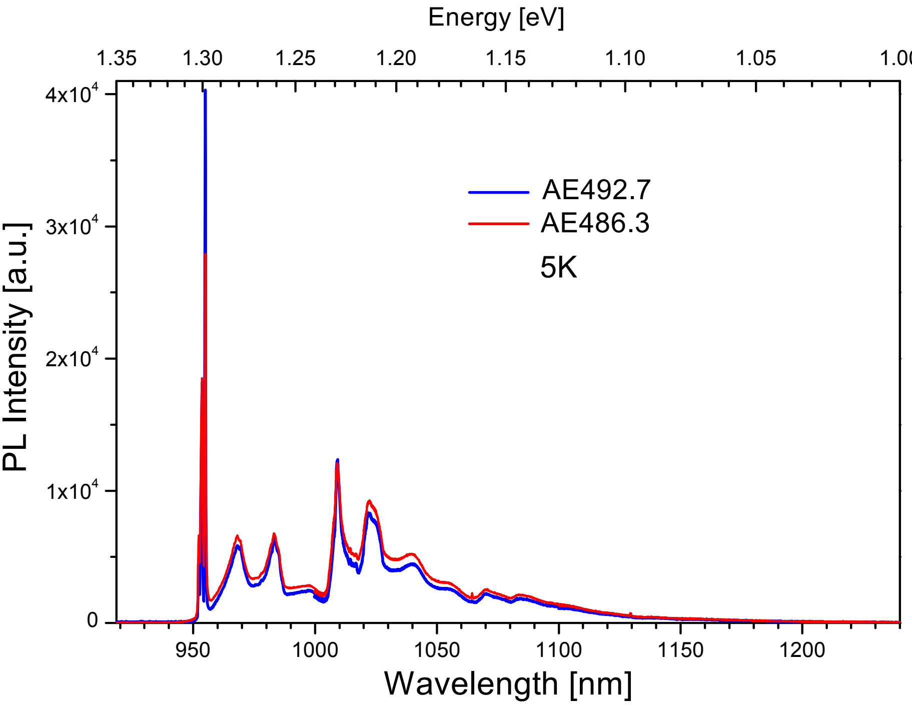

Figure 11: Low temperature NIR-PL spectra of the two Fe-doped samples. The intense emission line at 1.299 eV (~950 nm) is related to substitutional Fe impurities.

Low temperature NIR-PL measurements were carried out in all samples to verify the incorporation and activation of deep iron acceptors. Fig. 11 depicts the NIR-PL spectra of the two iron doped samples, AE486.3 and AE492.7. The intense line at 1.299 eV, represented in Fig. 11, is associated with the $^4T_1(G) \rightarrow ^6A_1(S)$ crystal-field transition of the iron substitutional for the Ga atom, i.e., Fe^{3+}_{Ga} [26,32]. The relatively broad additional lines observed in both sample's spectra are the phonon sideband structures. We observed a small spectral intensity variation between the two Fe-doped samples, which may be associated with different concentration of Fe^{3+}_{Ga}.

PL measurements performed on different regions of these samples showed no sizable variations of the peak intensity and energy position, indicating no local stress and concentration variation, i.e., PL intensity of the samples is spatially very homogeneous.

2.1.2.4 Electrical Characterization

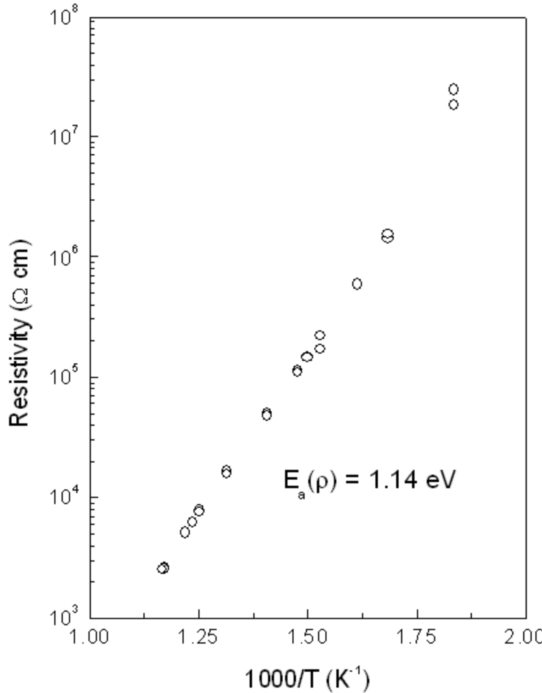

Figure 12: Fe-doped GaN resistivity as a function of 1000/T as determined by Hall Effect measurements.

The resistivity of the Fe-doped GaN samples was measured by Hall effect at different temperatures [This measurement was performed by co-workers at Kyma Technologies, Inc., Raleigh, NC]. Ti (250Å)/Al (1250Å) contacts with an Au capping

layer were used on the samples. The contacts were annealed at 600ºC prior to the measurement. Fig. 12 shows the resistivity calculated from the Hall effect measurements as a function of 1000/T for a Fe-doped GaN sample. The room temperature resistivity was greater than 10^{10} Ω·cm [33]. The activation energy of the deep level in the GaN was determined to be 1.14eV. This result indicates that high quality SI GaN substrates for high frequency device fabrication can be produced by Fe doping.

2.1.2.5 Summary

High crystalline quality, unintentionally doped and iron doped freestanding GaN films grown by HVPE process on sapphire with AlN nucleation layer can be reproducibly grown. No deterioration of the surface morphology and the structural and optical properties of the substrates were observed on Fe-doped substrates. Low temperature photoluminescence studies of these samples are consistent with full compensation of the pervasive Si and O shallow donors by Fe deep acceptors. In addition, the low temperature NIR photoluminescence shows that the incorporation of Ga substitutional Fe^{3+} compensating centers was realized. Temperature dependent Hall measurements clearly indicated the achievement of SI GaN substrate.

2.2 Bulk GaN crystals grown from solution at moderate pressure and temperature

Different techniques have been used to grow bulk GaN, but each technique has its own advantages and limitations. For example, it is possible to grow freestanding 2-inch diameter GaN film on a sacrificial sapphire substrate by HVPE [34]. Thick HVPE GaN films grown on *c*-plane sapphire have typical dislocation densities around 10^7 cm^{-2} [35]. However, the yield of GaN layer removal from the sapphire substrate is still low due to the lack of selective etchant. In addition, the formation of cracks and bowing in the GaN layer during the laser lift-off process makes this approach expensive. GaAs is another substrate option since it can be removed chemically or mechanically from the GaN layer. High quality HVPE GaN layer grown on GaAs showed a dislocation density of 10^5 cm^{-2} in a selected area [36]. Disadvantages of this approach are the presence of built-in residual strain and biaxial strain (specially formed during the cooling down process) resulting from different thermal expansion coefficients between the film and the substrate, and also formation of multiple crystal grains in the GaN film [37-39]. An alternative approach to grow single crystal GaN is by High Pressure-High Temperature (HPHT) liquid phase technique, which produces crystals with dislocation densities of approximately 10^2 cm^{-2} [40]. However, this technique produces only GaN crystal platelets of up to 1.5 cm lateral size and 300 μm of thickness. The typical low growth rate of this technique results from the low solubility of N in the liquid Ga, despite the high pressure of 10 kbar. In addition, GaN crystals can be grown at lower temperature/pressures by Na flux and Li flux methods [41,42]. Both flux methods use gaseous nitrogen, elemental

gallium and either alkali metal or alkali metal nitrides, which are employed to increase the reactivity and solubility of nitrogen in gallium. During the growth process gaseous nitrogen reacts with the elemental gallium to saturate the solution and deposit crystals. However, both methods have difficulties to establish and control seeded growth of large GaN crystals. To address these difficulties an alternate technique known as the thermal gradient molten solution is proposed. In this technique, a temperature gradient is used to control dissolution of solid GaN into the solvent and to deposit GaN crystals on seeds. This technique is appropriate for the industrial production of low dislocation density and low cost GaN substrates, which are requirements for large-scale production. The advantage of this method is the growth of GaN crystals on seeds from a supersaturated solution at moderate temperature and pressure as shown in the Fig. 13.

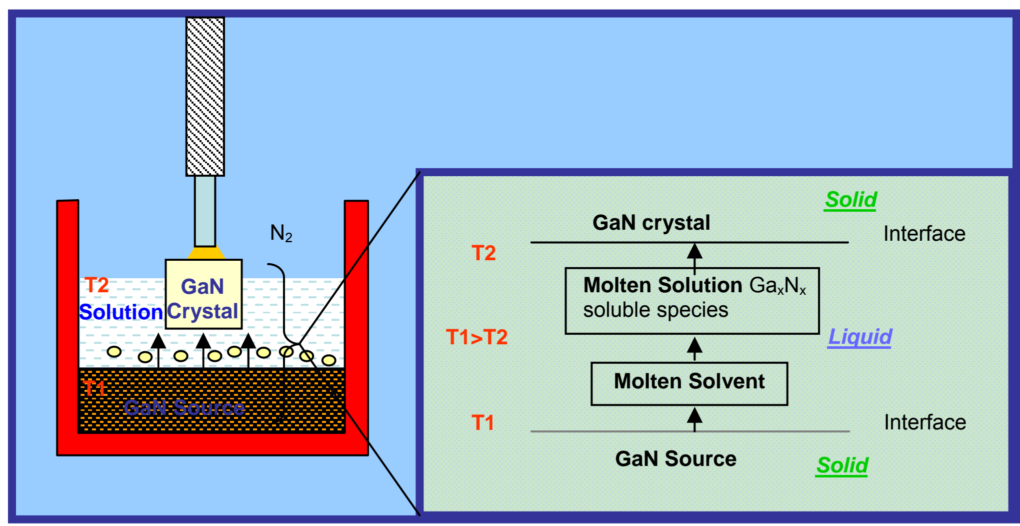

Figure 13: A schematics of the technical approach to GaN growth from solution.

2.2.1 Growth technique and sample information

Growth of GaN crystals was carried out at Naval Research laboratory, Washington DC, in a home built reactor coupled with a vertical tube furnace [43,44]. The reactor is designed in such a way that it is possible to perform top-seeded growth as shown in Fig. 14. The pressure in the furnace was maintained by using dry nitrogen gas (N_2). A multi-component based solvent efficiently dissolves the GaN source to create an appropriate growth solution in which GaN is stable at growth pressure and temperature. Solvent components are sensitive to moisture and oxygen. To minimize contamination by moisture and oxygen, the crucible and solvent components were handled in a glove box under dry nitrogen atmosphere with O_2 and H_2O content below 1ppm. After crucible charging, both were transferred from the glove box to the growth reactor. The crucible position in the reactor with respect to the heater was chosen to induce an axial thermal gradient inside of the solution. The seeds (if seeded growth was performed) were immersed in the solution, and the growth was performed at ~ 800 ^{0}C at a pressure of 0.25 MPa for 50 – 80 hrs.

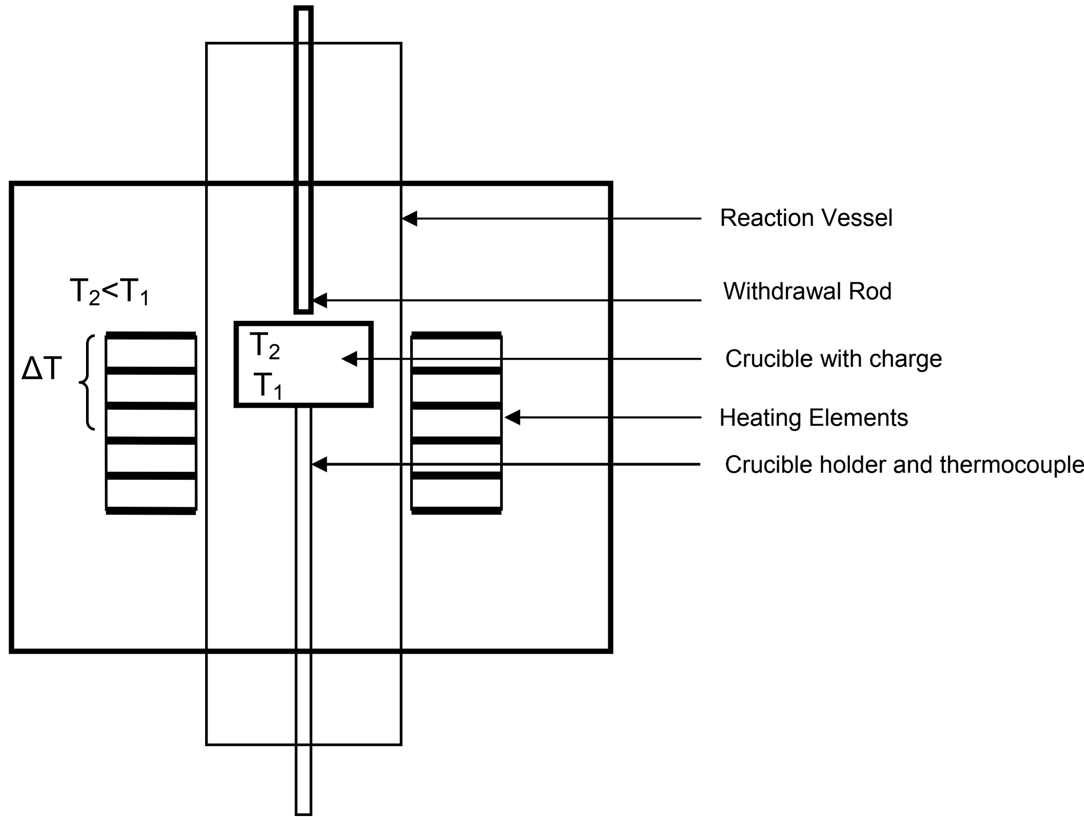

Figure 14: A schematic of the solution based growth reactor.

Three different categories of samples grown from solution at moderate temperature and pressure (SMTP) used in this work are: Sample I - spontaneously-nucleated GaN crystal; Sample II - GaN single crystals grown on HVPE GaN polycrystalline aggregates; and Sample III - homoepitaxial GaN layer grown on HVPE GaN template. Studies of self-nucleated GaN crystals and GaN single crystals grown on HVPE GaN polycrystalline aggregates should provide information on the growth of crystals with different crystalline directions. Similarly, studies of a homoepitaxial GaN

layer, grown on HVPE GaN template, should provide information about the viability of epitaxially grown GaN layers.

Optical microscopy, X-ray Difraction (XRD), micro-Raman scattering (μRS) and photoluminescence (PL) spectroscopy were used to characterize the GaN crystals.

2.2.2 Experimental Results and Discussions

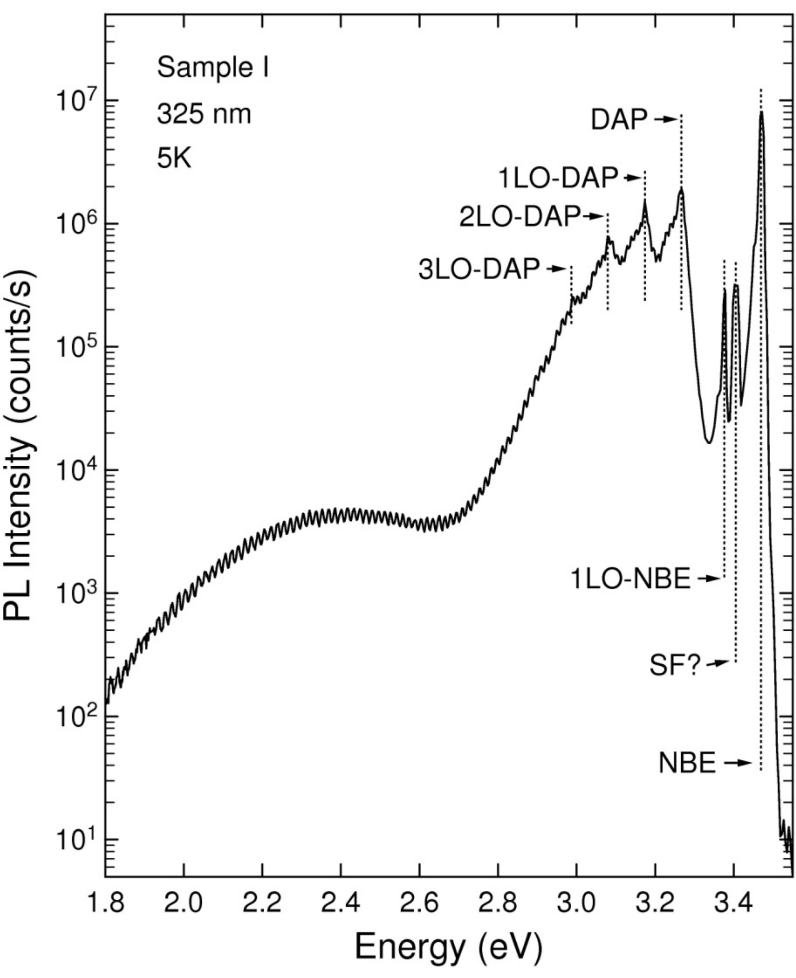

Figure 15: LT PL spectra of spontaneously-nucleated GaN crystal (sample I).

The critical part of this growth approach was the choice of solvent. The solvent should efficiently dissolve the GaN source and create a solution at moderate temperatures and pressures at which GaN is stable. As a result, GaN has been grown on a GaN seed utilizing the proper solvent at a growth temperature of 800°C and pressures of 0.2-0.3 MPa. The low temperature PL spectrum for a spontaneously-nucleated GaN crystal (Sample I) is shown in Fig. 15. This spectrum in the range of 1.8 - 3.55 eV, shows a dominant peak associated with annihilation of free and bound excitons at 3.47 eV, commonly known as Near Bandedge Emission (NBE) [31] with its phonon replica (1LO-NBE) at 3.37 eV. The intense broad band centered near 3.15 eV has been assigned to recombination processes involving electrons in the shallow neutral donors with holes in the shallow neutral acceptors [45]. This band, called shallow donor/shallow acceptor pair (DAP) band, has a zero phonon line (ZPL) at 3.26 eV, and phonon replicas at 3.17 eV (1LO-DAP), 3.08 eV (2LO-DAP), and 2.99 eV (3LO-DAP). Also observed is the well-known yellow luminescence (YL) band at ~2.25 eV.

To verify the nature of NBE and the unknown band at ~3.41 eV (indicated by 'SF?'), high resolution PL measurement was carried out and the result is represented in Fig. 16. The spectrum shows emission lines associated with the annihilation of free excitons involving holes from the valance band A (FX_A) at 3.481 eV and with the annihilation of free excitons involving holes from the valance band B (FX_B) at 3.485 eV. It is clear from Fig. 16 that the intense NBE line splits into two dominant peaks. The peak at 3.473 eV is assigned to annihilation of *A* excitons bound to shallow donors, leaving the

donors in the ground states (D^0X_A) and the peak at 3.463 eV is assigned to annihilation of *A* excitons bound to unknown shallow acceptor (A^0X_A) with A^0X_A phonon replicas (1LO- A^0X_A) at 3.376 eV [31,45,46]. Note that the D^0X_A peak also splits into two peaks, which is consistent with the incorporation of two shallow donors – oxygen (O^0X_A) and silicon (Si^0X_A) [31]. The peak at ~3.45 eV has been previously assigned to two-electron satellite (2ES) recombination process, which results from radiative recombination of the exciton bound to a donor, leaving the donor in an excited state, after their annihilation [31]. The emission band observed around ~ 3.4 eV (SF?) consists of two peaks at 3.4016 eV (FWHM of 5.2 meV) and 3.4095 eV (FWHM of 6.2 meV). These peaks are close to an emission band assigned to the emission associated with the annihilation of excitons bound to basal plane stacking faults (SF) in *a*-plane GaN layers as reported by Liu *et. al*. [47] and Paskov *et. al.* [48].

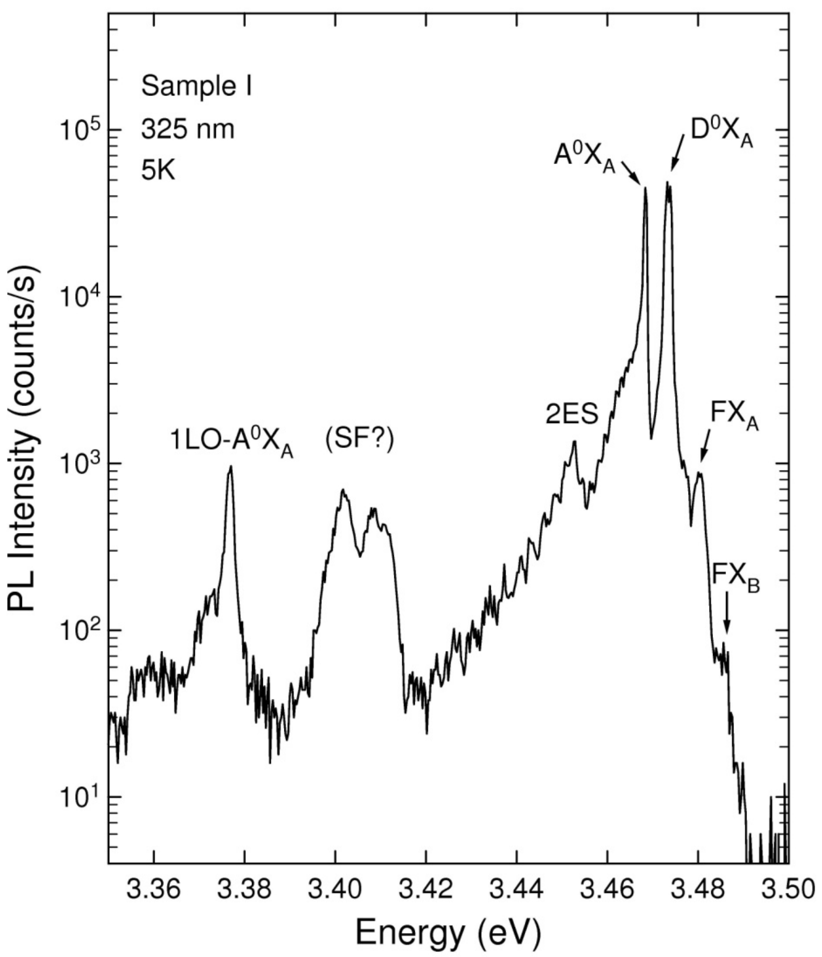

Figure 16: High-resolution PL spectra of spontaneously-nucleated GaN crystal (sample I).

To investigate the incorporation of point and extended defects on different crystalline growth sectors of GaN grown by SMTP, top seeded growth runs were conducted using HVPE GaN polycrystalline aggregates seed (Sample II) as shown in Fig. 17 [Grown by B.N. Feigelson at Naval Research Laboratory, Washington DC]. The shape of the polycrystalline pieces facilitates easy mounting and makes it simple to

observe dipping into the solution. This type of seed also gives an opportunity to study the nucleation and GaN growth on different crystal faces and in different crystallographic directions during one growth run. Fig. 17(b) shows such a polycrystalline seed before the growth run. The seed is mounted with Ta wire and dipped partly into the solution as shown schematically in Fig. 17(a). Due to the crucible position inside of the furnace (Fig. 14), the temperature of the seed was slightly lower than the GaN source. After 68 hours of exposure to the solution at 800°C and 0.24 MPa, the seed was removed. After cleaning the remaining solution from the seed, grown crystals of different orientations were found on the immersed portion of the seed. Most of the crystals formed as an epitaxial expansion of the crystallites of the aggregate (Fig. 17(c)). Some crystals were nucleated as twins on the very edge of the crystallites and developed as freestanding crystals (Fig. 17(d)). Most of the crystals grew epitaxially with the highest growth rates in the m-direction (Fig. 17(e)). All of the grown crystals were transparent and colorless, with well-defined hexagonal morphology.

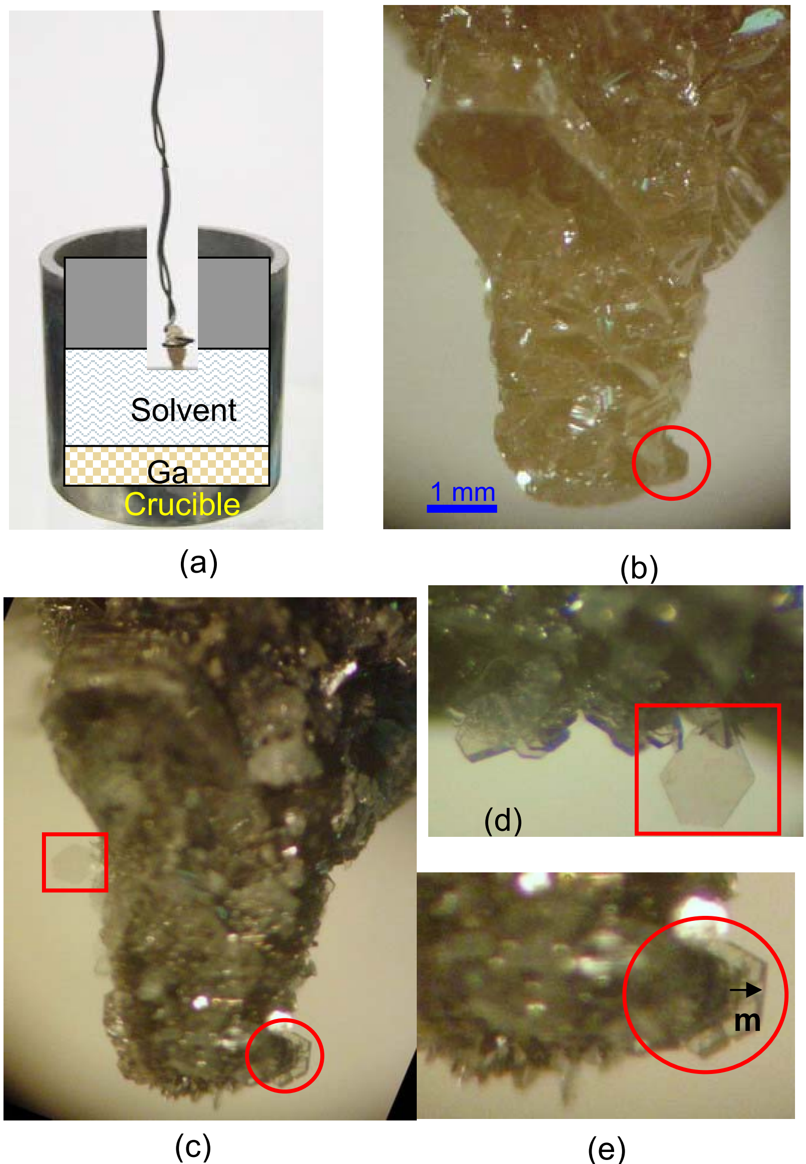

Figure 17: Schematic view and optical images of (a) the crucible with GaN source, solvent and HVPE GaN polycrystalline aggregate as seed, (b) the seed - HVPE GaN polycrystalline aggregate before growth run, (c) the seed - HVPE GaN polycrystalline aggregate after growth run with grown GaN crystals, (d) and (e) zoomed images of the crystals shown on the Figure 17(c), arrow indicates “m” direction.

High crystallinity of the grown crystals was also confirmed by XRD. This measurement was done by M. Mastro of Naval Research Laboratory, Washington DC. For XRD rocking curve measurements of the freestanding crystals a Blake double-crystal diffractometer equipped with a Si (100) beam conditioner and configured for the 004 diffraction with CuKα_1 radiation was used. Compared to typical diffractometers equipped with 4-bounce monochromators, the double-crystal instrument provides nearly one order of magnitude higher beam intensity at the sample and a much better resolution (5 arc-sec versus 12 arc-sec).

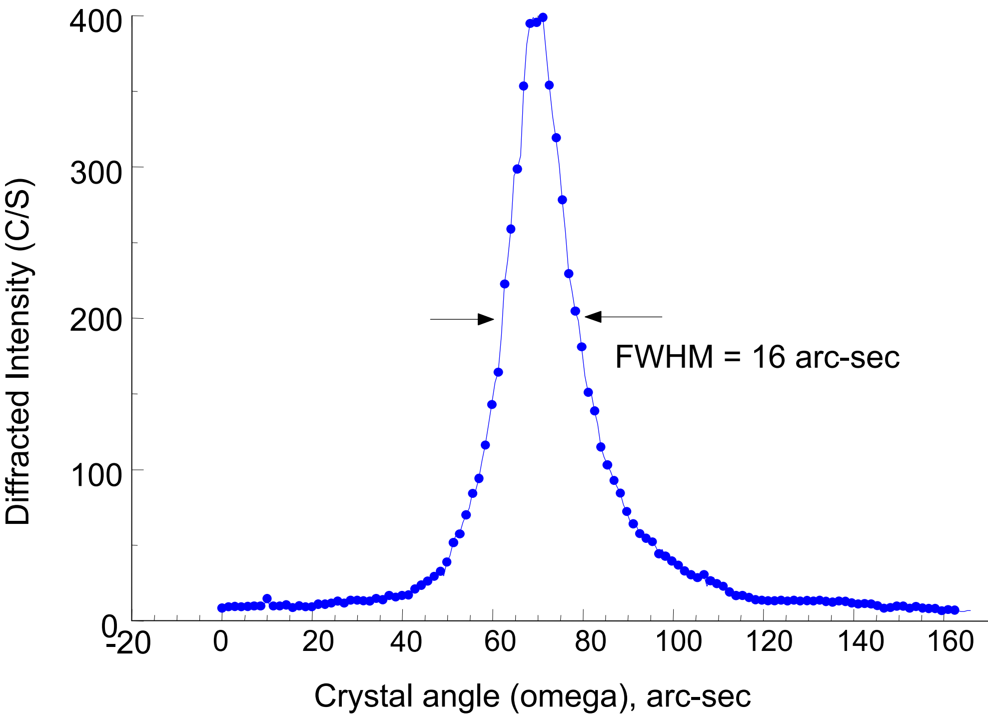

Figure 18: XRD rocking curve of the (0004) reflection for the GaN crystal grown on the polycrystalline GaN seed.

The beam size at sample was 80 μm wide and 200 μm high in cross-section. Note that the diffraction intensities represented on the rocking curve are actual count rates. The sample tilt was then adjusted for optimum rocking curve breadth and peak intensity. FWHM of about 16 arc-sec was obtained for the (0004) rocking curve, excluding the additional dispersion and convolution corrections that would only enhance this number slightly (Fig. 18).

Micro-Raman measurements were performed by J.G. Tischler at Naval Research Laboratory, Washington DC. This measurement was performed at room temperature in the backscattering geometry, in order to characterize the structural quality of the sample. The 1064.1 nm line of a Nd:YAG laser was focused to a 2μm diameter spot and used for excitation, while the scattered light was analyzed by a triple spectrometer TRIVISTA 557 equipped with an OMA V 1024-1.7 liquid nitrogen cooled InGaAs linear array detector. The FWHM spectral resolution of the system was 0.1cm^{-1}. Examination of the grown crystals with μRS spectroscopy in the $z(xy,xy)\bar{z}$ geometry showed the first-order allowed E_2^1, E_2^2 and A1(LO) phonons with full width at half-maximum (FWHM) of 0.26, 3.1 cm^{-1} and 6.9 cm^{-1}, respectively (Fig. 19). The sharp linewidths indicate high structural quality and low impurity concentrations [49,50].

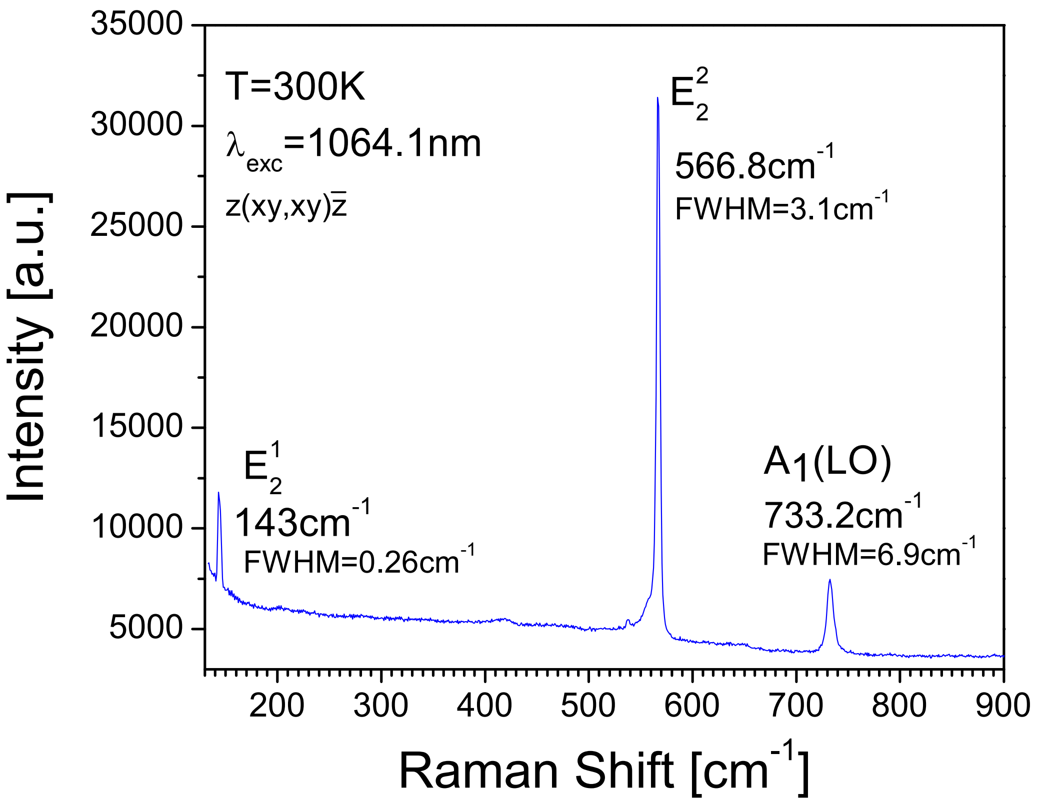

Figure 19: Room temperature micro-Raman spectrum of the GaN crystal grown on the polycrystalline GaN seed in the backscatter geometry.

To investigate the incorporation of point and extended defects on different crystalline growth sectors of GaN grown by SMTP, PL measurements were carried out on crystals grown on a HVPE GaN polycrystalline aggregate seed (Sample II). PL spectra of one of the individual crystals and its substrate, covering the spectral region 1.8 – 3.55 eV, are shown in Fig. 20. The spectra showed an intense NBE line at 3.47 eV with its phonon replica at 3.37 eV. Also observed is the intense broad emission band at

~3.41 eV (SF?), which has been previously assigned to excitons bound to basal plane SF in *a*-plane GaN layers [47,48]. The relative shift observed in the position of this unknown peak may result from strain introduced by the seeded growth process, as compared to the spontaneously-nucleated crystal (Sample I).

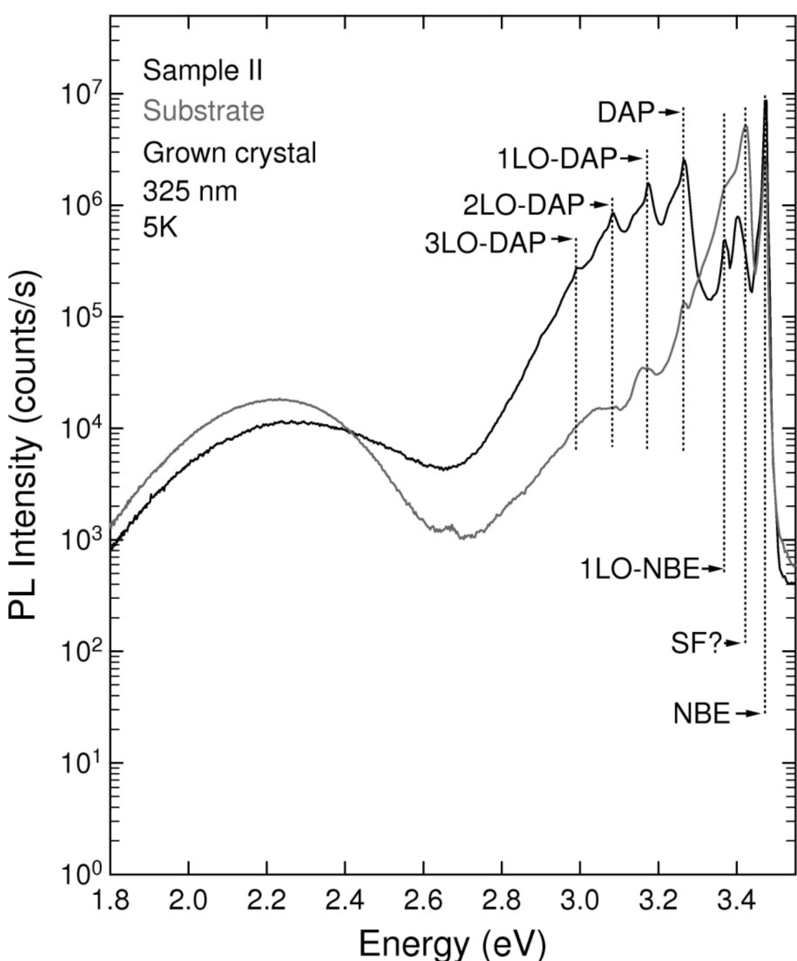

Figure 20: LT PL spectra of a HVPE GaN polycrystalline aggregate crystal seed (substrate) and the seed grown crystal (sample II).

A more intense and broad DAP band is observed in the spectrum of the grown crystal than that of the substrate, which may be attributed to larger incorporation of shallow acceptors in the grown crystal. Also observed is the reduction in the intensity of YL as compared with that of the substrate. This is consistent with the lower incorporation of native defects and/or residual donor impurities in the grown crystal as compared with the seed [51]. PL measurements performed on other individual crystals also showed similar features.

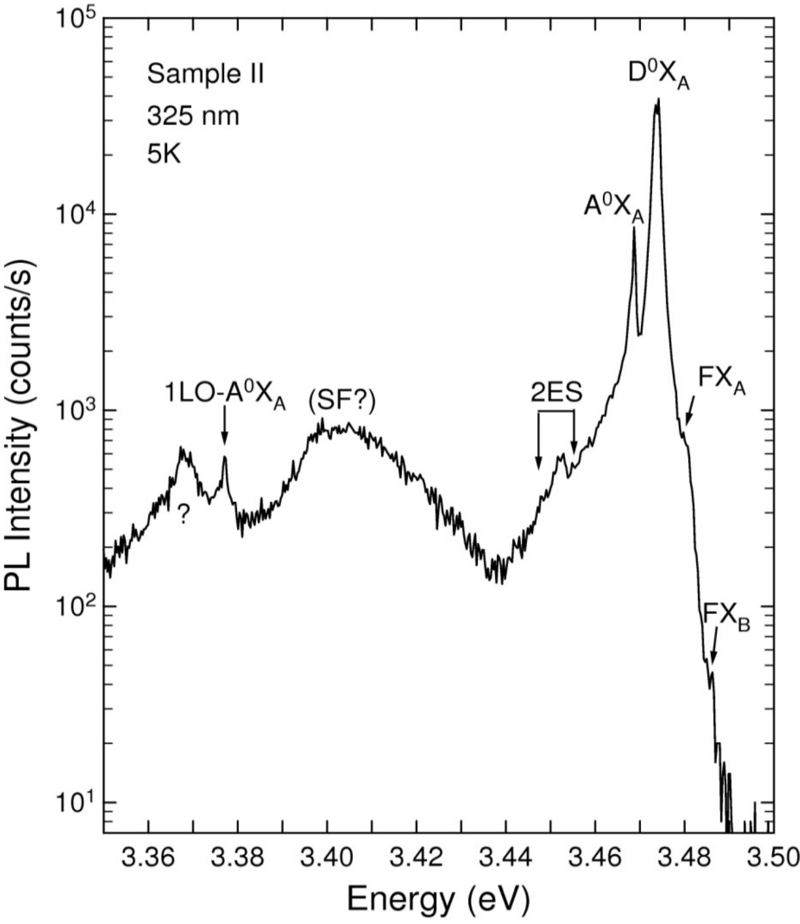

Figure 21: High-resolution PL spectra of grown crystal on HVPE GaN polycrystalline aggregate crystal seed (sample II).

Fig. 21 depicts the high resolution PL spectrum of the grown crystal showing a dominant peak at ~3.47 eV corresponding to *A* excitons bound to a shallow donor (D^0X_A). Improved crystalline quality was verified by reduced D^0X_A linewidth of the grown crystal, as compared with that of the seed. Spectra acquired with improved resolution (not shown) showed that D^0X_A is comprised of two lines, which is consistent with the incorporation of two dominant shallow donors i.e., oxygen (O^0X_A) and silicon (Si^0X_A) [31]. Around 3.45 eV, the so-called two electron satellite (2ES) is observed. Information about 2ES had been provided in section 2.2.2. This spectrum also includes emission lines related to A^0X_A (3.468 eV) [46] with 1LO-A^0X_A (3.376 eV), along with FX_A (3.479 eV) and FX_B (3.486 eV).

Growth runs were performed using HVPE GaN freestanding substrate as a seed to verify the prospect of homoepitaxial growth on single crystal GaN seeds (Sample III). The seed was mounted with Ta wire and partly immersed into the solution when the temperature in the solution reached 800°C. A small positive temperature difference between the seed and GaN source was induced by the chosen location of the crucible inside of the furnace as shown in Fig. 14. An epitaxially grown GaN layer was observed on the part of the template immersed into the solution for 80 hours (Fig. 22). Photographic images of the HVPE GaN templates were taken by B.N. Feigelson at Naval Research Laboratory, Washington DC. The part of the seed with the epitaxially grown layer showed enhanced transparency due to N-face surface improvement as seen in Fig. 22(a).

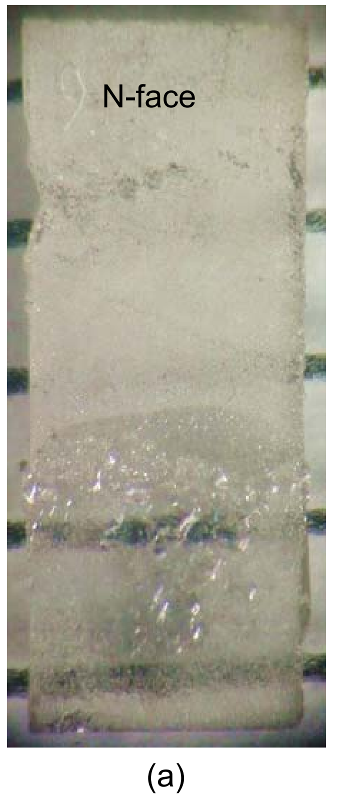

(a)

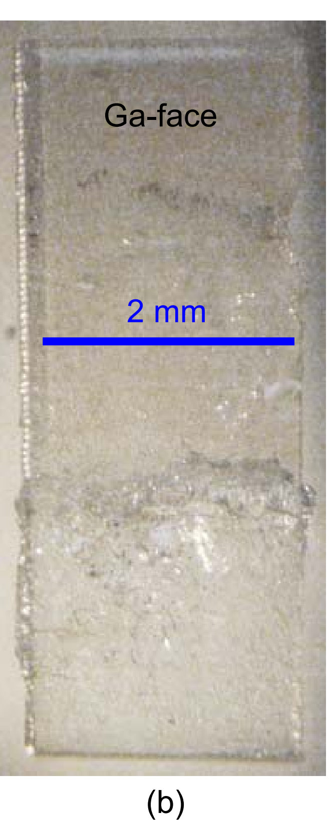

(b)

Figure 22: Photographic images of the HVPE GaN template used as a seed with epitaxially grown GaN layer (a) nitrogen face, (b) gallium face.

Fig. 23 displays an omega-2theta space map of the symmetric (0004) reflection for the Ga-face (a) as-received GaN seed and (b) GaN grown crystal. These measurements were done by M. Mastro of Naval Research Laboratory, Washington DC. The nearly 100-µm thick homoepitaxially grown layer showed a two order-of-magnitude reduction in the full-width-at-half-maximum (FWHM) of the (0004) XRD diffraction peak. FWHM of the X-ray rocking curve measured on both the Ga- and N-face of the sample are 111 and 127 arcsec, respectively, compared to 7740 arcsec and 8820 arcsec for the Ga- and N-face of the GaN seed, respectively.

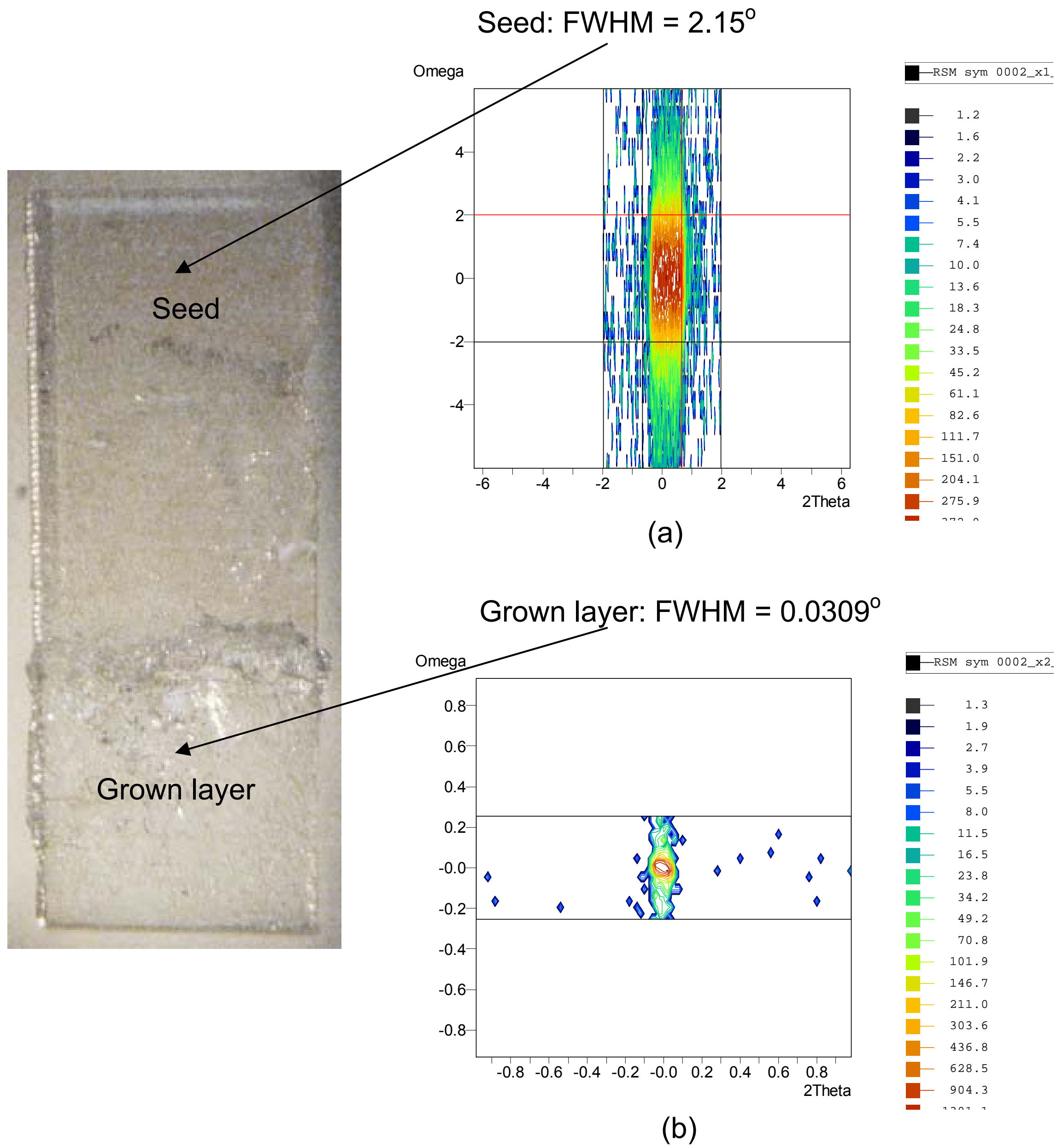

Figure 23: Omega-2theta space map of the symmetric (0004) reflection for the (a) as-received GaN seed and (b) Ga-face of the GaN grown crystal.

Raman spectroscopic (RS) measurements were carried out on the homoepitaxial GaN layer to probe the crystalline quality and residual biaxial strain. The first order Raman spectra of the cross section of the GaN homoepitaxial sample taken at the gallium-face, the nitrogen-face and the substrate, are depicted in Fig. 24. Group theory predicts eight optical modes namely A_1(TO), A_1(LO), two of B_1, E_1(TO), E_1(LO), E_2^1, and E_2^2 [49]. The experimental configuration yields first order phonon modes A_1(TO) at 535.2 cm^{-1}, E_1(TO) at 559.64 cm^{-1}, E_2^2 at 567.72 cm^{-1} , and A_1(LO) at 735.13 cm^{-1} [45]. The weaker E_1(TO) peak may be due to the misorientation of the sample position and microscope depolarization. Analysis of the lineshape and peak position of observed phonon modes confirms good crystalline quality and a stress free GaN epitaxial layer.

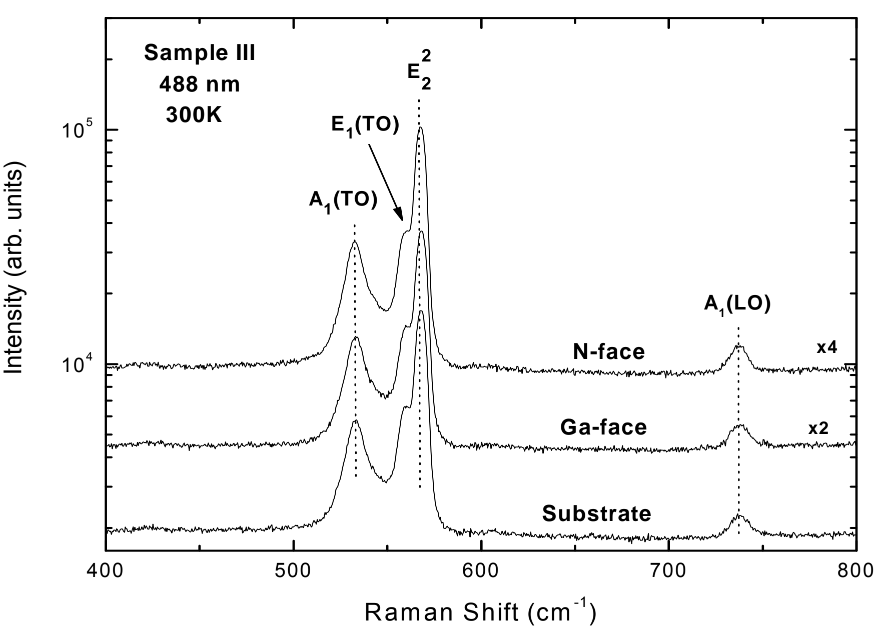

Figure 24: Cross-sectional Raman spectrum of homoepitaxial GaN layer (sample III).

Low resolution PL spectra of the epitaxially-grown GaN layer (Sample III) measured at the bare substrate (#2 – Nitrogen face, #4 – Gallium face) and epitaxial layer regions on both faces of the substrates (#1 – unpolished Nitrogen-face, #3 – polished Gallium-face) are depicted in Fig. 25. These spectra were normalized to minimize the overlapping of the peaks and bands. Note that the dominant NBE peak and its phonon replica (1LO-NBE) are observed at 3.47 eV and 3.37 eV, respectively, on all spectra, similar to the freestanding GaN crystals. A relative increase of PL intensity of the DAP band (3.28 – 3.00 eV) of the layer grown on the nitrogen-face of the substrate, in comparison to that of the substrate, strongly suggests a larger incorporation of shallow acceptors in the nitrogen-polar layer grown on the N-face of the substrate. In contrast, a decrease in the intensity of the DAP of the layer grown on the gallium-face of the substrate indicates lower incorporation of shallow acceptors in the gallium-polar layer in comparison with that of the substrate as well as that of the nitrogen-polar layer. Reduction in the YL bands (2.2 – 2.4 eV) of the layer in comparison with the substrate indicates a decrease in the concentration of the native defects and/or residual impurities [51]. Note that the band observed at ~ 3.41 eV in Fig. 15. and Fig. 20, assigned to emission associated with the annihilation of excitons bound to basal plane SF in the *a*-plane in GaN layers [47,48], is not observed in Fig. 25. This is consistent with *c*-plane growth of the epitaxial GaN layer.

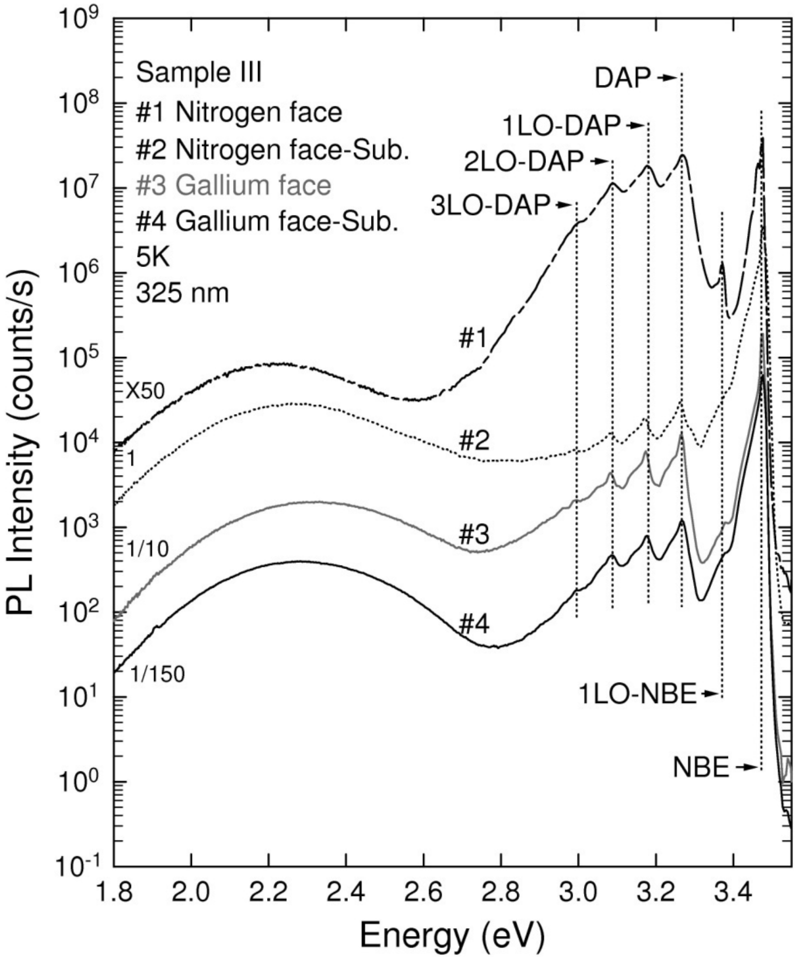

Figure 25: LT PL spectra of homoepitaxial GaN layer (sample III).

To verify the chemical nature of the shallow impurities incorporated in the layer, high resolution PL measurements were performed in the NBE spectral region, and the results are represented in Fig. 26.

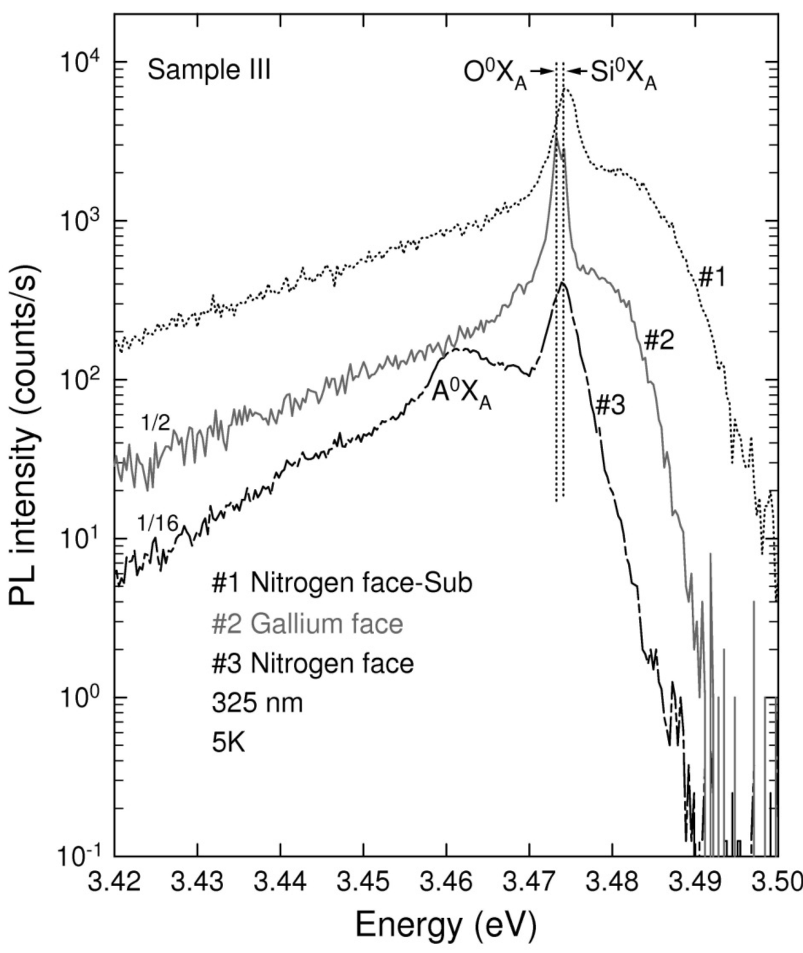

Figure 26: High-resolution PL spectra of homoepitaxial GaN layer (sample III).

This figure shows the band edge PL spectra of the epilayers grown on the gallium-face (#2) and the nitrogen-face (#3), and the spectra of the nitrogen-face of the substrate (#1). The NBE peak is clearly made of two peaks at ~3.47 eV and ~3.46 eV, assigned to D^0X_A and A^0X_A, respectively [45]. Note that the epilayer on the gallium-face shows no evidence of A excitons bound to unknown shallow acceptors (A^0X_A), whereas the one on nitrogen-face shows a relatively intense emission at 3.462 eV [45,46]. There

are two sharp lines, in the case of the gallium-face epilayer spectrum at 3.472 eV and 3.474 eV, indicating that O^0X_A and Si^0X_A are the pervasive dominant shallow donors [31]. The spectrum of the nitrogen-face epilayer shows a broader emission line at 3.474 eV, which suggests higher donor concentration or lower crystalline quality. Smaller FWHM values of O^0X_A and Si^0X_A (0.45 meV for O^0X_A and 0.29 meV for Si^0X_A) are consistent with a lower incorporation of impurities in the gallium-face epilayer. The intense broad band observed at ~3.48 eV has previously been assigned to a high concentration of free electrons [52].

2.2.3 Summary

High quality GaN single crystals have been grown from solution on a GaN seed at nitrogen pressures less than 0.25 MPa and at 800 ^{0}C. The high crystallinity and purity of the crystals were confirmed by XRD, RS and LT PL spectroscopy. These techniques were employed to investigate the structural and optical properties of self-nucleated GaN crystals, crystals grown on HVPE GaN polycrystalline aggregates, and homoepitaxial GaN layers grown from solution at moderate temperature and pressure. LT PL measurements showed sharp and intense D^0X_A peaks indicating good crystalline quality and low free carrier concentration, confirming the results of XRD and RS studies. An emission band at ~3.41 eV, which has been attributed to excitons bound to the basal plane stacking faults is observed in the self nucleated GaN crystals and crystals grown on polycrystalline aggregate GaN crystals. However, this 3.41 eV band is not observed in

the homoepitaxial GaN layer due to *c*-plane growth. Also observed is a significant decrease in the intensity of YL and DAP bands, indicating considerable decrease in the concentration of the native defects and background impurities in the crystals and layers grown by this method. These observations strongly suggest that it is possible to grow high quality epitaxial layers on crystalline GaN substrates.

3. CHARACTERIZATION OF *n*-TYPE GALLIUM NITRIDE FILMS

To date, sapphire and silicon carbide have been the most common substrates for nitride-based optical and electrical devices, since they provide large-area and high-quality bulk material at a relatively low cost. Despite the remarkable progress in the fabrication of opto-electronic devices based on the heteroepitaxial templates, a reduction in the concentration of defects has been an important issue. The concentrations of threading and screw dislocations typically range between 10^6 and 10^{10} cm^{-3} in heteroepitaxial templates. Low concentration of dislocations was obtained in case of a freestanding (FS) hydride vapor-phase epitaxial (HVPE)-grown GaN substrates at around 3 x 10^6 cm^{-2} [53]. Presently, HVPE substrates seem to be the best option for GaN homoepitaxial growth.

The lack of reproducibility in the electrical properties of as-grown films may result from unknown levels of contamination of the precursors and reactors, and changes in the system parameters such as flow, pressure during growth. To reach semi-insulating (SI) character needed for microwave device fabrication, deep level producing impurities, such as Be, C, Zn, and Fe, has been employed by different groups to compensate for the excess shallow *n*-type impurities observed in unintentionally doped (UID) GaN films.

However, the unknown chemical nature and level of background doping of the UID films compel the use of high-level compensation doping, to achieve the degree of compensation necessary to produce SI GaN substrates. This approach can yield substrates with low crystalline quality and poor thermal conductivity, which can affect the performance of nitride-based electronic devices.

For a better understanding of the crystalline quality including the dislocations (threading and screw), a detailed characterization of FS GaN films grown on sapphire substrates by different techniques was performed. In this work, GaN films grown by hydride vapor-phase epitaxy (HVPE), molecular beam epitaxy (MBE), and organo-metallic vapor-phase epitaxy (OMVPE) were considered.

3.1 Experimental samples and approach

Crack-free and freestanding (FS) UID GaN films with thicknesses ranging from 150 to 400 μm have been successfully deposited on sapphire substrates using the HVPE technique by a number of researchers [54-56]. Commonly, 2-in diameter *c*-plane sapphire substrates are placed on a 1030 ^{0}C horizontal susceptor of a hot-wall HVPE reactor to grow the GaN film. The precursor gas GaCl, formed by pre-reacting Ga metal and HCl, is transported by nitrogen carrier gas to the hot growth-zone, where it reacts with NH_3 to deposit GaN on the (0 0 0 1) sapphire substrates at a pressure of 130 Torr. A group V / group III species ratio between 20 and 35 typically results in a growth rate between 30 and 100 μm/h. Films with dislocation density of $\leq 10^7$ cm^{-2} are easily produced. Laser-assisted liftoff technique (e.g., 248nm lie of KrF laser with 20ns pulse-

width and 50Hz pulse rate) is conveniently employed to remove the films from the sacrificial sapphire substrates [57]. A laser beam energy density of 0.2-0.3 J/cm^2 releases the nitrogen from the film to form a thin layer of liquid Ga at the film-substrate interface. Wafer bowing during the laser lift-off process causes fractures, which can be minimized by keeping the GaN/sapphire templates at a temperature near the GaN decomposition temperature. To obtain a flat, smooth grown surface, GaN FS films are mechanically polished, which introduces subsurface damage up to 4000 Å below the surface. Post-growth reactive ion etching or chemical-mechanical polishing processes are employed to remove this damage and obtain epi-growth surface quality [58]. Growth processes of the samples used in this work are reported elsewhere [59].

The samples used for this study are:

Sample #1: Si-doped GaN deposited on FS-HVPE GaN substrate by OMVPE technique,

Sample #2: UID (oxygen background) GaN deposited on FS-HVPE GaN substrate by MBE technique, and

Sample #3: FS HVPE GaN (reference sample)

To verify the chemical nature of shallow donors and to estimate their concentration, systematic investigations have been carried out on UID and Si-doped GaN films grown by chemical vapor deposition and molecular beam epitaxy. High-resolution low-temperature photoluminescence (PL) measurements were performed on GaN films analyzed by high sensitivity secondary ion mass spectroscopy (SIMS).

Preliminary luminescence measurements were carried out on a number of FS-HVPE substrates for selection of suitable substrate for UID and Si-doped epilayers. Fig. 27 depicts the high resolution PL spectra acquired from two substrates (named as substrate #1 and #2) with a thickness of ~200 μm used for homoepitaxial growth, in the spectral region near the bandedge. The spectra for both substrates are dominated by intense emission bands associated with the annihilation of excitons bound to neutral donors D^0X (also represented as XD^0) at 3.47 eV with their phonon replicas (1LO- D^0X) at 3.37 eV. Based on the line-width and relative intensity of the individual emission bands, its clear that these substrates show good crystalline quality and low background impurity concentration [60,61]. Due to its good crystalline quality, these substrates were subjected to UID and Si-doped MBE and OMVPE growth processes, respectively.

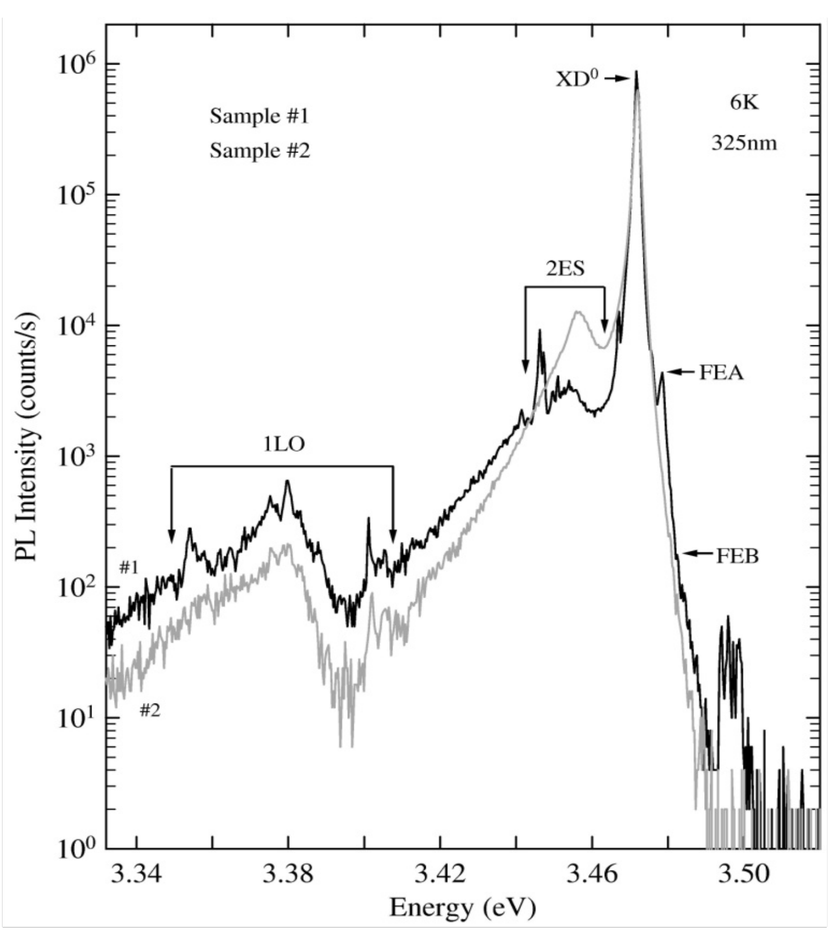

Figure 27: Low temperature high-resolution PL spectra of the two typical HVPE substrates, which were subjected to epi-growth processes.

3.2 Surface morphology of a UID and Si-doped GaN

Atomic force microscopy (AFM) of a 5µm x 5µm UID GaN homoepitaxial film grown on FS-HVPE substrate grown by MBE technique (sample #2) is shown in Fig. 28. Tapping mode AFM measurements revealed that the surface between gallium droplets was extremely smooth with clearly visible atomic steps. The observed nominal roughness of 8 Å indicates that it is possible to grow high quality films with reduced defect

concentrations. The OMVPE Si-doped homoepitaxial films with thickness of about 5 μm are characterized by reduction in threading dislocation density of ~5 x 10^6 cm^{-2} [60,62] and improved growth surface roughness of ~ 2 Å, as compared with the substrate. These low roughness values confirm the potential of these homoepitaxial films for device fabrication.

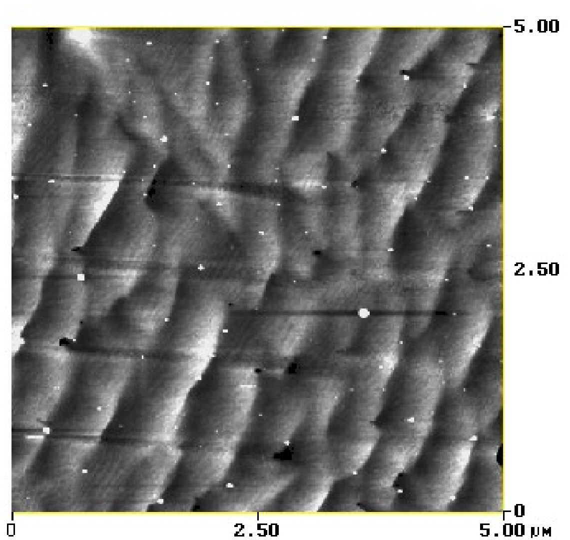

Figure 28: AFM of UID GaN deposited on FS-HVPE GaN substrate by MBE technique.

3.3 Secondary ion mass Spectrometry

High-resolution SIMS measurements were performed by Evans Analytical group, CA, to determine the concentration of the impurities in the epilayers. High resolution SIMS profile measurements were acquired on the samples after the growth process. SIMS measurements carried out on the OMVPE Si-doped homoepitaxial film,

represented in Fig. 29, a show that the target concentration of ~1.5 x 10^{17} atoms/cm^3 was achieved, which is well above the detection limit (~4 x 10^{14} atoms/cm^3). As expected, for the films grown by OMVPE, an increase of the carbon (C) concentration was observed in the epitaxial film as compared to that of the substrate. It was found that oxygen (O), which has a concentration ~8.8 x 10^{15} atoms/cm^3 in the film, was close to its detection limit. The concentrations of Si, O, and C in the homoepitaxial film in comparison with the substrate are shown in Table II.

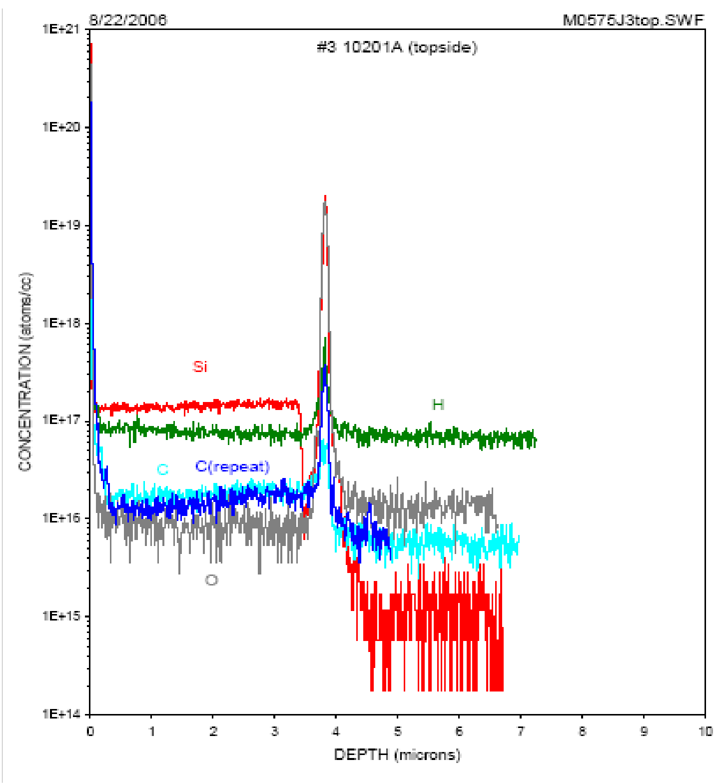

Figure 29: SIMS depth profiles of the GaN homoepitaxial film grown by OMVPE on FS- HVPE GaN substrate (Si: OMVPE/HVPE-FS).

Table II: SIMS data on OMVPE GaN film grown on HVPE- FS GaN substrate, showing the concentration (cm^{-3}) of Si, O and C in the substrate and in the film.

	"Si"	**"O"**	**"C"**
Film	$1.5x10^{17}$	$8.9x10^{15}$	$1.8x10^{16}$
Substrate	$1.3x10^{15}$	$1.4x10^{16}$	$6x10^{15}$

Similarly, SIMS measurements carried out on the unintentionally doped MBE homoepitaxial film, depicted in Fig. 30, shows a higher level of O than that in the HVPE substrate. The source of O doping is presently unknown. The C concentration remains about the same in both the film and the substrate. The Si concentration in this MBE homoepitaxial film is about the detection limit too. The concentration of Si, O, and C in the homoepitaxial film and in the substrate is given in Table III.

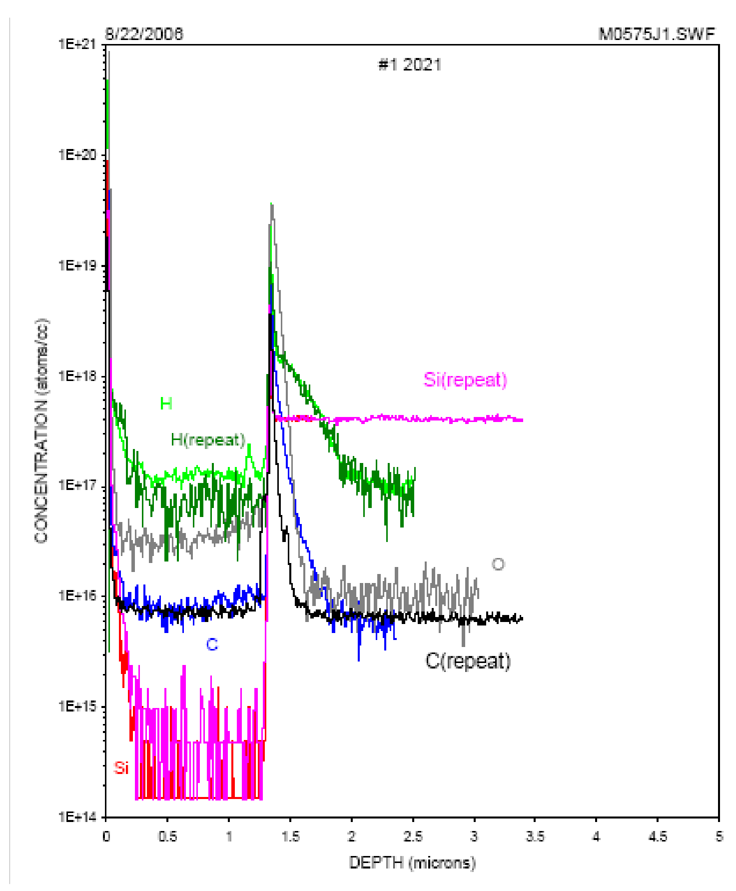

Figure 30: SIMS depth profiles of the homoepitaxial film deposited on a FS-HVPE GaN substrate by RF-plasma-assisted MBE technique (UID-O:MBE/HVPE-FS).

Table III: SIMS data of UID- MBE GaN film grown on HVPE-FS GaN substrate with concentrations (cm^{-3}) of Si, O and C in the substrate and in the film.

	"Si"	"O"	"C"
Film	4.5×10^{14}	3.3×10^{16}	7.3×10^{15}
Substrate	4×10^{17}	1×10^{16}	6.6×10^{15}

3.4 Photoluminescence Spectroscopy

Fig. 31 shows the low temperature PL spectra covering the spectral range between 3.441 and 3.484 eV for the two homoepitaxial films (sample #1, #2) analyzed by SIMS along with the spectrum on FS- HVPE GaN substrate (sample #3). The PL spectrum of the substrate (sample #3, reference sample) shows three dominant peaks at 3.4716, 3.4721, and 3.4723 eV. The three dominant peaks have been previously assigned to excitons bound to neutral O donors, unknown donors and neutral Si donors, respectively [31]. The PL spectrum of the Si-doped homoepitaxial film (sample #1) shows a large increase in the intensity and the full-width at half-maximum of the emission band around 3.472 eV, which is very close to the line assigned to Si donors, in the spectrum of sample #3. Also, the PL spectral range covers the region associated with the recombination process associated with the annihilation of the free-excitons (FE), where holes originate from the valance band A (FX_A). A strong reduction in the line intensity of the FX_A peak is observed as compared with the spectrum of sample #3. These PL changes are consistent with a large excess concentration of neutral donors in the epi, as compared with the concentration of donors in sample #3, i.e., the HVPE-GaN substrate. The contribution of the O-related PL line seems to be very small, which is in good agreement with the SIMS measurements indicating a low concentration of O donor background in the OMVPE homoepitaxial film. The PL spectrum of the MBE homoepitaxial film (sample #2) is dominated by a single line near the spectral position assigned for excitons bound to neutral O donors (O^0X), as highlighted for the spectrum

#3. Note that the relative intensity of the FX_A, as compared with that of the spectrum #3, is reduced, indicating a larger concentration of neutral donors. The SIMS analysis detects a larger concentration of O in the UID MBE GaN film than that observed for the FS-HVPE substrate. Note that the PL emission line intensity associated with the Si impurity is strongly reduced suggesting that O is the dominant shallow neutral donor impurity in this film, also in agreement with the SIMS measurements. These results confirm the identification of Si and O as the pervasive dominant shallow donors in GaN as proposed by *Moore et al.* and by *Freitas et al.* [7,31]. This spectrum also shows a relatively intense emission line near 3.467 eV, represented by A^0X, previously associated to excitons bound to an unknown shallow impurity [46].

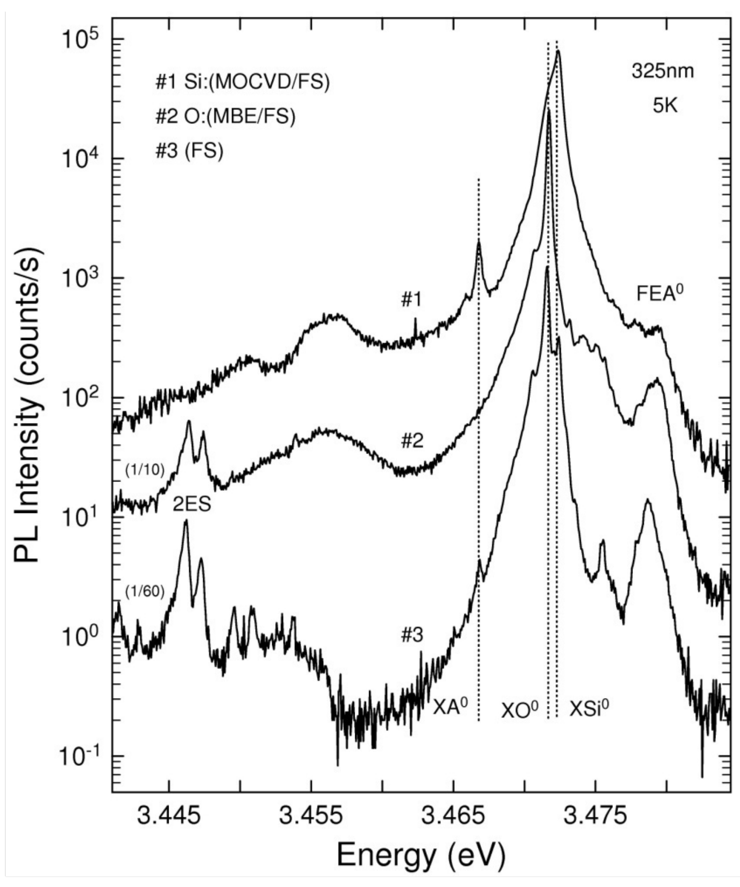

Figure 31: Low temperature PL spectra of the Si-doped OMVPE (Si: OMVPE/HVPE-FS) and the UID MBE (UID-O: MBE/HVPE-FS) homoepitaxial GaN films. The spectrum of an HVPE-FS GaN reference substrate is also shown.

Also observed in the spectra of samples #2 and #3 are the lines represented by two-electron satellite (2ES). The 2ES transitions refer to the spectral lines resulting from radiative recombination of the exciton(s) bound to a donor(s), leaving the donor(s) in an excited state after their annihilation [31] as shown in Fig. 32. The sample, which was intentionally doped with Si (sample #1) clearly shows a broad spectra at energy 3.450 eV

where as the sample, which was UID – with impurity trace of O (sample #2), shows two intense peaks at ~ 3.445 eV and ~ 3.450eV. The peaks observed at ~ 3.445 eV and ~ 3450 eV may be related to O and Si, respectively. Additional studies are required to understand the nature of the this broad peak.

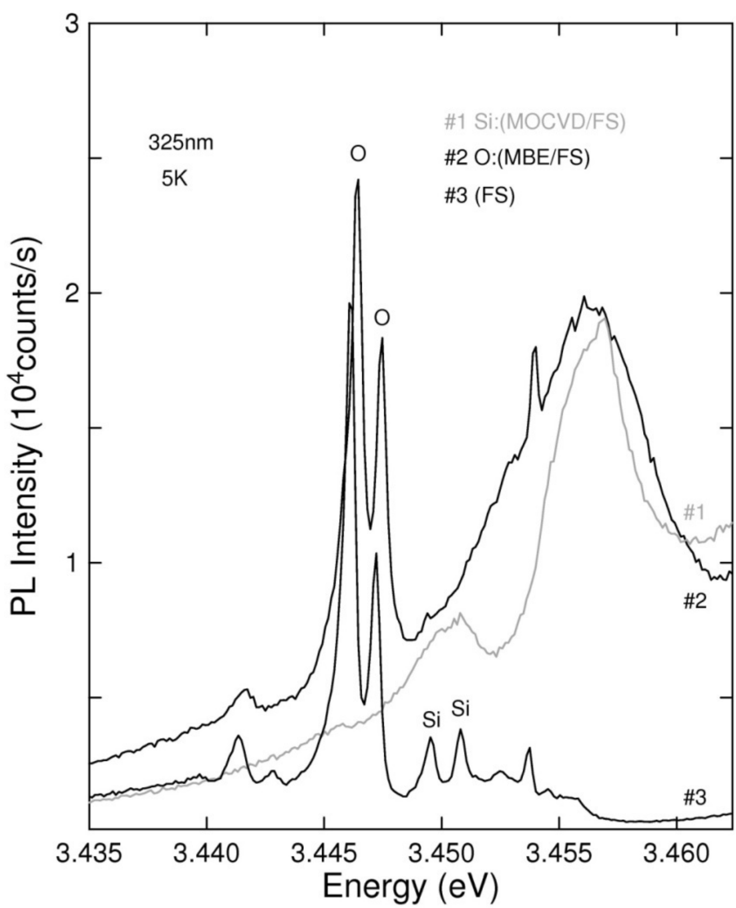

Figure 32: Spectra taken at 5K in the 2ES region of all three samples.

Fig. 33 depicts the emission line associated with the annihilation of excitons bound to an unknown shallow acceptor, represented by A^0X in Fig. 31. We observed a

linear dependence of the line intensity with the laser excitation intensity, which suggests an excitonic transition character for the recombination process. The intensity of the A^0X line seems to increase with Si doping, as observed by comparing the spectrum of sample #1 with that of sample #3.

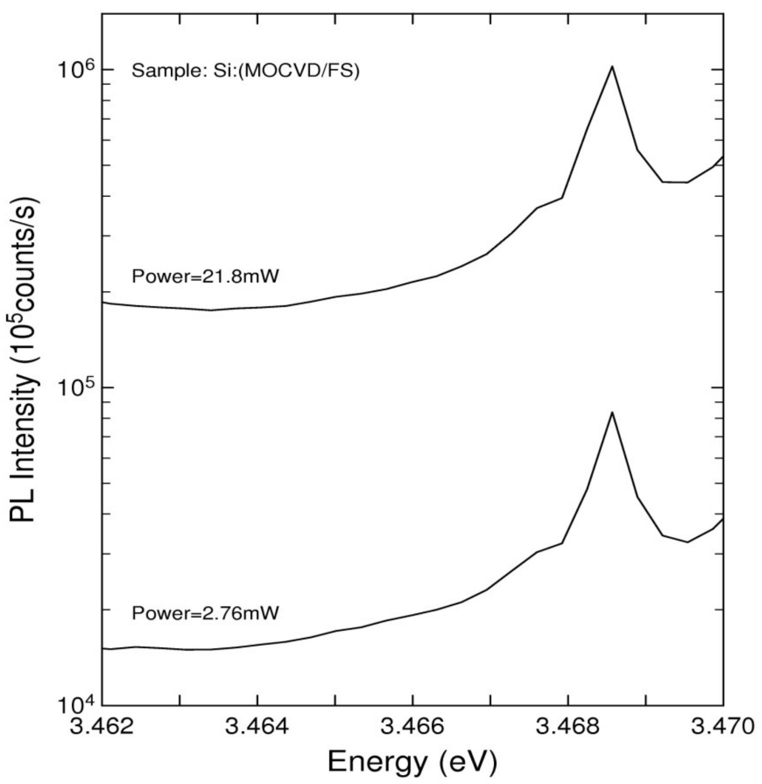

Figure 33: PL spectrum of the Si: OMVPE/HVPE-FS GaN sample showing the A^0X intensity dependence with power excitation.

3.5 Summary

Detailed low-temperature PL and high-sensitivity SIMS experiments on FS-HVPE GaN substrates and homoepitaxial films deposited by MBE and OMVPE support the chemical identification of Si and O as the dominant pervasive shallow donors in GaN films. The PL peaks associated with the Si and O donors are clearly identified. Hence, the residual donors in epitaxial layers can be easily identified by non-destructive PL techniques from now on.

4. CHARACTERIZATION OF *p*-TYPE GALLIUM NITRIDE FILMS

To investigate the acceptor activation in GaN, two different studies were performed. In the first set of experiments, impact of high dislocation densities, caused by high Mg doping level (10^{17} - 10^{20} cm^{-3}), on the optical and spin properties of the Mg acceptors were studied. In the second set, activation of Mg/ Be in Mg in-situ doped, Be in-situ doped and Mg ion-implanted GaN samples subjected to microwave annealing in the temperature range of 1300 – 1500 ^{0}C for 5 – 15s was studied.

4.1 Study of Mg-doped GaN homoepitaxial layers grown by MBE

The nature and properties of Mg shallow acceptors and Mg-related or -induced deep centers in the III-V nitrides have been subjects of much experimental and theoretical investigation during the last 15 years. Most of this research has focused on highly Mg-doped (~ 10^{18} – 10^{20} cm^{-3}) GaN layers grown on foreign substrates, such as sapphire and SiC, characterized by high dislocation densities (~ mid 10^{8}–10^{10} cm^{-2}) that result from differences in the lattice constants and thermal expansion coefficients of the respective nitride films and underlying host substrates. In particular, many photoluminescence (PL) studies of Mg-doped heteroepitaxial GaN have revealed a variety of near-infrared and visible emission bands, including a so-called “red” PL band near 1.8 eV, broad “blue” PL

bands with peak energy between 2.8 and 3.2 eV, and a PL band at 3.27 eV with resolved LO phonon replicas attributed to recombination between residual shallow donors (SD) and Mg shallow acceptors (SA) [6]. In addition, both electron paramagnetic resonance (EPR) and optically-detected magnetic resonance (ODMR) techniques have been employed to identify residual defects and gain more information on the nature of the Mg-related states [63,64]. One of the big puzzles common to all the magnetic resonance work was the nearly isotropic g-tensor (i.e., $g_{\|}$, $g_{\perp}$ ~2) found for the Mg shallow acceptors in the highly dislocated and highly Mg-doped GaN layers.

Combined PL and ODMR experiments have been performed on a set of Mg-doped (10^{17}-10^{20} cm^{-3}) GaN layers deposited by molecular beam epitaxy (MBE) on thick, free-standing GaN substrates characterized by dislocation densities less than $5x10^6$ cm^{-2}. This study allowed separating the impact of high dislocation densities from effects due to high Mg doping levels, on the optical and spins properties of the Mg acceptors. To date, the most important acceptor-dopant employed for making *p*-type GaN is Mg. Most notably, ODMR on the 3.27 eV shallow donor-shallow acceptor (SD – SA) PL band (also known as DAP band) from a GaN homoepitaxial layer with [Mg] of ~$1x10^{17}$ cm^{-3} provided the first observation of the highly anisotropic g-tensor (i.e., $g_{\|}$ ~ 2-4, $g_{\perp}$ ~ 0) expected for Mg shallow acceptors based on k•p theory and the ordering of the valence band states in wurtzite (wz)-GaN [65].

4.1.1 Experimental Details

The PL and ODMR were performed on several Mg-doped GaN homoepitaxial layers (0.5-0.7 μm-thick) deposited by MBE on Fe-doped, free-standing GaN substrates (~ 1 cm x 1 cm, 200 μm-thick) grown by HVPE [25]. The GaN films were intentionally doped with Mg from 10^{17}–10^{20} cm^{-3} as confirmed by secondary ion mass spectroscopy (SIMS) [66]. An undoped GaN homoepitaxial film was also investigated to serve as a reference. Prior to growth of the GaN:Mg films, a 0.7 μm-thick Be-doped (~$3x10^{19}$ cm^{-3}) buffer layer followed by an un-doped 0.2 μm GaN layer were deposited. The Be-doped layer helped to insure electrical isolation of the Mg-doped GaN layers [67]. Further details of the growth are provided elsewhere [21].

Several electrical and structural characterization techniques were also employed on these samples. For example, room-temperature Hall effect on a representative GaN homoepitaxial layer with Mg level of $2x10^{19}$ cm^{-3} revealed a hole concentration of ~10^{18} cm^{-3} with a mobility of 11 $cm^2/(V\ s)$. In addition to Mg depth profiles, SIMS revealed O levels of ~$6x10^{16}$ cm^{-3} and Si below the detection limit of $5x10^{14}$ cm^{-3}; common residual shallow donor impurities found in both MOCVD- and MBE-grown GaN. Atomic force microscopy showed typical rms surface roughness values of 5-10 Å. Finally, plan-view transmission electron microscopy (TEM) performed on the GaN homoepitaxial layer with [Mg] of $1x10^{17}$ cm^{-3} revealed a threading dislocation densities $\leq 5x10^6$ cm^{-3} over 5 μm x 5 μm areas.

The high-resolution PL at the GaN bandedge was excited by the 325 nm line of a HeCd laser and analyzed by 0.85-m double-grating spectrometer. The near band-edge and deep visible PL (2.0-3.3 eV) was generated by the 351 nm line of an Ar^+ laser and analyzed by a 0.25-m double-grating spectrometer. In both cases the emission was detected by GaAs PMT detectors. The ODMR was performed at 24 GHz with the samples rotated in the (1 1 2 0) plane to obtain symmetry information [This was performed by E. Glaser at Naval Research Laboratory, Washington DC]. A UV blocking filter was placed in front of the Si photodiode employed in the ODMR for detection of the below bandgap emission.

4.1.2 Photoluminescence Spectroscopy

The bandedge low-temperature (5K) PL spectra of two lowest Mg-doped GaN homoepitaxial layers and an undoped GaN sample are shown in Fig. 34. The dominant emission (labeled O^oX_A) observed from the undoped reference GaN film at 3.472 eV is due to annihilation of excitons (involving holes from valence band A) bound to shallow O [62]. This feature is also observed in the GaN:Mg layers and is consistent with the SIMS results that show O as the dominant residual shallow donor species in these layers. The additional line (labeled Mg^oX) observed at 3.467 eV from the two Mg-doped GaN films is attributed to recombination of excitons bound to neutral shallow Mg acceptors. Its narrow linewidth of 0.2-0.4 meV indicates the high crystalline quality of these samples. This feature is similar to that previously reported by *Stepniewski et al.* [68] for

MOCVD-grown Mg-doped GaN homoepitaxial layers deposited on GaN bulk crystals. It should be noted that the small energy shifts (< 0.5 meV) for the O^oX_A and Mg^oX PL lines from these Mg:GaN layers are likely due to slight differences in residual strain.

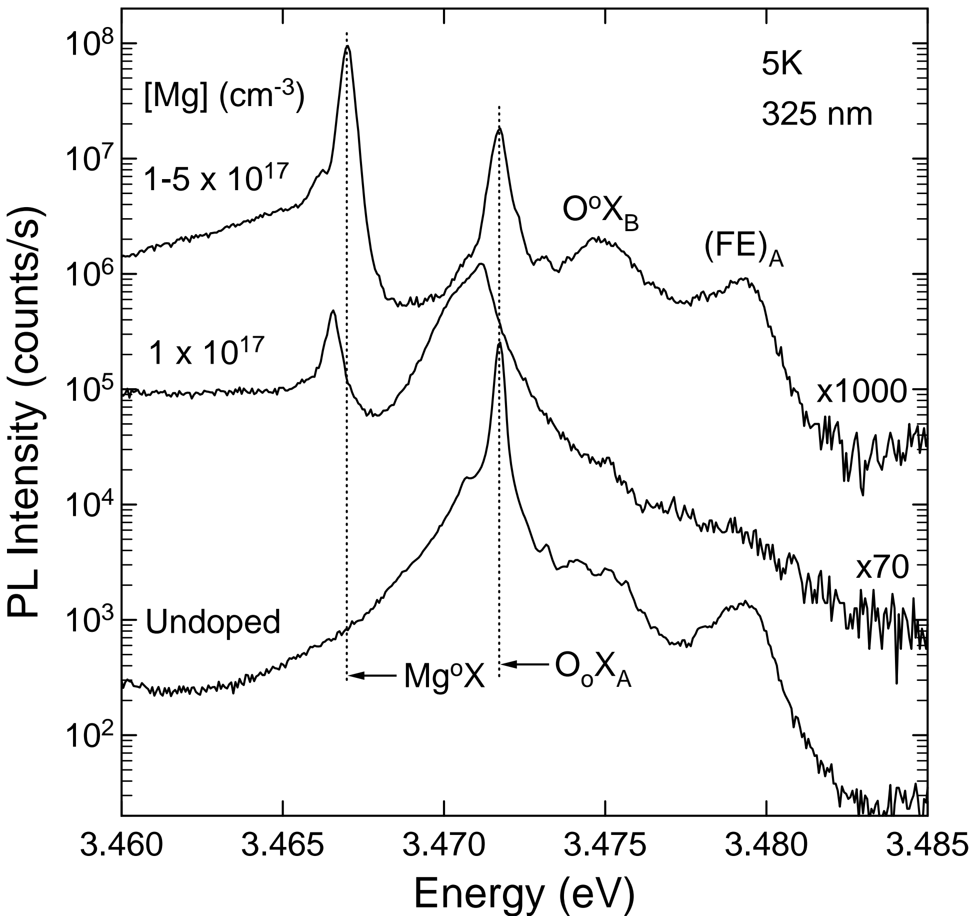

Figure 34: 5K high-resolution PL in the near band edge spectral region of two Mg-doped GaN homoepitaxial films and one undoped GaN homoepitaxial reference layer. The spectra are displaced vertically for clarity.

The low-temperature (2K) PL spectra (< 3.4 eV) observed from several GaN homoepitaxial films with Mg doping levels of 10^{17}–10^{20} cm^{-3} is shown in Fig. 35. In contrast to many previous reports in the literature for MBE- and MOCVD-grown Mg-doped GaN heteroepitaxial layers with [Mg] ≥ $3x10^{18}$ cm^{-3}, no evidence was found for the so-called broad "blue" emission band with energy between 2.8 and 3.2 eV. Instead, all samples exhibited strong SD-SA recombination with zero phonon line at ~3.27 eV and a series of LO phonon replicas. We note the pronounced narrowing of this emission from the samples with Mg doping near $1x10^{17}$ cm^{-3}. This behavior is attributed to both the reduced dislocation density and low Mg impurity concentration. The additional partially resolved feature at ~ 33 meV below the 3.27 eV SD-SA (DAP) ZPL (and LO phonon replicas) for the two lowest Mg-doped samples is similar to that first observed by Dingle and Ilegems [69] in un-doped (*n*-type) GaN samples. It is suggested to be due to a second SD-SA (DAP) recombination system.

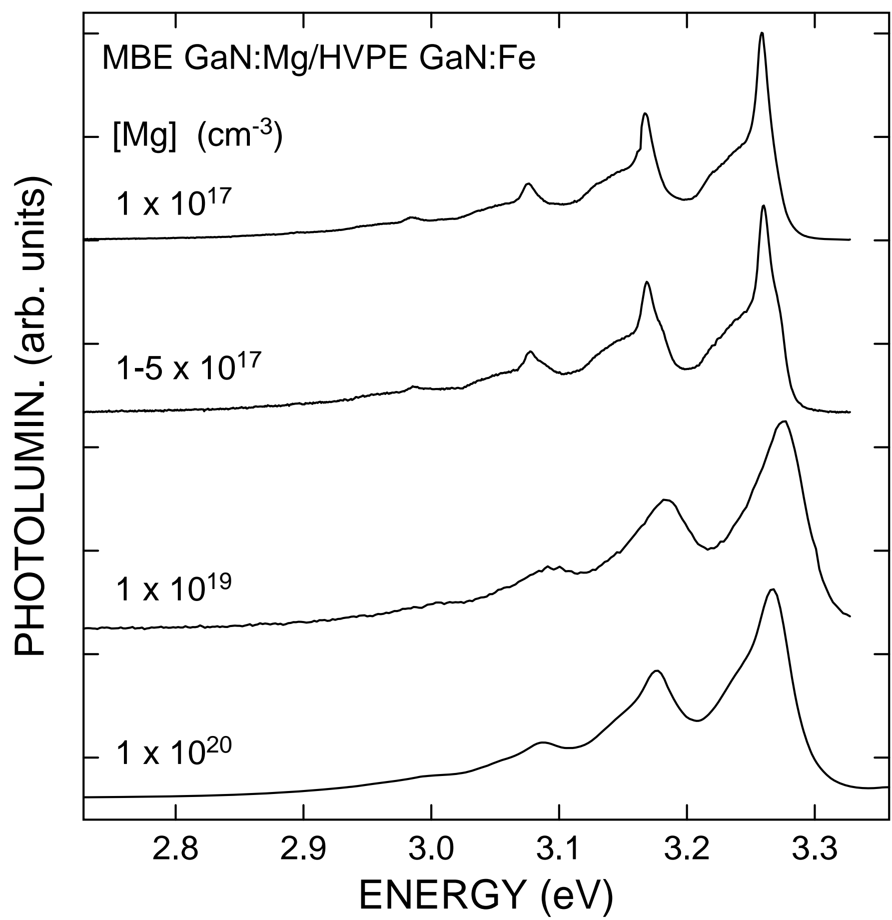

Figure 35: PL (< 3.4 eV) recorded at 2K from several Mg-doped GaN homoepitaxial layers.

4.1.3 Optically detected magnetic resonance

Optically detected magnetic resonance obtained on the 3.27 eV SD-SA (DAP) PL from the GaN homoepitaxial layer with [Mg] = 1×10^{17} cm^{-3} for several orientations of the magnetic field (**B**) with respect to the *c*-axis is shown in Fig. 36. Two luminescence-increasing signals are found. The first (labeled SD) is sharp (FWHM ~ 3.5 mT) with $g_{\|}$, $g_{\perp}$ ~ 1.950 and is a signature of effective-mass shallow donors in GaN [63]. It is assigned to residual O SD on the N sites from the high-resolution PL and SIMS measurements as shown in Ref. 63.

The second feature (labeled Mg_{Ga}), which is broader (FWHM ~ 20 mT for angles ≤ 25°), is weakly observed for **B** within 10° of the *c*-axis and, most notably, shifts rapidly to higher field as **B** is rotated away from the *c*-axis (especially for angles > 20°). In addition, a noticeable asymmetric broadening to the low-field side of this peak is observed for angles ≥ 25°. A plot of the *g*-values (triangles) of this resonance as a function of the angle (θ) between **B** and the *c*-axis is shown in Fig. 37. A fit to this data was made with the usual expression for g-tensors in the case of axial symmetry: $g(\theta)=(g_{\|}^2\cos^2\theta + g_{\perp}^2\sin^2\theta)^{1/2}$, where $g_{\|}$ and $g_{\perp}$ are the *g*-values with **B** parallel and perpendicular to the *c*-axis, respectively. A good fit is found with $g_{\|}=2.19\pm0.01$ and $g_{\perp}\sim0$. This highly anisotropic g-tensor is predicted from effective mass theory [65] for shallow Mg acceptors in wz-GaN where the ground state, from symmetry arguments, reflects the character of the $J=3/2$, $m_J=\pm3/2$ valence band edge.

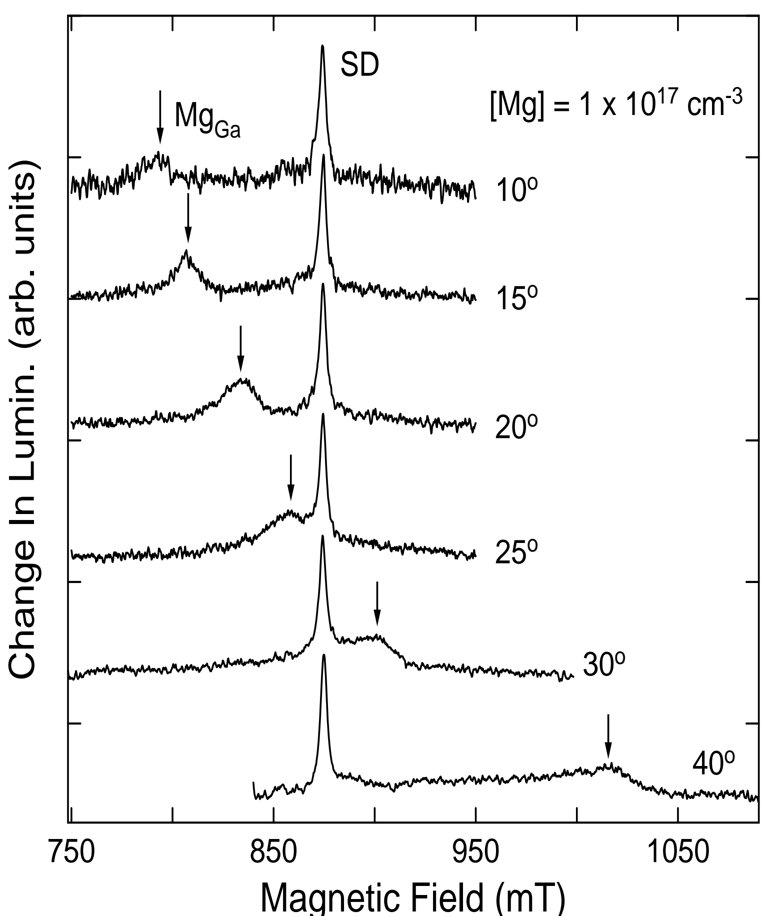

Figure 36: ODMR spectra at 24 GHz observed on the 3.27 eV SD-SA (DAP) PL from a homoepitaxial GaN layer doped with [Mg] of 1 x 10^{17} cm^{-3} for several orientations of **B** with respect to the c-axis.

This previously elusive result via magnetic resonance techniques is attributed to the much reduced dislocation densities and Mg impurity concentrations compared to those typically found in the widely investigated [6] Mg-doped GaN heteroepitaxial

layers. This is demonstrated explicitly in Fig. 37 by the nearly isotropic *g*-values (squares) observed for the shallow Mg acceptors via ODMR on the 3.27 eV SD-SA (DAP) PL from a GaN heteroepitaxial layer with Mg-doping level of $3x10^{18}$ cm^{-3} grown on Al_2O_3 [70]. It is to be noted that ODMR was not found on the 3.27 eV SD-SA (DAP) recombination from the GaN homoepitaxial films with Mg doping ≥ 10^{19} cm^{-3}. This can be attributed to the small average donor-acceptor pair separation (e.g., ~ 30Å for [Mg] of 10^{19} cm^{-3} compared to ~ 130 Å for [Mg] of 10^{17} cm^{-3}) in such samples that result in recombination lifetimes that are too fast to alter spin populations for the microwave powers (~50 mW) available in these ODMR experiments.

Finally, ODMR was recently reported for the SA involved in the 3.27 eV SD-SA (DAP) PL from a GaN homoepitaxial layer intentionally doped with Si ($2x10^{17}$ cm^{-3}) [71]. The Si-doping studies as described by Freitas et al. in Ref. [31] strongly indicated that the SA in this case were due to some fraction of the Si impurities taking the N host lattice sites. Most noteworthy, in addition to the similar excitonic emission energies of ~ 3.467 eV, the magnetic resonance characteristics of this feature (including the highly anisotropic *g*-tensor as shown by the circles in Fig. 37 and the asymmetric broadening behavior observed with **B** rotated ≥ 25° from the *c*-axis) are nearly identical with those found in this work for the Mg SA on the Ga sites.

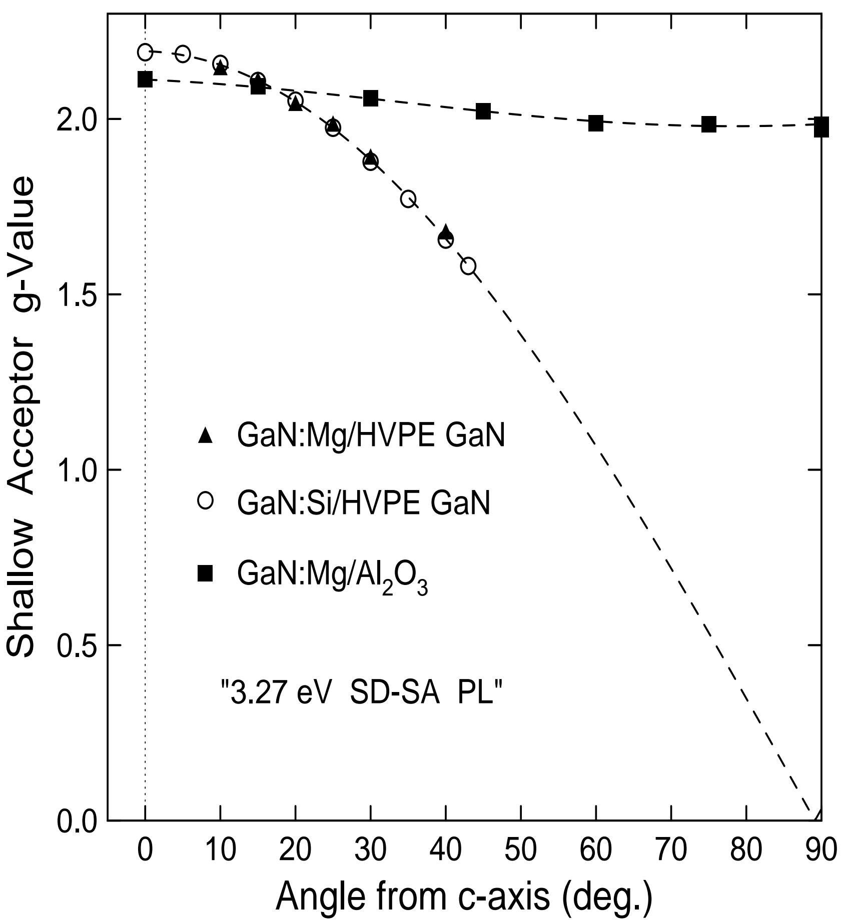

Figure 37: g-values of ODMR feature Mg_{Ga} in this work (triangles) and those reported previously for shallow acceptors in Si-doped GaN homoepitaxial layers (circles) and for Mg shallow acceptors in Mg-doped GaN heteroepitaxial films (squares). Dashed curves are fits to the data as described in the text.

4.1.4 Summary

PL and ODMR have been performed on several GaN homoepitaxial layers doped with Mg from 10^{17} to 10^{20} cm^{-3}. In addition to strong emission at ~3.467 eV attributed to annihilation of excitons bound to shallow Mg acceptors, each sample exhibited SD-SA (DAP) recombination at 3.27 eV with no evidence for other deep visible PL bands. ODMR on this emission from the lowest Mg-doped sample revealed the first evidence for the highly anisotropic g-tensor predicted for effective-mass Mg acceptors in wz-GaN. Surprisingly, the characteristics of this feature are very similar to those found recently from ODMR of Si shallow acceptors on the Ga host lattice sites.

4.2 Microwave annealing of *in-situ* Mg doped GaN films grown by MOCVD

The problem associated with obtaining highly conductive p-type layers has become a bottleneck for the development of efficient III-nitride optical, high-power, and high-temperature devices [72]. High annealing temperatures (> 1200 ºC) are required for optimally activating *in-situ* and more specifically ion-implantation doped acceptors were later used for healing the lattice damage in ion-implanted GaN [72,73]. However, the GaN is not thermally stable, when exposed to temperatures > 900 ºC for any length of time, at a standard pressure of 0.1 MPa [74]. Hence, to preserve the GaN surface morphology, the required high annealing temperature (> 1200 ºC) should be reached very fast and the duration of anneal should be limited to few seconds. Existing rapid thermal annealing (RTA) techniques, based on tungsten-halogen lamps are primarily designed for Si and GaAs technologies [75]. The maximum temperature of the halogen lamp RTA systems is limited to 1250 ºC due to the quartz hardware used in these systems [72,75]. Resistively or inductively heated ceramic furnaces are capable of much higher operating temperatures, but due to their large thermal masses, the temperature ramping rates of such furnaces are very modest (few ºC / min). Promising results were obtained after annealing AlN capped, ion-implanted GaN in the temperature range of 1300 – 1400 ºC, by a RTA system [72,76] based on molybdenum intermetallic composite heaters. This system is capable of 50 ºC/s heating rates. However, the GaN surface acutely deteriorated when annealing temperatures crossed 1400 ºC. Thus, clearly there is a need for a RTA system capable of heating rates > 50 ºC/s to efficiently anneal GaN at temperatures

> 1400 ºC. The lack of such a RTA technique has thus far hampered the advancement of ion-implantation technology in GaN material system, which is critical for the development of high-performance, planar GaN electronic devices. Chang et al. [77] have reported on acceptor activation in Mg (in-situ) doped GaN after a 2.4 GHz, 560 W, low-temperature microwave treatment. They speculate that the absorbed microwave energy breaks the passivating Mg-H complexes, thereby resulting in Mg activation. However, such low-temperature annealing treatments may not be successful, when applied to ion-implanted GaN, since high-temperatures (> 1300 ºC) are required for alleviating the lattice damage introduced by ion-implantation in GaN.

A microwave rapid thermal annealing (RTA) technique has been recently developed for annealing ion-implanted SiC at temperatures in excess of 2000 ºC with ultra-fast temperature ramping rates of 500 ºC/s [78-80]. In this thesis work, the use of this microwave RTA technique has been extended for annealing GaN at temperatures in the range of 1300 – 1500 ºC for durations of 5 -15 s.

4.2.1 Experimental details

Samples explored in this study were 3μm thick Mg-doped, *c*-plane GaN epilayers grown by metalorganic chemical vapor deposition (MOCVD) on *a*-plane sapphire substrates [81]. For heating the GaN sample, a 5 mm x 5 mm highly conducting 4H-SiC piece is placed directly underneath the GaN sample of interest to serve as the susceptor, where both the GaN sample and the SiC piece are placed within the microwave heating head. Microwave annealing of GaN is performed with and without a surface capping

layer composed of MgO, AlN or graphite. AlN caps have successfully protected the GaN surface up to temperatures of 1300 ºC and 1400 ºC, for conventional furnace annealing [14] and RTA [72,76], respectively. The AlN layers (200 nm thick) were deposited on the GaN sample using pulsed-laser deposition [82]. The MgO layers (200 nm and 100 nm thick) were deposited on the GaN using electron beam evaporation of a MgO target. Fused lumps of MgO (Alfa Aesar, 99.95%, metals basics, 3-12 mm pieces) were used as target material. Graphite caps are formed on the GaN epilayers by first spin-coating a layer of standard photoresist, followed by annealing in vacuum at 750 ºC. Microwave annealing is performed in the temperature range of 1300 – 1550 ºC for short 5 s and 15 s durations in a pure (99.999%) nitrogen atmosphere. After microwave annealing, the MgO cap is easily removed by etching in dilute acetic acid, whereas the AlN cap is removed by a 10 min etch in 85 wt% H_3PO_4 at 80 ºC.

The reliable application and removal of the AlN cap on the GaN surface was studied at Dr. Schrifel's laboratory using x-ray photoelectron spectroscopy (XPS), which were acquired using a Mg Kα x-ray source. For details about the XPS system, please refer to Ref. 78. The sample surface after annealing and removal of the cap is monitored by tapping mode atomic force microscopy (AFM). Structural characterization is performed at Dr. Qadri's Lab at Naval Research Laboratory using high resolution X-Ray diffraction (HRXRD) and rocking curve measurements. The optical characterization of the material is performed using low-temperature (5K) photoluminescence (PL) spectroscopy. For obtaining the PL spectra, a He-Cd laser was used with an excitation intensity of 2.5 mW. For more details about the PL system, refer to Ref. 45. Room-

temperature Hall measurements were performed after depositing (30 nm) Ni / (30 nm) Au contacts on the GaN layers in the van der Pauw geometry. The contacts were made ohmic by alloying in a conventional box furnace at 550 ºC, in air, for 10 min.

4.2.2 X-Ray Photoelectron Spectroscopy

The reliability of the application, sustainability of the AlN cap during annealing, and removal of the AlN cap after microwave annealing was studied by XPS. A survey XPS scan of the surface of the AlN as-capped sample is shown in Fig. 38(a). Other than O 1s and C 1s signals coming from the native oxide/hydrocarbon layer, only Al and N signals can be seen in the survey scan. The survey XPS scan of the AlN capped sample after 1400 ºC / 5 s microwave annealing is shown in Fig. 38(b). Surprisingly, no nitrogen signal can be detected from this scan but a rather strong O 1s signal is seen in addition to the Al signal. Narrow scans (not shown) of the O 1s peak were consistent with the presence of either Al_2O_3 or $Al(OH)_3$ [83]. Thus, upon microwave annealing, the AlN film has oxidized and formed Al_2O_3 and/or $Al(OH)_3$. This is in spite of the fact that the annealing was done in an atmosphere of UHP nitrogen, which emphasizes the strong oxidation affinity of the AlN film. A similar result was obtained after microwave annealing at 1500 ºC / 5 s. A survey XPS scan of the sample after 1400 ºC microwave annealing and removal of the cap by H_3PO_4 is shown in Fig. 38(c).

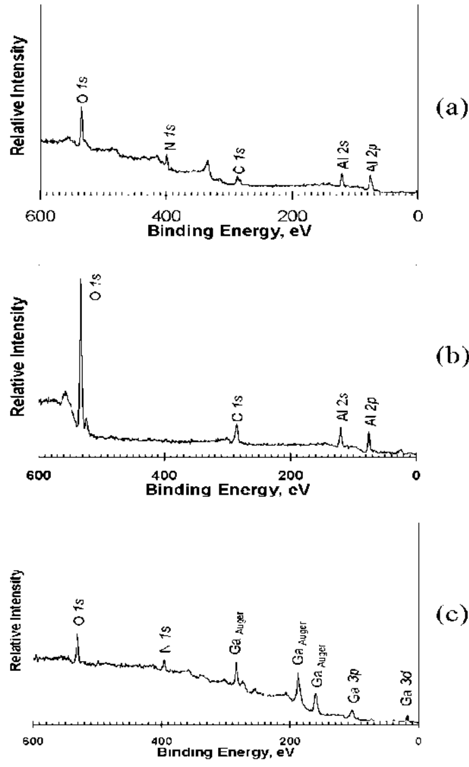

Figure 38: XPS survey scans of: (a) AlN as-capped GaN sample, (b) AlN capped sample after 1400 °C/5 s annealing, and (c) after removal of the AlN cap at the conclusion of annealing.

4.2.3 Structural characterization of microwave annealed samples

AFM images of the GaN sample surface, after microwave annealing at different temperatures with a MgO cap in place are shown in Fig. 39. It can be seen from Fig. 39 that the MgO cap was able to protect the GaN surface without any substantial decomposition at annealing temperatures up to 1300 ºC, but significant GaN

decomposition could be detected for the MgO capped annealing done at 1400 ºC (Fig. 39(e)). The GaN film totally decomposed, when the microwave annealing temperature was above 1400 ºC accompanied by cracking of the MgO cap, and liquid Ga droplets could be observed (not shown) on the surface.

AFM images of the GaN sample surface after microwave annealing at 1300 ºC and 1500 ºC with an AlN cap in place are shown in Fig. 39(d) and 39(f), respectively. It can be seen from Fig. 39(f) that the GaN surface of even the 1500 ºC/5 s microwave annealed sample appears very smooth with a RMS roughness (0.6 nm) comparable to the as-grown sample (0.3 nm). No evidence of any GaN decomposition can be seen for even this ultra-high-temperature annealing. For comparison, the AFM image of a GaN sample annealed for 5 s at 1300 ºC without any cap in place is shown in Fig. 39(b). Significant GaN decomposition resulting in the formation of hexagonal cavities can be observed in Fig. 39(b).

To summarize, ultra-fast microwave annealing was successfully used to anneal GaN epi-layers up to temperatures as high as 1500 ºC using a protective PLD AlN capping layer. The PLD deposited AlN film is a much better capping layer to preserve the surface integrity of GaN at temperatures > 1300 ºC compared to the e-beam deposited MgO film. It might seem that the MgO film might have cracked due to a greater lattice mismatch [84] between the GaN and MgO (~ 6.5%) [85] compared to the GaN and AlN (2.6%) [86]. However, x-ray diffraction scans (not shown) confirmed that the e-beam deposited MgO layer is fine-grain polycrystalline.

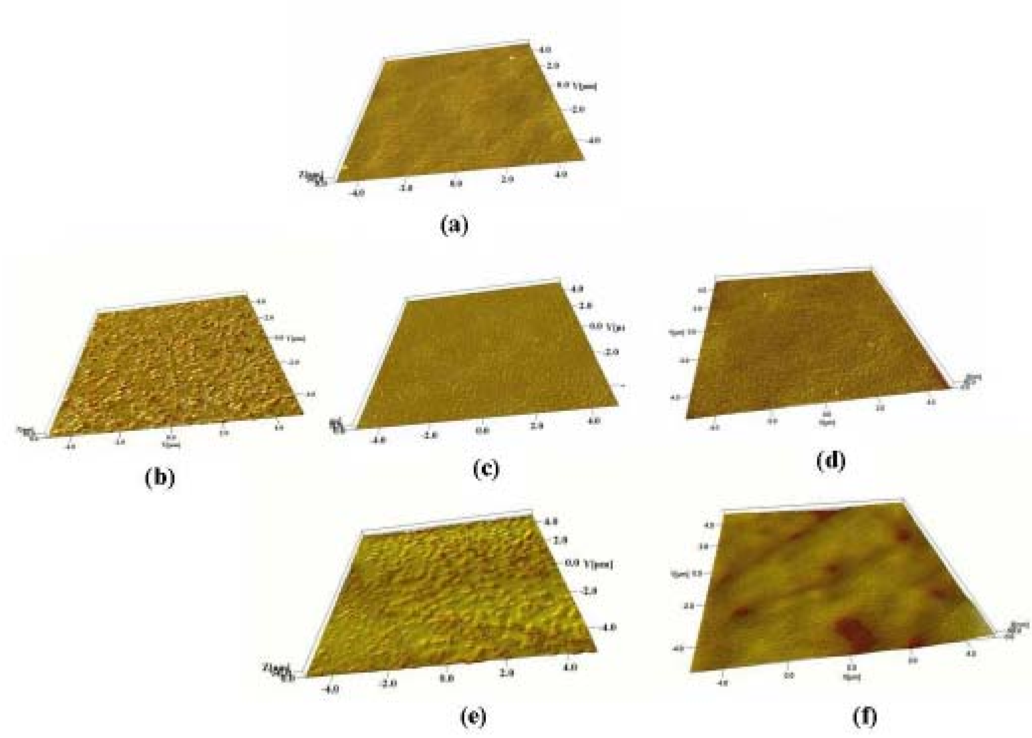

Figure 39: Tapping mode AFM images of: (a) an as-grown GaN surface (RMS roughness = 0.3 nm); after 1300 ºC / 5 s microwave annealing of GaN layers with (b) no cap (RMS roughness = 9.2 nm), (c) MgO cap (RMS roughness = 0.8 nm), and (d) AlN cap (RMS roughness = 1 nm); (e) after 1400 ºC / 5 annealing with MgO cap (RMS roughness = 7.2 nm); and (f) after 1500 ºC/5 s annealing with AlN cap (RMS roughness = 0.6 nm).

Thus, the MgO layer should have plenty of grain boundaries to accommodate lattice or thermal co-efficient of expansion (TCE) mismatch without cracking. In fact, significant GaN decomposition was observed for the MgO capped sample annealed at 1350 ºC, 50 ºC before the MgO film cracked, whereas the AlN capped samples remained

decomposition-free even after a 1500 ºC annealing treatment. It is known that the PLD process used to deposit the AlN cap results in a much better interface with the underlying GaN compared to the e-beam deposition process, which was used for the MgO cap formation. Thus, the presence of a large number of voids at the MgO /GaN interface could have allowed the escape of nitrogen from the GaN film, which accelerated the decomposition of the GaN film.

In addition to the MgO and AlN caps, photoresist converted graphite caps were also explored to study their feasibility for protecting the GaN surface during high-temperature microwave annealing. Graphite caps have successfully protected SiC epilayers during ultra-high temperature (1700 - 1900 ºC) microwave annealing of SiC [78]. However, in the present study it was found that for microwave annealing of GaN, the graphite caps started delaminating from the GaN surface at temperatures > 1000 ºC, presumably because of the stress at the GaN/graphite interface, created by localized decomposition of the GaN epilayer under the graphite cap. From this study, it is evident that an excellent interface between the GaN and the capping layer is vital, if the GaN surface morphology is to be preserved during high-temperature annealing.

4.2.4 Optical Characterization

Low-temperature (5 K) PL spectra on the Mg-doped GaN films grown on sapphire annealed at 1300 ºC and 1500 ºC for a duration of 5 s, using AlN cap layer, are shown in Fig. 40. The PL spectrum from an as-grown (unannealed) sample is also shown in Fig. 40 for comparison. The only feature visible in the PL spectra from the as-grown

sample is a broad band (3.0 -3.2 eV), with no phonon replicas. This band has been reported in case of heavily Mg-doped GaN grown by MOCVD [86]. The UVL band is assumed to originate from recombination between a shallow donor and the Mg acceptor(donor-acceptor pair, DAP) [84,86]. These broad and featureless UVL band observed in the PL spectrum of as-grown sample has been assigned to potential fluctuations arising from the random distribution of charged impurities such as donors and acceptors, coupled with the fact that there are not enough free carriers to screen them [86]. For the sample annealed at 1300 ºC, the relative intensity of the UVL band increases and a significant red shift is observed. In addition, a second band with similar intensity at 3.27 eV (zero-phonon line, ZPL) along with its LO phonon replicas is detected. Also observed, is a near band-edge emission peak at 3.47 eV [86] corresponding to the recombination of an exciton bound to a neutral donor (NBE). These observations are consistent with activation Mg acceptors in the annealed samples. For the sample annealed at 1500 ºC, the relative intensity of the UVL band and the near-band-edge (NBE) emission band increase. This indicates that the 1500 ºC / 5 s microwave annealing is more effective than the 1300 ºC / 5 s annealing in reducing the concentration of the deep compensating centers or passivating hydrogen, therefore, in activating the Mg dopant.

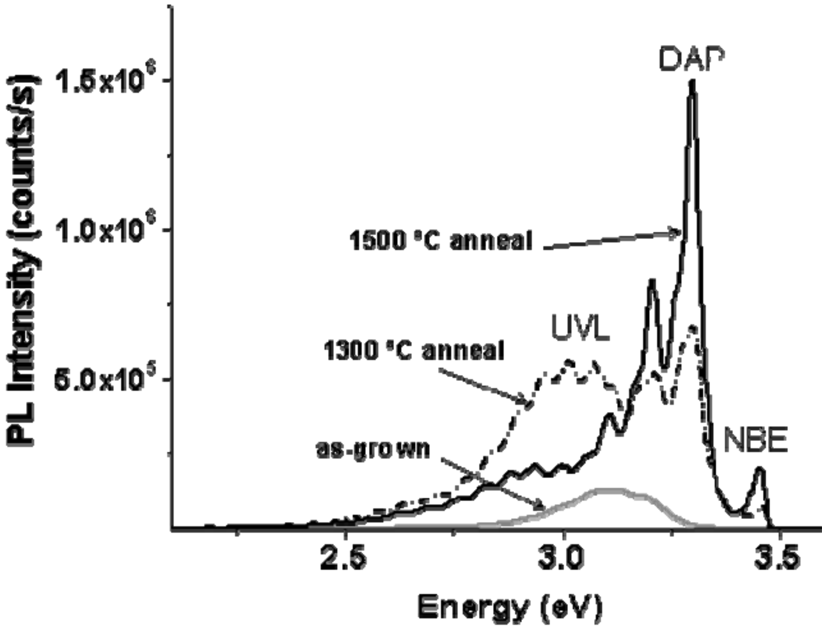

Figure 40: Low-temperature (5 K) PL spectra of as-grown Mg:GaN on sapphire; and of AlN capped samples subjected to 5 s microwave annealing at 1300 ºC and 1500 ºC.

Low-temperature PL spectra (shown in Fig. 41), on the microwave annealed samples with a MgO cap in place, indicate an increase in Mg activation for the 1300 ºC / 5 s annealed sample based on the observation of an intense, structured UVL band at 3.29 eV (ZPL) as well as a strong near-band-edge emission (NBE) band at 3.46 eV. However, upon increasing the annealing temperature to 1350 ºC, the NBE band disappears, whereas a broad blue band (2.7 – 3.1 eV) becomes dominant. This band is red shifted when compared to the band between 3.0 and 3.2 eV band of the as-grown sample.

Since the AFM images did show any significant decomposition of GaN for the 1350 ºC annealing, it is conceivable that this broad band originates from the recombination involving deep donor-like defects, which are activated by the annealing treatment. A similar spectrum (not shown) was also obtained for the 1400 ^{0}C / 5 s annealed sample, with the MgO cap in place.

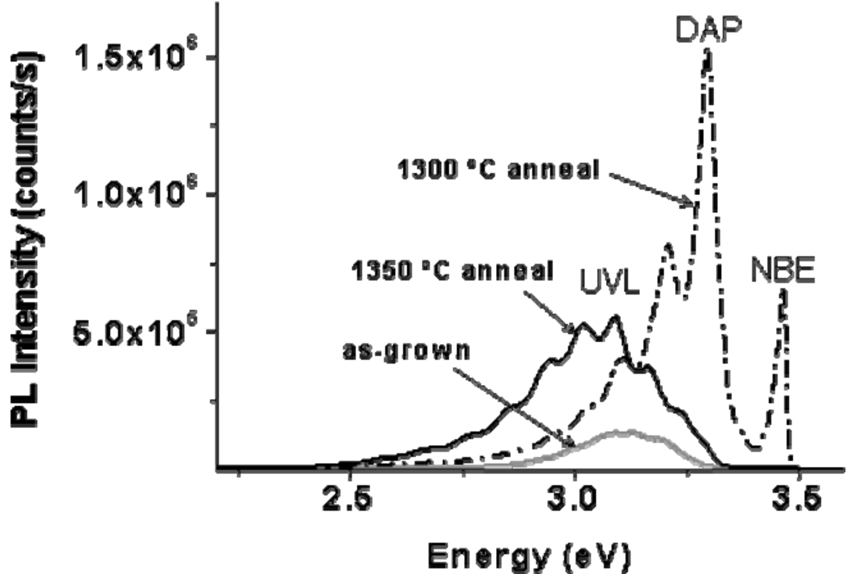

Figure 41: Low-temperature (5 K) PL spectra of as-grown Mg:GaN on sapphire; and of MgO capped Mg-doped GaN samples after 5 s microwave annealing at 1300 ºC and 1350 ºC.

The above PL results suggest that the high-temperature (1500 ºC) microwave annealing of AlN caped samples is very effective in increasing the net acceptor concentration in in-situ Mg doped.

4.2.5 Electrical Characterization

A variation of the hole concentration (*p*) as a function of microwave annealing temperature, for the uncapped samples and for samples protected by the MgO and AlN caps during 5 s microwave annealing, is shown in Fig. 42. For both uncapped as well as MgO capped samples, the *p* decreases, when the annealing temperature is increased above 1300 ºC. This is a direct consequence of increasing GaN decomposition with increasing annealing temperature for uncapped and MgO capped GaN layers, which was observed from the AFM images. The PL spectra for the MgO capped samples also indicated a decrease in Mg acceptor activation for the 1350 ºC and 1400 ºC anneals compared to the 1300 ºC annealing, which agrees with the electrical results.

However, for the samples, which were capped by the AlN during annealing, the highest *p* is measured for the 1500 ºC annealing. Based on the above PL results, it is believed that this is due to a decrease in the compensating deep donor on passivating hydrogen concentration with increasing annealing temperature as long as the integrity of the GaN material is maintained. Hole mobilities of 14 – 19 cm^2/ V.s were measured on all the above-mentioned samples.

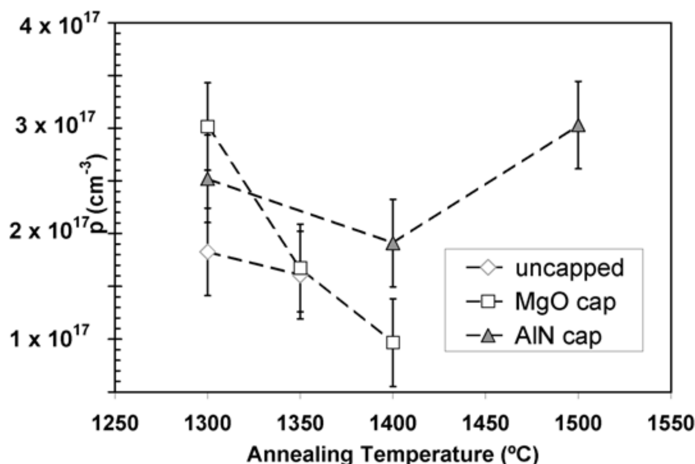

Figure 42: Hole concentration (*p*) as a function of annealing temperature for 5 s duration microwave annealing on uncapped, MgO capped, and AlN capped in-situ Mg-doped MOCVD-GaN.

4.2.6 Summary

Due to the ultra-fast heating/cooling rates of the microwave RTA system, it is possible to successfully anneal GaN in the temperature range of 1300 – 1500 ºC, when the GaN is protected by a pulsed laser deposited AlN cap. The surface of the AlN capped GaN layer annealed at 1500 ºC for 5 s is very smooth with a RMS roughness of 0.6 nm, which is comparable to the RMS roughness of 0.3 nm measured on the as-grown sample. The e-beam deposited MgO cap successfully protected the GaN surface during microwave annealing only up to 1300 ºC, but a significant GaN decomposition is

observed for the higher temperature anneals. Low-temperature (5 K) PL spectra and Hall measurements performed on the AlN capped samples indicate that the 1500 ºC / 5 s microwave annealing is more effective than the 1300 ºC / 5 s microwave annealing in activating the Mg-dopant. By comparison, fairly good luminescence and electrical results were obtained for the MgO capped GaN layers only for annealing up to 1300 ºC, but the optical as well as electrical quality of the GaN layers degrade during higher-temperature (> 1300 ºC) annealing. Photoresist converted graphite cap delaminates from the GaN surface for microwave annealing temperatures > 1000 ºC and is therefore not a suitable capping material for high-temperature annealing of GaN.

4.3 Microwave annealing of *in-situ* Be doped GaN films grown by MBE

Many groups have been investigating beryllium as a *p*-type dopant in GaN using a variety of approaches. There have been limitations and difficulties to reproduce reports of *p*-type conductivity for Be doped GaN by annealing. The activation energy of Be in *p*-type GaN has been reported in the range 120-200 meV [88,89]. To the best of the author's knowledge, direct comparison between the photoluminescence (PL) measurements and secondary ion mass spectroscopy (SIMS) has not been reported to date on in-situ Be-doped GaN.

4.3.1 Experimental details

In this study, 1μm thick, Be-doped GaN epilayers, grown by molecular beam epitaxy (MBE) on *n*-type 6H-SiC substrate with a Be doping concentration of ~ 1 x 10^{19} cm^{-3} have been used. The GaN wafer is capped with ~ 0.3μm layer of AlN to protect the sample during annealing. The AlN layers were deposited using pulsed-laser deposition [82]. For performing the microwave annealing on the GaN sample, a 5mm x 5mm highly conducting 4H-SiC piece is placed directly underneath the GaN sample to serve as a susceptor. The samples were placed within the microwave heating head and the temperature is measured using the optical pyrometer [78]. Microwave annealing is performed in a temperature range of 1300-1500 ^{0}C for a duration of 5s in pure (99.9%) nitrogen atmosphere. After annealing, the AlN cap is removed by a 1 hour etch in 85 % (wt) H_3PO_4 at 120 ^{0}C.

4.3.2 X-Ray Photoelectron Spectroscopy

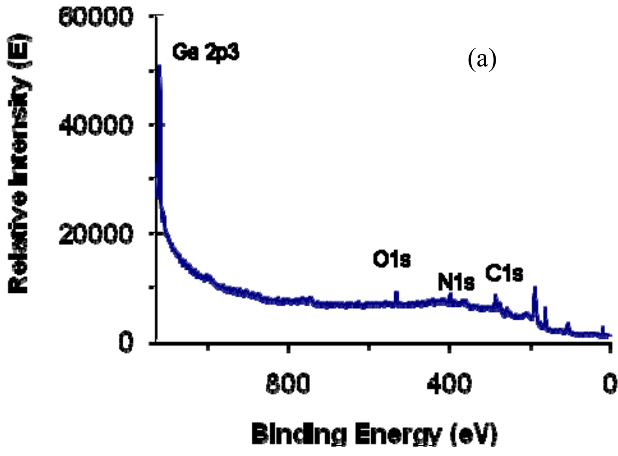

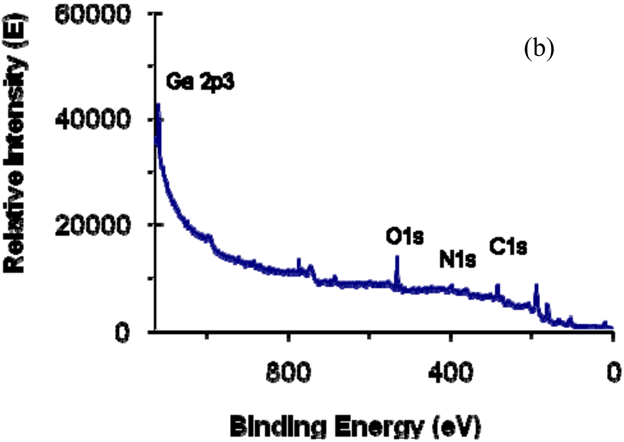

Figure 43: XPS of Be in-situ doped GaN films after the removal of AlN cap (a) unannealed, and (b) annealed at 1400 ^{0}C / 5 s.

The removal of the AlN cap on the GaN surface was monitored by using x-ray photoelectron spectroscopy (XPS). The XPS spectra were obtained using a Mg Kα x-ray source.The XPS scans for the unannealed sample and 1400 ^{0}C/5s annealed sample are shown in Fig. 43(a), and 43(b). One can clearly see the Ga and N signals in the annealed sample, but no Al signal, indicating the effective removal of cap.

4.3.3 Secondary ion mass spectrometry

The Be SIMS depth profiles in unannealed and annealed samples are shown in Fig. 44. A uniform (~ 1 x 10^{19} cm^{-3}) concentration of Be in GaN film can be clearly seen in Fig. 44(a). After 1300 ^{0}C/5s annealing, the Be out-diffused into the AlN layer and also in-diffused toward the GaN/SiC interface. The in- and out- diffusion of the Be increased with increasing annealing temperature as depicted in Fig. 44 (a), (b), (c), and (d).

In fact, after 1500 ^{0}C annealing only a small fraction of in-situ doped Be remained in GaN layer, revealing the unattractive nature of Be-doping for the GaN technology. The Be is a known fast interstitial diffuser in III – V compunds [88]. Hence, it does not seem to be a suitable choice for GaN, especailly if the material needs to be subjected to a high temperature treatment after the epilayer growth.

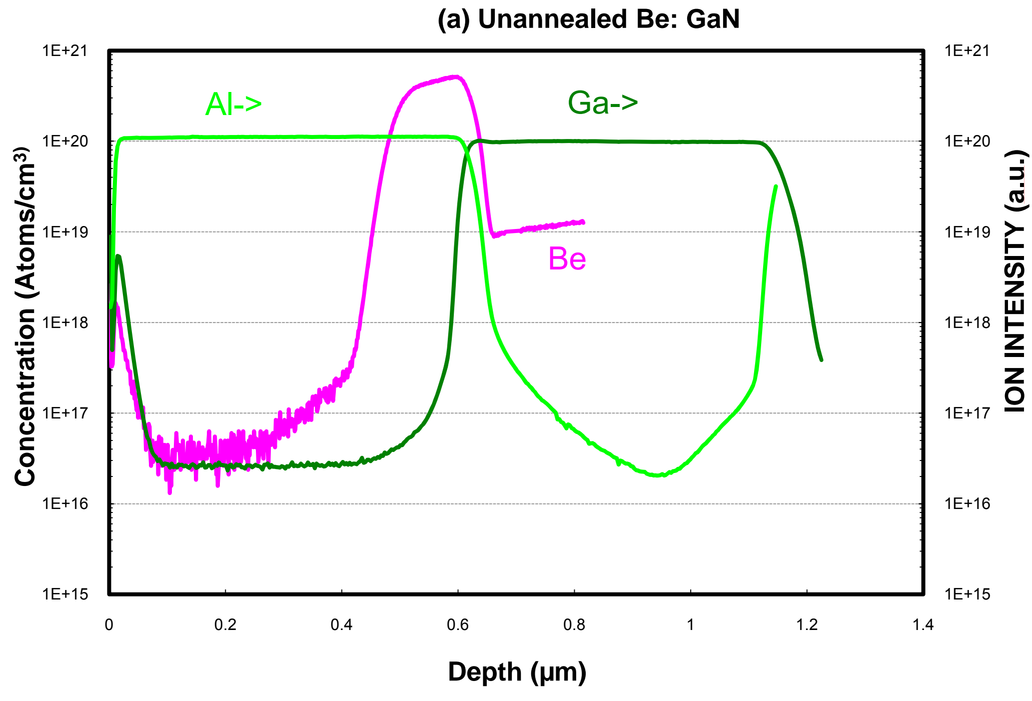
(a) Unannealed Be: GaN
Al->
Ga->
Be
Concentration (Atoms/cm3)
ION INTENSITY (a.u.)
Depth (µm)
1E+21
1E+20
1E+19
1E+18
1E+17
1E+16
1E+15
0
0.2
0.4
0.6
0.8
1
1.2
1.4

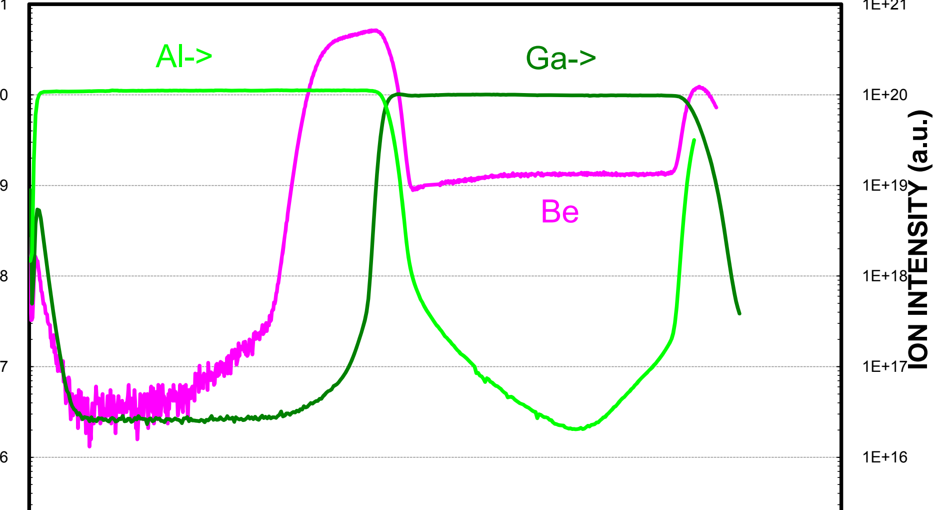
(b) Annealed at 1300 0C/5s
Al->
Ga->
Be
Concentration (Atoms/cm3)
ION INTENSITY (a.u.)
Depth (µm)
1E+21
1E+20
1E+19
1E+18
1E+17
1E+16
1E+15
0
0.2
0.4
0.6
0.8
1
1.2
1.4

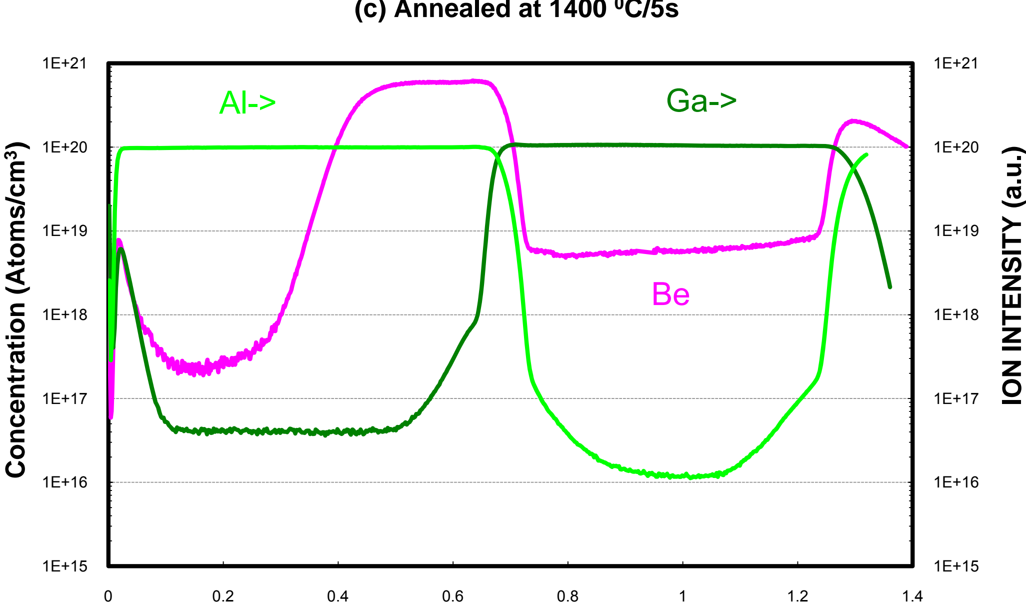

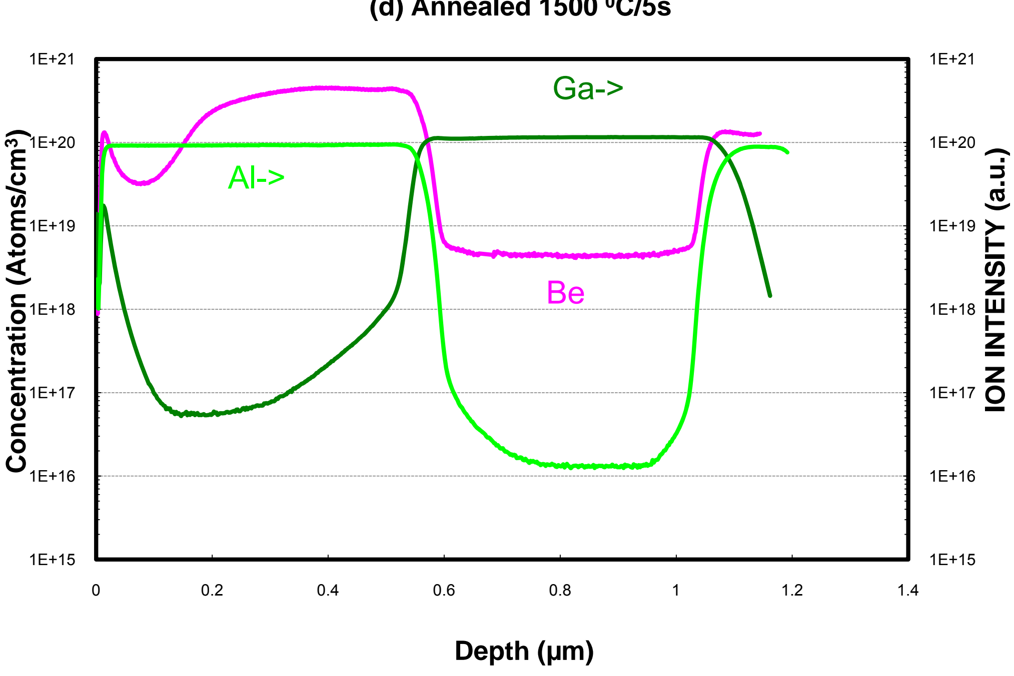

Figure 44: SIMS results of the Be doped GaN films (a) before annealing, and after (b) 1300 ºC / 5 s, (c) 1400 ºC / 5 s, and (d) 1500 ºC / 5 s microwave annealing.

4.3.4 Optical Characterization

Low-temperature PL spectra from Be doped GaN, microwave annealed at 1300 ºC / 5 s, 1400 ºC / 5 s, 1500 ºC / 5 s and 1600 ºC / 5 s, are shown in Fig. 45. For reference, the PL spectrum from unannealed as-grown GaN epilayer is also shown in Fig. 45. The PL spectra of the Be-doped GaN films microwave annealed at 1300 ºC / 5s, 1400 ºC / 5s, 1500 ºC / 5s and 1600 ºC / 5 s shows the near-bandedge (NBE) and its phonon replica at 3.464 eV and 3.369 eV, respectively. Also observed is the intense and broad luminescence band related to recombination processes involving SA-SD pairs (DAP) with ZPL at 3.273 eV. Similar spectra have been observed on unintentionally doped bulk and epitaxial films of GaN [45]. The peak position of this DAP band is about 11 meV red-shifted from the value reported for intentionally Be-doped GaN films grown by MBE [90]. The peak position of DAP band depends on the concentration of donors and acceptors, and the excitation conditions. Experiments performed under high excitation conditions results on peak shift to higher energies, due to the saturation of process involving SA-SD (DAP) pair at larger lattice separation. The large energy difference in peak position of the DAP band of the annealed samples and reported data [45] strongly indicates that the acceptor involved in the recombination processes of these annealed samples is not related to Be acceptor impurities. The nature of the DAP band with ZPL at 3.273 eV are still under discussion. The large variation of the DAP relative intensity may results from effects associated with the high temperature annealing process.

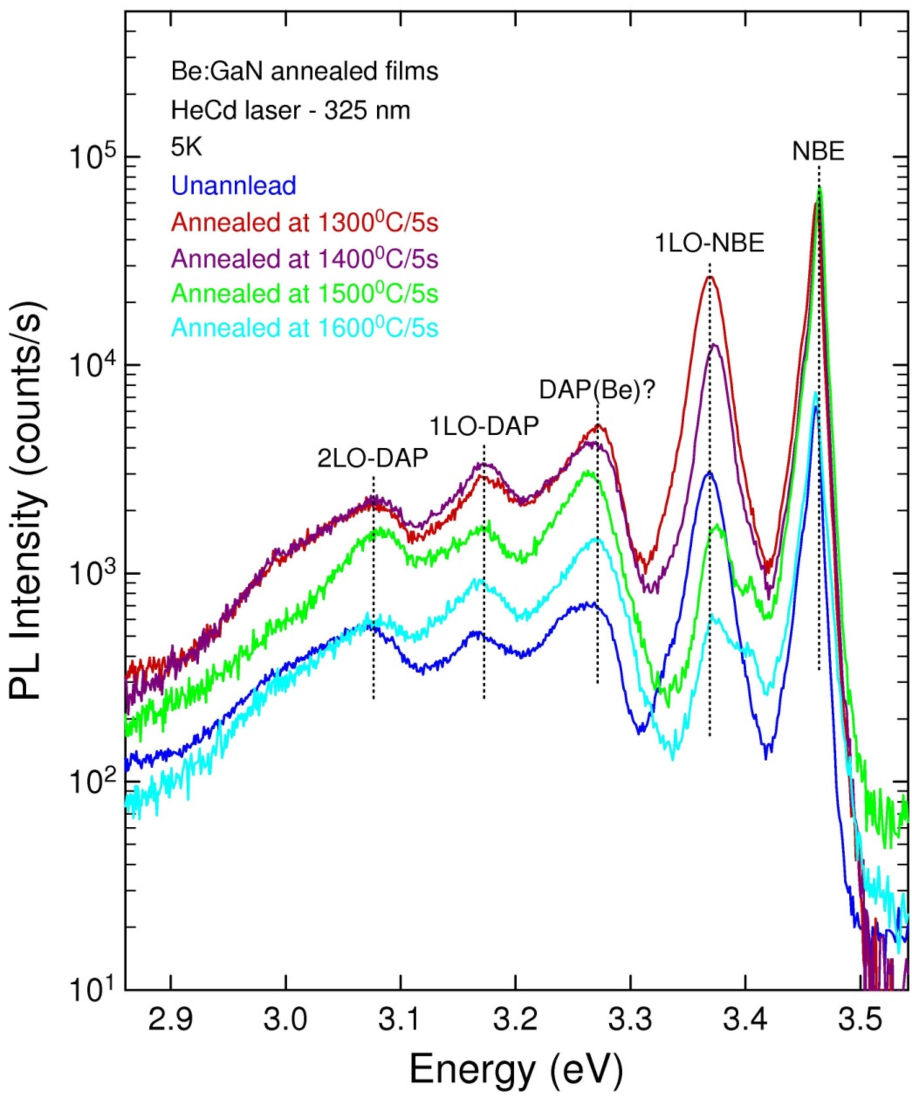

Figure 45: Low-temperature (5 K) PL spectra from an un-implanted GaN epilayer, and GaN epilayers before and after 1300 ºC / 5 s ,1400 ºC / 5 s, 1500 ºC / 5 s and 1600 ºC / 5 s microwave annealing.

4.3.5 Summary

In summary, Be doped GaN epilayer films annealed at high-temperatures in the range of 1300 -1600 ºC/ 5s using ultrafast microwave heating did not show any evidence of Be activation as a shallow acceptor in GaN. In addition, a severe intense and broad luminescence band related to recombination processes involving SA-SD pairs (DAP) with ZPL at 3.273 eV. The large energy difference in peak position of the DAP band of the annealed samples and reported data [45] strongly indicates that the acceptor involved in the recombination processes of these annealed samples is not related to Be acceptor impurities. The large variation of the DAP relative intensity may results from effects associated with the high temperature annealing process.

4.4 Microwave annealing of Mg-implanted GaN films grown on sapphire

Selective area Mg-implants using implantation mask could be used to create arrays of GaN LEDs and laser diodes as opposed to selective area reactive ion etching of *p*-type GaN epilayer, which compromises planarity and consequently device yield. High-dose Mg-implantation is also useful to form low-resistance ohmic contact to *p*-type GaN layers.

4.4.1 Experimental details

The multiple energy Mg^+ implant schedule performed into undoped 3 μm thick GaN epilayers grown on a-plane sapphire is given in Table IV. Also single energy Mg-implant at 150 KeV for a dose of 5x 10^{14} cm^{-2} was performed. The implantation was performed at a temperature of 500 ºC with a tilt of 7 º. The multiple energy Mg implant schedule for GaN was designed using the SRIM software to obtain a uniform implant concentration box depth profile.

After implantation, the GaN epilayers were capped by a 0.3 μm layer of AlN grown by PLD and then subjected to microwave annealing in the range of 1300 – 1500 ºC for 5 - 15s. After annealing, the AlN cap was etched by the H_3PO_4 recipe, as described earlier. The reliable removal of the AlN caps after microwave annealing was again confirmed by the XPS measurements. After removing the cap, the Mg – implanted GaN epilayers were characterized for their structural and optical properties, and also for the thermal stability of the implant.

Table IV: Multiple energy Mg implant schedule performed on undoped GaN.

Implant Energy (keV)	Implant Dose (cm^{-2})
10	3.8×10^{13}
25	3.3×10^{14}
55	1.7×10^{14}
110	4.1×10^{14}
225	8.3×10^{14}
300	8.3×10^{14}

4.4.2 X-Ray Photoelectron Spectroscopy

XPS scans of single energy Mg implanted GaN samples after the removal of AlN cap are shown in Fig. 46. From the XPS scans of Mg: GaN samples shown in Fig. 46(a), and 46(b) the Ga and N signals are observed, but no Al signals are observed, indicating that the oxidized AlN cap was successfully removed.

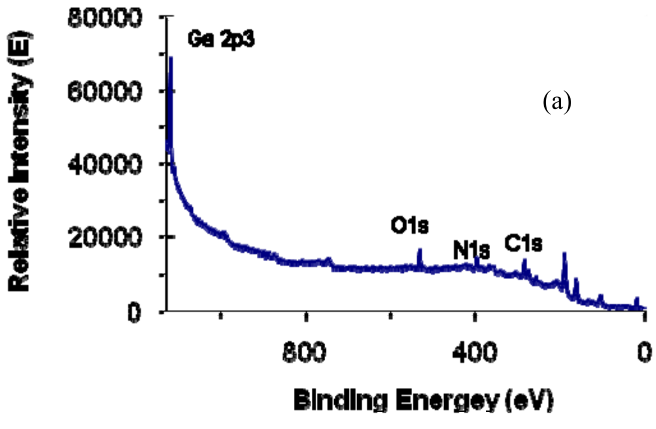

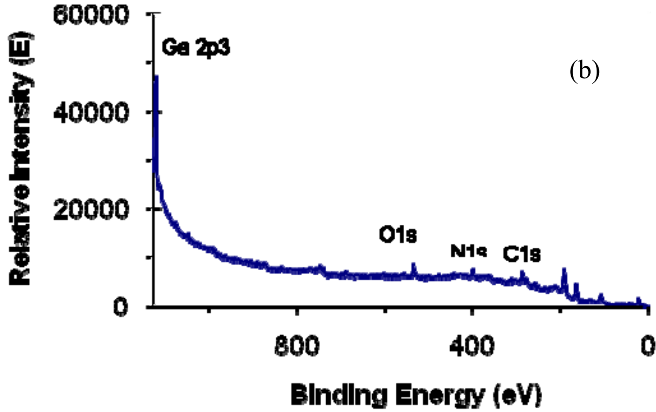

Figure 46: XPS survey scans of: (a) Mg: GaN sample annealed at 1400 ºC/15s , and (b) Mg:GaN sample annealed at 1500 ºC/15s.

4.4.3 Secondary ion mass spectrometry

SIMS depth profiles of the Mg implanted GaN before and after 1300 ºC /5 s and 1400 ºC / 5 s microwave annealing are shown in Fig. 47. The SIMS profile for the as-implanted sample and for the 1300 ºC / 5 s annealed sample are close. However, a slight Mg accumulation at the surface and some in-diffusion of Mg into the GaN can be

observed for the 1300 ºC annealed sample. The microwave annealing at 1400 ºC resulted in a significant Mg accumulation in a thin ≈ 40 nm surface layer, and a depletion of Mg at depths of 40 nm – 400 nm from the surface. A pronounced in-diffusion of Mg into the GaN can also be observed from Fig. 47 at depths beyond 400 nm. As indicated in Fig. 47, the extracted doses from the 1300 ºC (1.6×10^{15} cm^{-2}) and 1400 ºC (1.5×10^{15} cm^{-2}) annealed samples are slightly lower compared to the extracted dose (1.7×10^{15} cm^{-2}) from the as-implanted sample. This is probably due to some out-diffusion of Mg into the AlN cap during the annealing treatment.

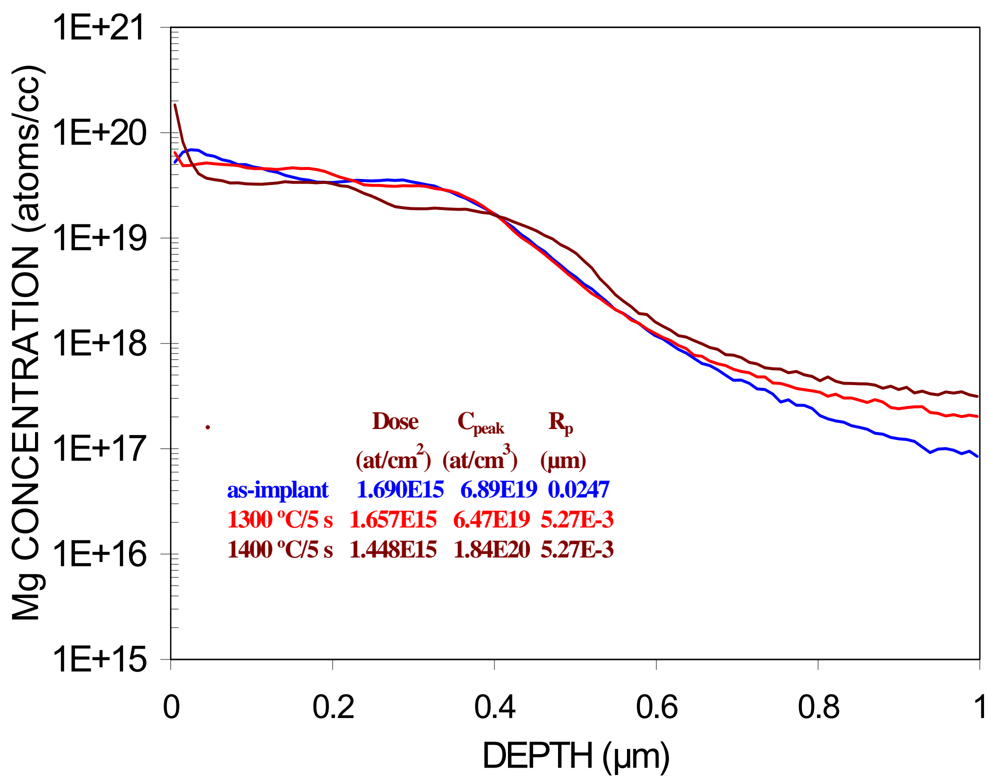

Figure 47: SIMS depth profiles of the Mg implanted GaN before and after 1300 ºC /5 s and 1400 ºC / 5 s microwave annealing.

4.4.4 Atomic Force Microscopy

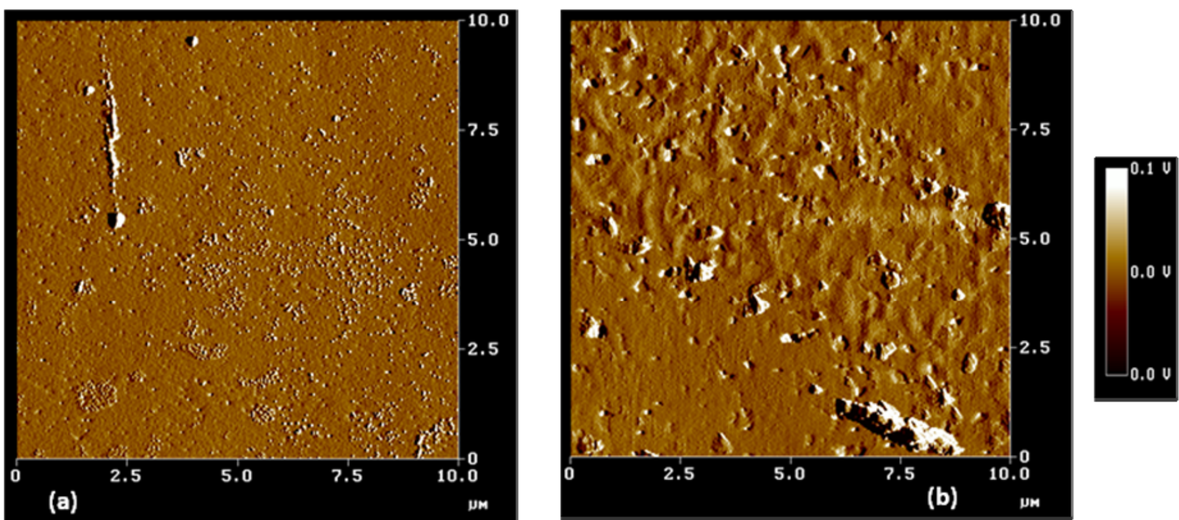

Figure 48: Tapping mode AFM images Mg:GaN of: (a) after 1300 ^{0}C/15s annealing (RMS roughness = 3.387 nm), and (b) after 1500 ^{0}C/15s annealing (RMS roughness = 9.724 nm).

AFM images of the GaN sample surface, after microwave annealing at 1300 ^{0}C/15 s and 1500 ^{0}C/15 s (after the AlN cap has been removed) are shown in Fig. 48(a) and Fig. 48(b), respectively. It can be seen from Fig. 48(a) that the GaN surface of 1300 ^{0}C/15 s microwave annealed samples appear smooth with the RMS roughness of 3.387 nm. Also the surface of 1500 ^{0}C/15 s microwave annealed sample showed a smooth surface with a RMS roughness of 9.724 nm as shown in Fig. 48(b). Though there is an increase in the roughness with an increasing annealing temperature, the measured

roughness of ~ 10 nm for the 1500 ^{0}C/15s annealing is not severe enough for the device applications compared to 1300 ^{0}C/15s annealed sample.

4.4.5 X-Ray Diffraction and rocking curve measurements

HRXRD and rocking curve measurements were taken on an 18 kW Rigaku ATX-E diffractometer with Cu radiation. Two channel cut Ge (220) crystals were used to monochromatize the incident beam and provide very parallel CuKa1 radiation. This arrangement almost eliminates the vertical divergence in the incident beam to give a precise measurement of the rocking curve and lattice parameters. In addition, this diffractometer has an open Eulerian cradle with independent (x,y,z) movements as well as the tilt, χ and rotation, ϕ movements in order to align the sample to obtain the precise measurements.

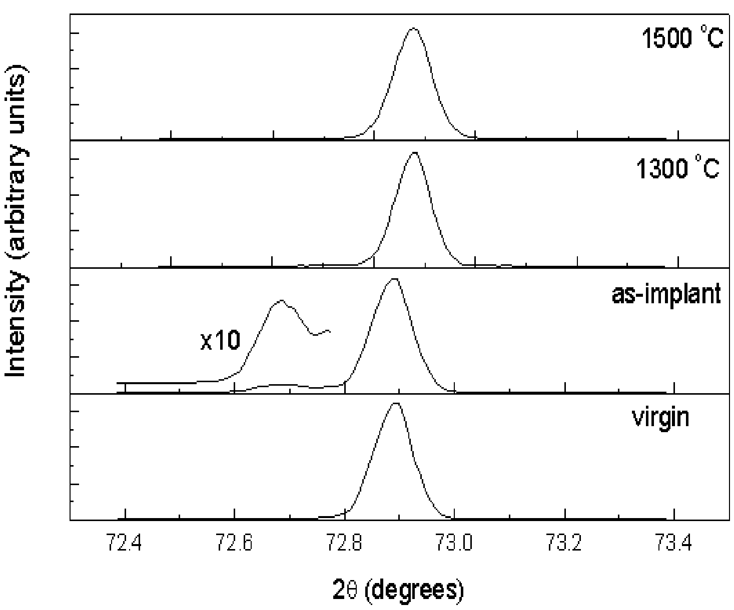

Figure 49: XRD scans of the GaN (004) as-implanted and microwave annealed films.

Fig. 49 and Fig. 50 show an overlay of the XRD scans on single energy Mg-implanted GaN (004) and GaN (104) reflections of the as-grown, as-implanted as well as the microwave annealed films. It can be seen that the implanted film has the defect sub-lattice peaks (10x magnification) due to the interference of the x-rays from the implanted impurity in the interstitial sites. These sub-lattice peaks disappear after microwave annealing and confirm that the implanted Mg atoms have taken substitutional positions.

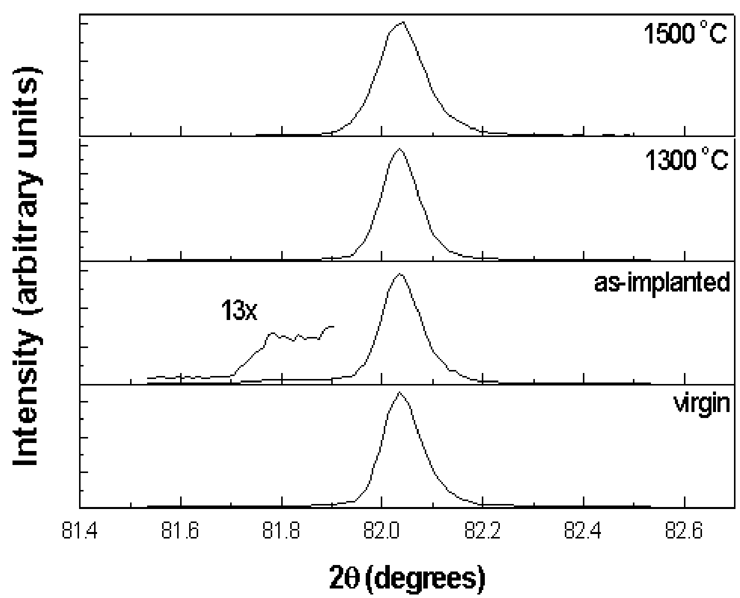

Figure 50: XRD scans of the GaN (104) as-implanted and microwave annealed films.

4.4.6 Optical Characterization

Low-temperature PL spectra from multiple energy Mg-implanted GaN, before and after 1400 ºC / 5 s and 1500 ºC / 5 s microwave annealing are shown in Fig. 51. For reference, the PL spectra from an as-grown GaN epilayer used for the Mg- implantation is also shown in Fig. 51. In addition to the near-band edge emission, a broad yellow

luminescence (YL) band (2.0 eV – 2.6 eV) and a near-ultra violet luminescence (N-UVL) band (2.7 eV – 3.2 eV) also can be observed in the PL spectra obtained from the as-grown GaN epilayer. The YL in GaN is generally attributed to the presence of C, O, and/or H in the material [45]. The presence of YL and N-UVL in the PL spectra indicates the presence of deep levels in UID as-grown GaN films.

The as-implanted GaN does not exhibit any significant photoluminescence, since the implant-induced damage introduces a lot of defect levels in the bandgap, which act as non-radiative recombination centers. The PL spectra from the 1400 ºC microwave annealed GaN does show the re-appearance of the near band-edge (NBE) emission as well as DAP emission related to Mg activation. Thus, microwave annealing at 1400 ºC at-least partially heals the implant-induced lattice damage. Increasing the annealing temperature to 1500 ºC results in further reduction of implant-induced damage as can be seen from the increase in intensity of both NBE emission and Mg activation related DAP emission bands of Fig. 51. However, the defect related YL and BL bands can also be seen in the PL spectra of microwave annealed samples at a higher intensity than the NBE peak, which possibly precludes any electrical activation due to compensation of the acceptors. It seems, it is difficult to remove the residual implant damage in multiple energy Mg-implanted GaN. In addition, it is paramount to have an excellent quality starting GaN epilayer, which does not emit high intensity YL and N-UVL bands, which has been associated with deep level defects.

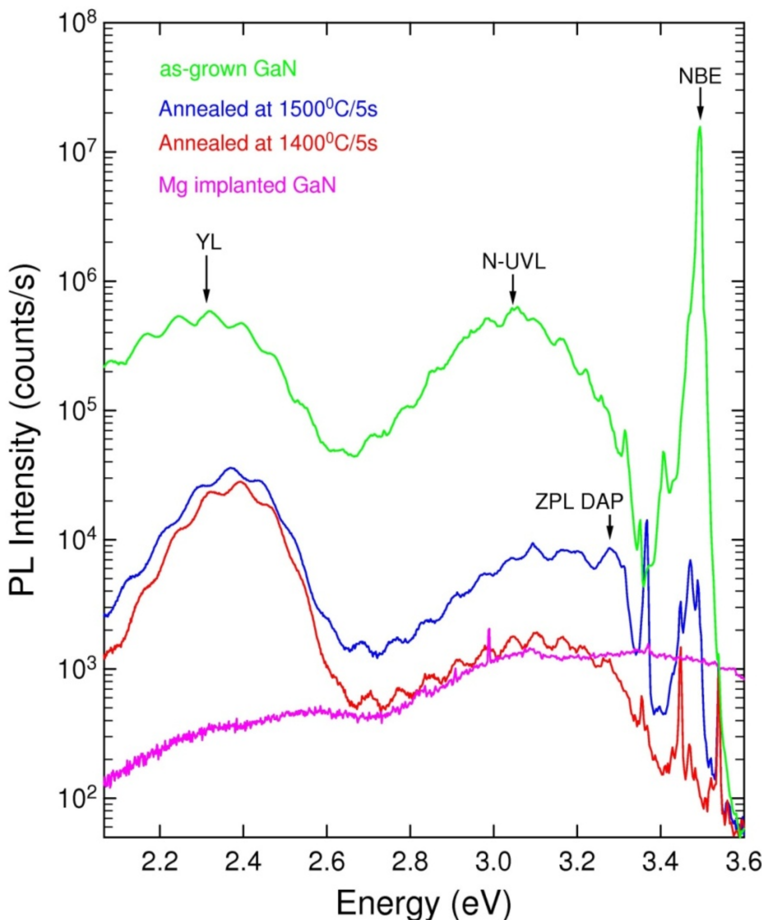

Figure 51: Low-temperature (5 K) PL spectra from an un-implanted GaN epilayer, and multiple energy Mg implanted GaN epilayers before and after 1400 ºC / 5 s and 1500 ºC / 5 s microwave annealing.

Similarly, Low-temperature PL spectra (shown in Fig. 52), on the microwave annealed single energy Mg-implanted GaN epilayer grown on sapphire films, indicates an increase in Mg activation for the 1300 ºC / 15 s annealed film by the presence of an intense UVL band at 3.29 eV (ZPL) as well as a relatively stronger near-band-edge emission (NBE) band at 3.46 eV with its phonon replica (1LO-NBE) at 3.37 eV. Upon

increasing the annealing temperature to 1400 ºC/15s and 1500 ºC/15s, the intensity of NBE band decreases with an increase in the intensity of broad N-UVL band (2.7 – 3.1 eV). A broad yellow luminescence is also observed (2.0 –2.4 eV) in the spectra of the annealed sample. Note that these bands are observed in UID as grown GaN films. An increase in the intensity and structure of the DAP band is with increasing temperature is also observed. This confirms the increase in the concentration of Mg acceptors at higher annealing temperature.

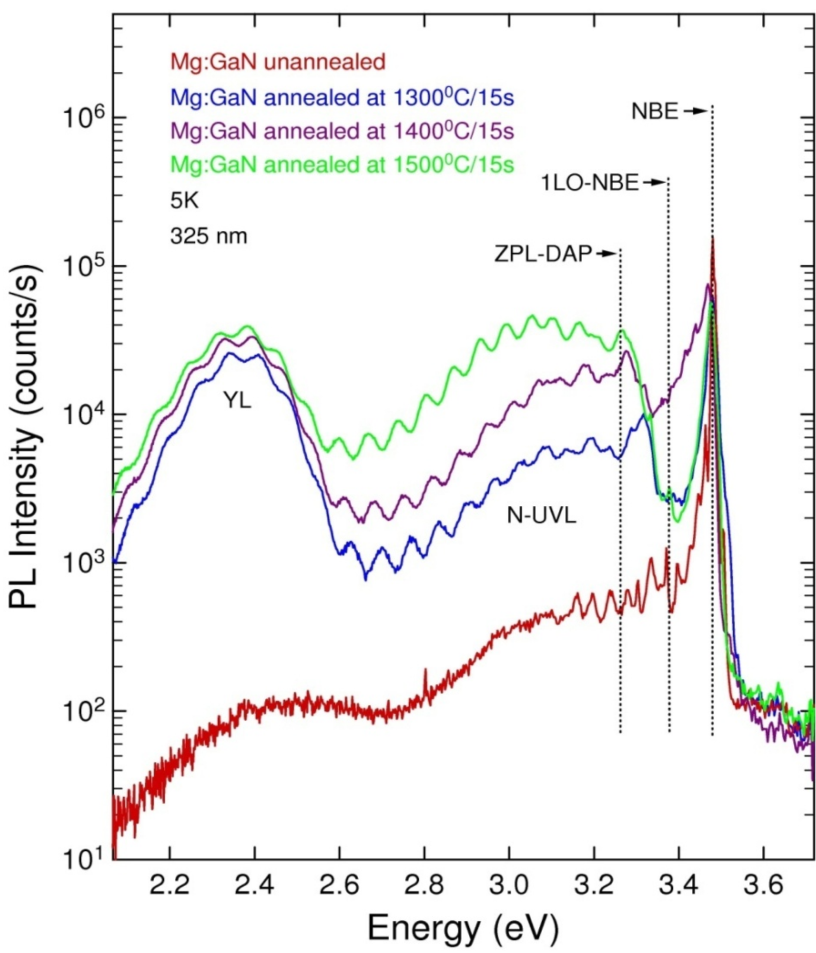

Figure 52: Low-temperature (5 K) PL spectra of as-implanted (unannealed) and annealed Mg-implanted GaN for 15s annealing at 1300 ^{0}C, 1400 ^{0}C, and 1500 ^{0}C.

4.4.7 Electrical Characterization

The electrical characterization of the multiple energy Mg implanted GaN, even after a 1500 ºC annealing treatment, has indicated almost no electrical activation of Mg acceptor. The samples are highly resistive. This is likely due to the significant lattice damage created by the high dose, multiple energy Mg implants. Also, the PL

spectra (Fig. 51) have indicated the presence of deep levels even in the as-grown GaN epilayer, which may influence the Mg activation. The combination of the poor starting material and high residual implant damage are detrimental for the electrical activation of multiple energy Mg implant.

4.4.8 Summary

In summary, GaN epilayers were reliably annealed at high-temperatures in the range of 1300 -1500 ºC, when the GaN is protected by a PLD AlN cap. Promising electrical and optical results were obtained for in-situ Mg doped epilayers, and single-energy Mg-implanted GaN. However, it has proven to be more challenging to activate multiple energy, high dose Mg implants. Significant lattice damage exists even after annealing at temperatures as high as 1500 ºC, albeit for short 5 s durations.

5. NONDESTRUCTIVE CHARACTERIZATION OF DISLOCATIONS AND MICROPIPES IN 4H-SiC USING PHOTOLUMINESCENCE IMAGING

Silicon carbide (SiC) is an attractive material for developing high-power, high-temperature, and high-frequency devices, owing to its superior properties [91]. Devices made from SiC are facing various issues related to defects nucleated in the substrate or epitaxial layers [92,93]. Micropipes (MPs) have been known as device-killing defects, reducing the breakdown voltage significantly. Low angle grain boundaries (LAGBs), consisting normally of a mixture of basal plane dislocations (BPDs) [94] and threading edge dislocations (TEDs) [95], act as nucleation sites for basal stacking faults (SFs) in SiC bipolar devices [96]. Subsequent electron-hole recombination enhanced partial dislocation glide can expand the SFs over large areas leading to the degradation of device performance [97].

Several techniques can be utilized to identify defects present in SiC, for examples, transmission electron microscopy (TEM), molten potassium hydroxide (KOH) etching and synchrotron white beam X-ray topography (SWBXT). TEM is a destructive technique and suffers from small field of view. The information collected by molten KOH etching is extremely limited since etching occurs only at the sample surface. SWBXT has proven to be a powerful technique for recording the overall defect distribution in SiC crystals. Furthermore, the nature of defects can be readily obtained by

SWBXT, e.g., line direction and Burgers vector (direction and magnitude) of dislocations and misorientation of LAGBs. However, the technique evidently requires access to a synchrotron X-ray source. In this thesis work, a fast and a simple technique, employing photoluminescence (PL) imaging, to record the defect structures in commercial SiC wafers is explored and the results were compared to those obtained from SWBXT.

5.1 Experimental Details

SiC crystals used in the study are commercial 3-inch 4H-SiC wafers, grown by the physical vapor transport (PVT) technique, with 8° off-cut towards [11-20]. The luminescence emission was excited with the 325 nm line of a HeCd laser. A combination of UV-corrected lenses was employed to expand the laser beam to achieve the required uniform wafer illumination. A near UV-extended CCD with built-in wheel filters, fitted with a collecting lens, was employed to acquire the real color [combination of Red, Green and Blue (RGB)] and monochromatic colors (R, G, B) images. External filters with specific band-passes can also be conveniently used to map the spatial distribution of specific defects. The laser power density was controlled with calibrated neutral density filters. A number of UV laser lines can also be employed to provide depth profile. Grazing-incidence SWBXT images using the (11-2.12) plane reflections were recorded from the Si-face at an X-ray incident angle of 2°.

5.2 Results and Discussion

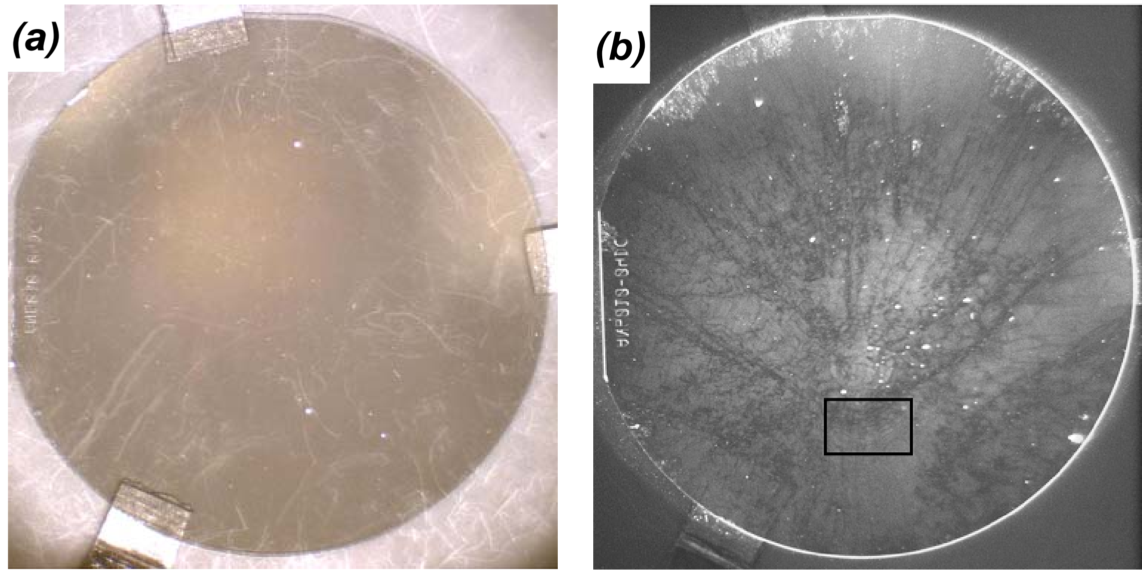

Figure 53: Comparison of the (a) photographic image of the 3-inch wafer and (b) PL panchromatic image. The overall distribution of defects is clearly seen in the panchromatic PL image.

Fig. 53(a) shows a photographic image recorded from a wafer in room light and Fig. 53(b) is the corresponding panchromatic PL image. The major flat of the wafer with the laser mark is (1-100) while the minor flat corresponds to (11-20). In the image recorded using room light, the whole wafer is uniformly illuminated and no clear features are revealed [the diffused white lines distributed in Fig. 53(a) are artifacts]. However, in the panchromatic PL image (Fig. 53(b)), a large number of dark lines and bright dots are observed. The PL emission results from the radiative recombination of photon excited carriers. The estimated penetration depth of the 325 nm laser line at room temperature is less than 10μm, which is larger than the 3-5 μm recombination length of the carrier. Therefore, most of the observed luminescence originates below the sample surface.

However, this long recombination length affects lateral resolution. The presence of the non-radiative centers or centers emitting in a different spectral region, e.g., IR, is responsible for the intensity contrast, which is conveniently useful to distinguish between different regions of the wafer. The dark lines observed mostly run from the facet region (off-center in the wafer) to the wafer edge, with others being circumferential to the facet region (as marked in the box, see discussion below). These all probably correspond to low angle grain boundaries.

In order to confirm these observations, grazing-incidence SWBXT images were recorded from the same samples used for the PL imaging. Examples of comparative images are shown in Fig. 54. Figs. 54(a) and 54(c) are the real color PL images and Figs. 54(b) and 54(d) are their corresponding SWBXT images. The wafer in Fig. 54(a) and 54(b) corresponds to the one discussed in Fig. 53. One can notice that in the SWBXT image, there are a large number of low angle grain boundaries running from the boxed off-center facet to the edge of the wafer. These have a clear one-to-one correspondence to those visible on the PL image. In addition, the boundaries circumferential to the boxed off-center facet observed in Fig. 53(b) also correspond well with the SWBXT image. In Fig. 54(c), a dark area (pointed by arrow) is observed in the PL image, which corresponds to the highly misoriented region (with a high density of low angle grain boundaries). This region corresponds to polytype inclusions, that are also seen in Fig. 54(d). It's easy to detect and distinguish the polytype inclusions and micropipes in PL imaging [Fig. 54(a) and Fig. 54(c)] in comparison to SWBXT imaging [Fig. 54(b) and Fig. 54(d)].

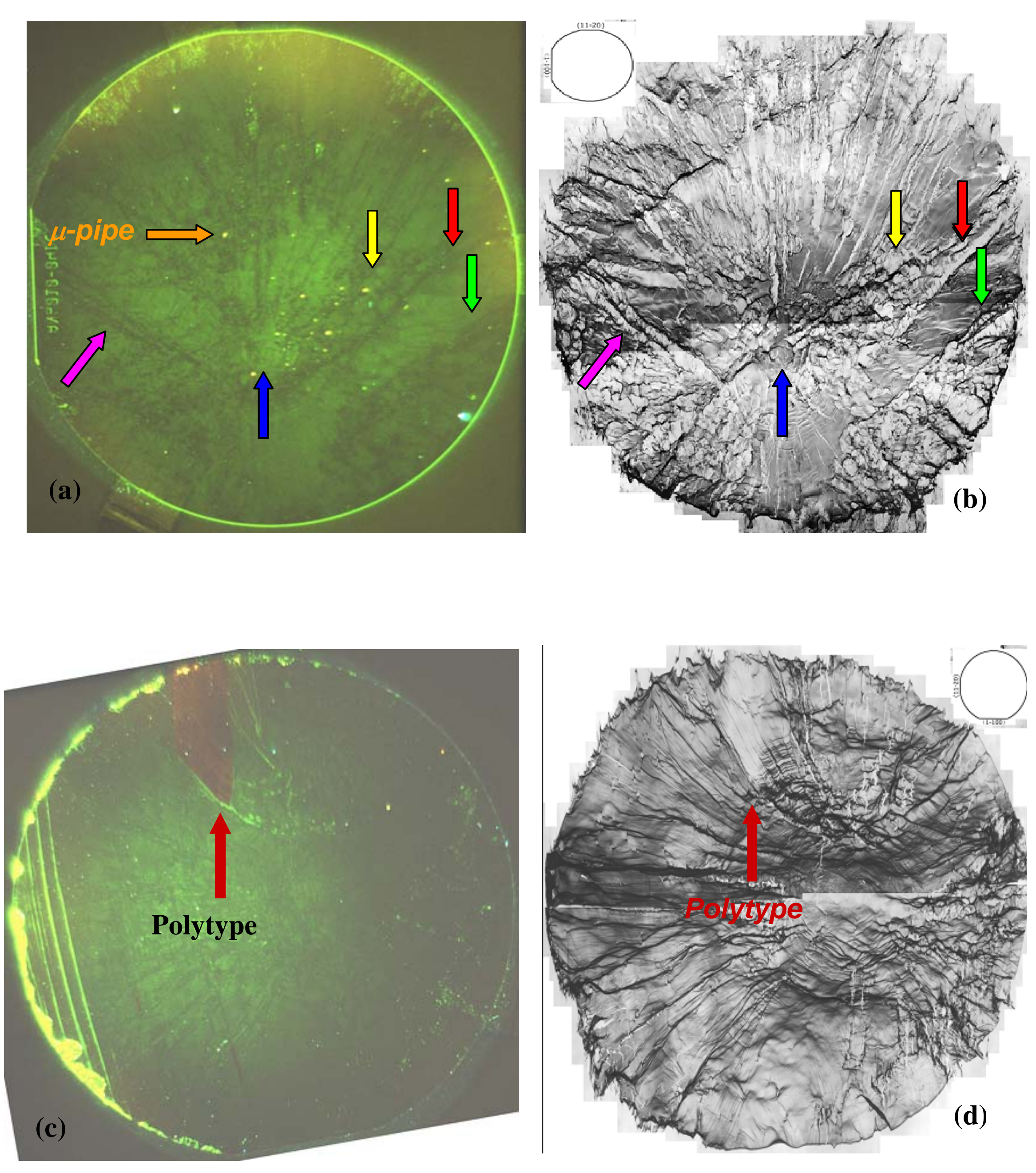

Figure 54: Comparison between PL image and SWBXT. (a) RGB PL image of a 3’’ SiC wafer discussed in Fig. 53; (b) (11-2.12) grazing-incidence SWBXT of the same wafer. (c) PL image of another 3-inch wafer and the corresponding (d) SWBXT.

Figure 55(a) shows a PL image recorded under higher magnification [from the same wafer used for Fig. 54(c) and (d)] with the corresponding SWBXT image being shown in Fig. 55(b). The detailed configuration of the low angle grain boundaries is clearly observed in the PL image. The bright area at the bottom left corner is from a polycrystalline grain, which contains a high density of defects, leading to a high degree of luminescence. Most of the major low angle grain boundary images observed on the PL image correspond well with those on the x-ray topograph, as indicated by the arrows.

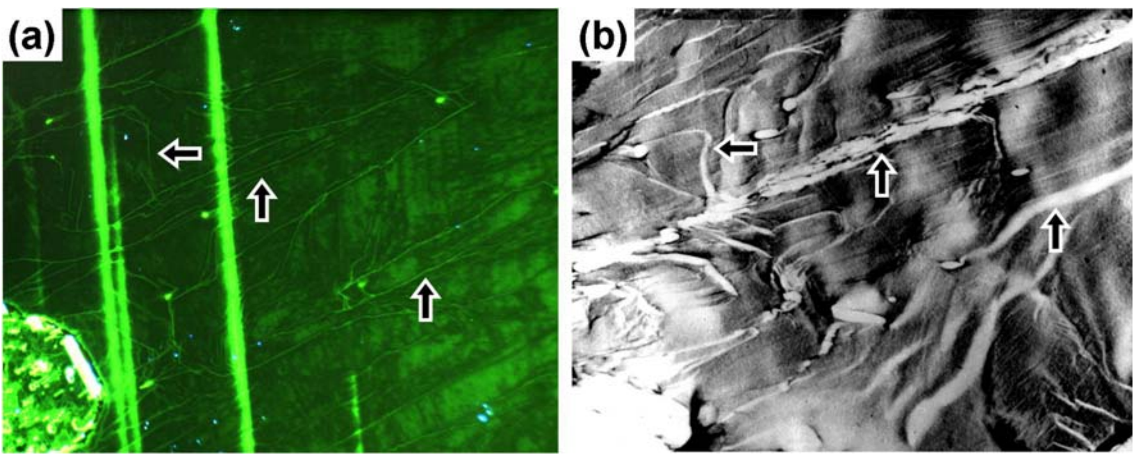

Figure 55: A higher magnification PL image (a) showing the detailed low angle grain boundary configuration and the (b) SWBXT image corresponding to the same area.

The white dots observed on the PL image are likely to be associated with micropipes and several of these have one-to-one correspondence with SWBXT observations. However, detailed SWBXT validation of the sensitivity of PL imaging to micropipes is complicated by the overall level of distortion and misorientation associated

with the low angle grain boundary structures and the fact that some of the micropipes are located in the boundaries. Further work needs to be done for a detailed correlation on lower defect density wafers.

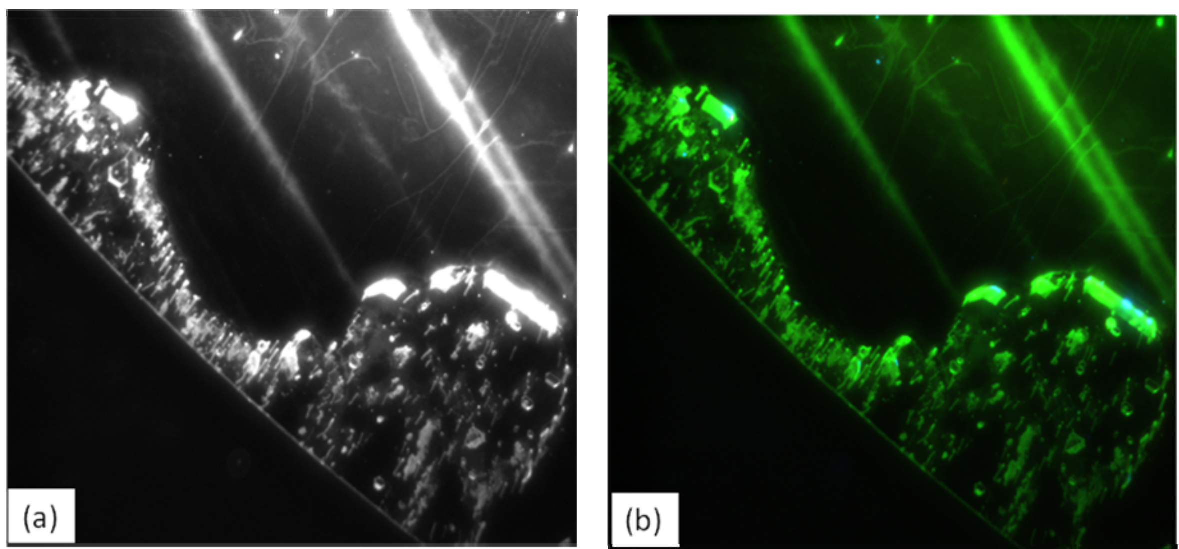

Figure 56: Higher magnification (a) panchromatic scale and (b) Green PL images of a polycrystalline region, which have shown high concentration of micropipes and micro-crystallites.

Higher magnification PL images of these polycrystalline grain, represented in Fig. 56 ((a) panchromatic scale and (b) Green color) clearly show the presence of high concentration of micropipes and micro-crystals on the edges of the wafer. Micropipes and micro-crystals are formed during the process of growth, which are responsible for lowering breakdown voltage. Also observed are the grain boundaries on the surface of the wafer.

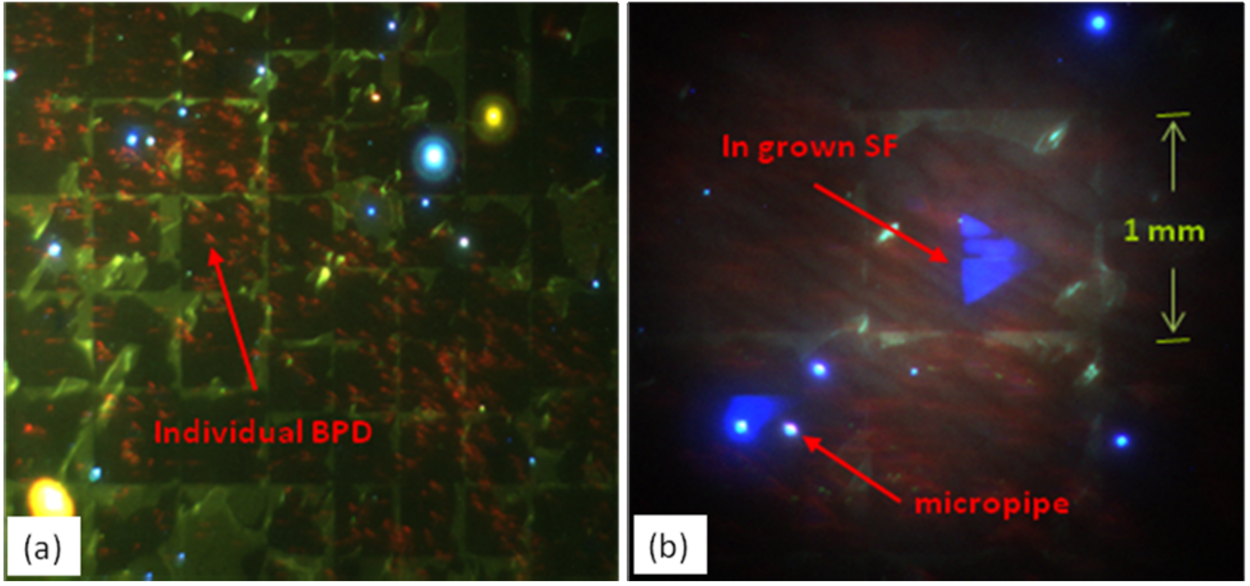

Figure 57: Higher magnification RGB-PL images of a thick 4H-SiC homoepitaxial layer showing the presence of individual SF, BPD, and micropipes.

Also, PL imaging technique allows us to achieve larger optical magnification to detect individual basal plane dislocations (BPD) and ingrown stacking faults (SF), in addition to individual micropipes and micro-crystalline inclusions. The BP dislocations and SF are shown in Fig. 57(a) and 57(b).

In grown stacking faults are created by rigidly shifting the upper half of the crystal with respect to the lower half, in other words slipping of the basal plane. It's clear from the Fig. 57 that a BP dislocation emits red color and SF emits blue color.

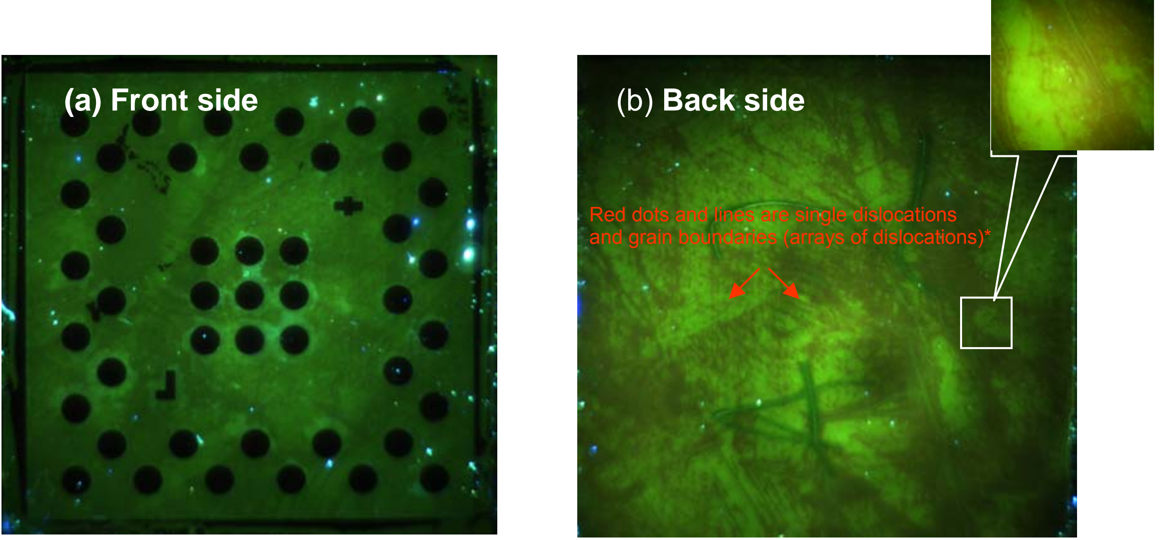

Figure 58: Large area real-color PL imaging of Schottky devices on SiC showing (a) front side and (b) backside.

To understand the nature of the defects and their impact on the performance of the devices, Schottky contacts were fabricated on the SiC. The sample is about 1x1 cm^2 and the diameter of the devices is about 300 μm. Fig. 58 shows real color PL imaging of the front side and back side of the SiC with Schottky contacts. Fig. 58(a) shows the frontside of the SiC with Schottky devices. Similarly Fig. 58(b) shows the backside of the SiC. Due to higher doping concentration, detection of dislocations is more pronounced in the substrate (backside) as seen in Fig. 58(b).

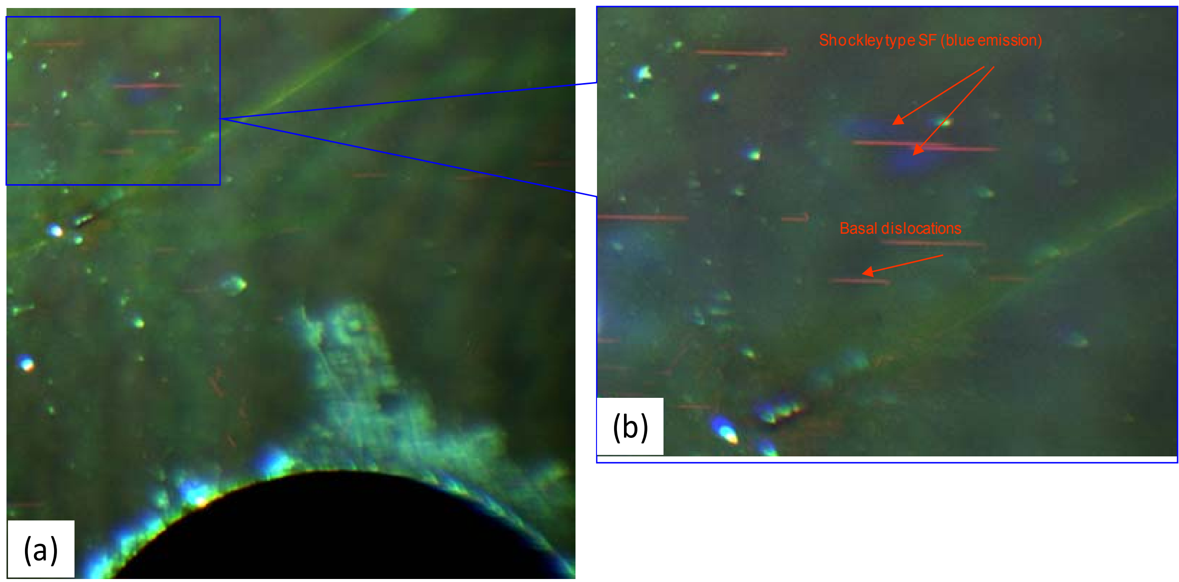

Figure 59: Large area real-color PL imaging (cont.) of defects distribution in device surrounding area taken at front surface.

High magnification of the selected region on the front side of the SiC sample is shown in Fig. 59. Fig. 59(a) was taken using 5x magnification lens of the microscope and Fig. 59(b) using 10x magnification lens of the microscope. The distribution of dislocations like Shockley type SF and basal dislocations can be clearly seen.

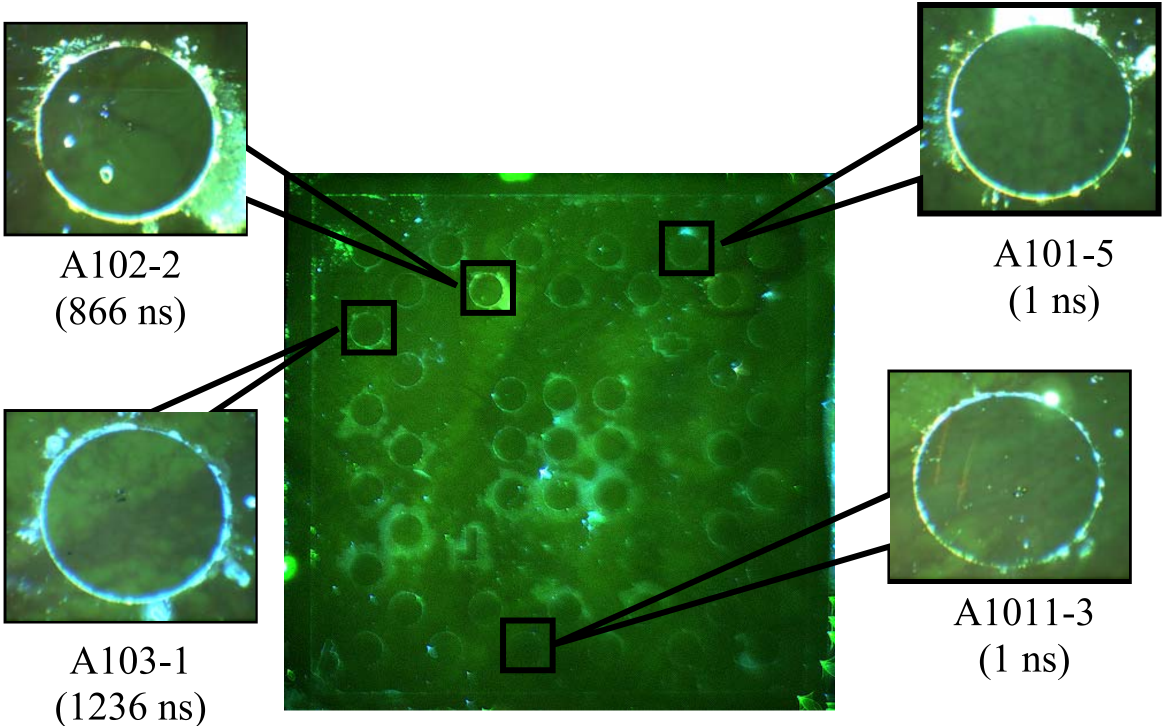

Figure 60: RGB PL imaging of individual devices (after removing the contacts).

Dislocations such as Shockley type SF and basal dislocations were observed around the devices. To see if these defects are present below the surface of the metal contacts, chemical etching was performed to remove these contacts.

Fig. 60 is the real color PL imaging of SiC after the removal of the contacts. Four individual regions of the sample were studied, which showed significant features. Time taken to capture images for two different region was around 1 ns whereas other regions took longer times of 800 – 1300 ns.

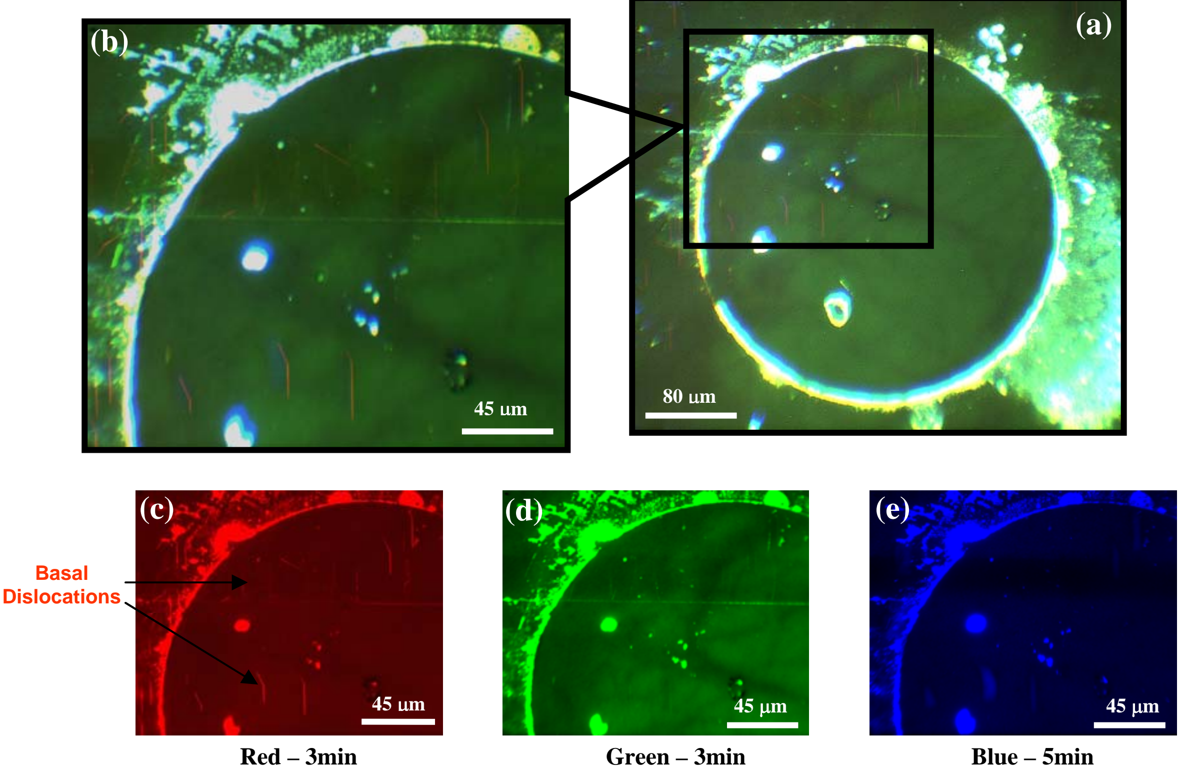

Figure 61: PL imaging of device A102-2 after removing the metal contacts.

High magnification of 10x of one selected region is shown in Fig. 61(a). For a better understanding of the defects much higher magnification of 20x was used, which are shown in Fig.61(b), (c), (d) and (e). Fig. 61(b) shows RGB PL imaging, which shows a row of Shockley type SFs. Also observed is a distribution of few basal dislocations. Fig. 61(c), Fig. 61(d), and Fig. 61(e) show only red emission (capturing time of 3min), green emission (capturing time of 3min), and blue emission (capturing time of 5min), respectively. Red emission imaging clearly shows the basal dislocation. Also Fig. 61(d) shows the grain boundaries.

Before the removal of the metal contacts electron-beam-induced-current (EBIC technique was performed on the region where PL imaging [Fig. 61] was previously acquired. SEM and EBIC images of this region are shown in Fig. 62.

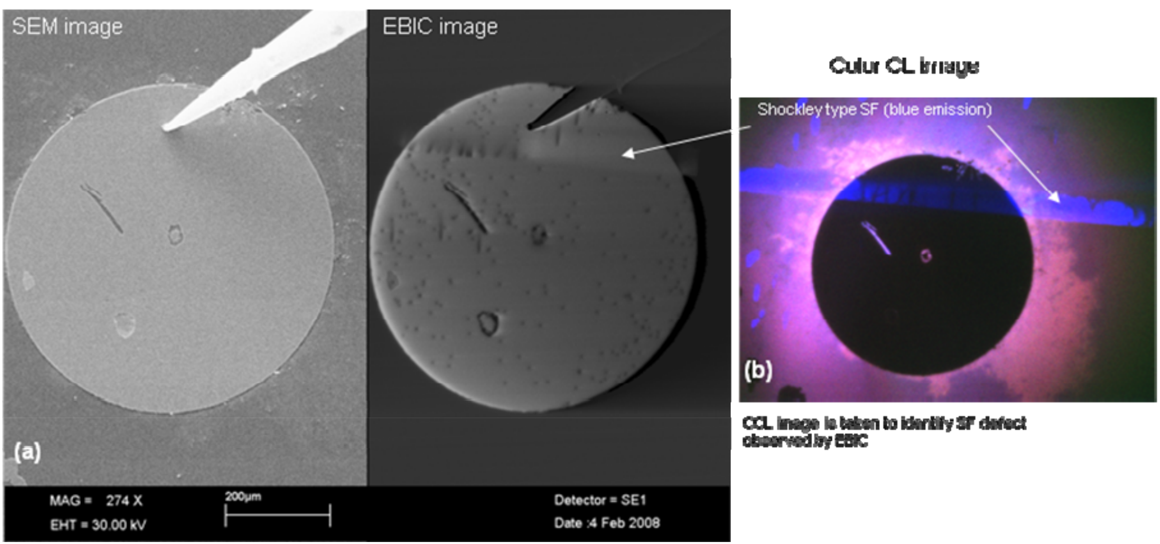

Figure 62: SEM, EBIC and CCL of device A102-2 with metal contacts.

EBIC is obtained from the collection of carriers by internal electric fields. Electrically active defects are observed because of the reduction of current resulting from carrier recombination. Also color Cathodoluminescence (CCL) imaging is shown in Fig. 62(b). The combination of these techniques is extremely powerful to detect and identify defects in devices. Fig. 62(a) shows the SE and EBIC and Fig. 62(b) shows the CCL image of the sample. The EBIC image and the CCL image clearly show the Shockley type SFs.

Fig 63 shows the CCL image of the same region after the removal of the device contacts using chemical etching. This was acquired under 15 KeV and 60 nA condition. This figure shows the region where the Shockley type SF is present.

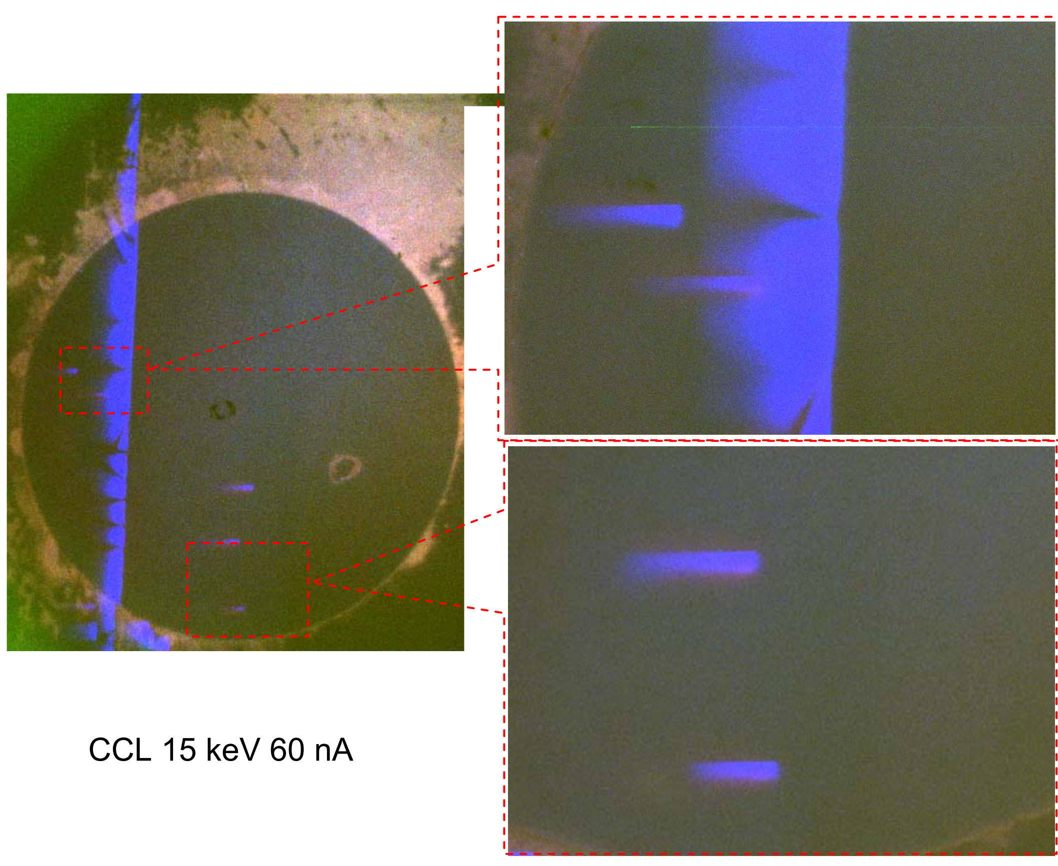

Figure 63: CCL of device A102-2 after removing the metal contacts.

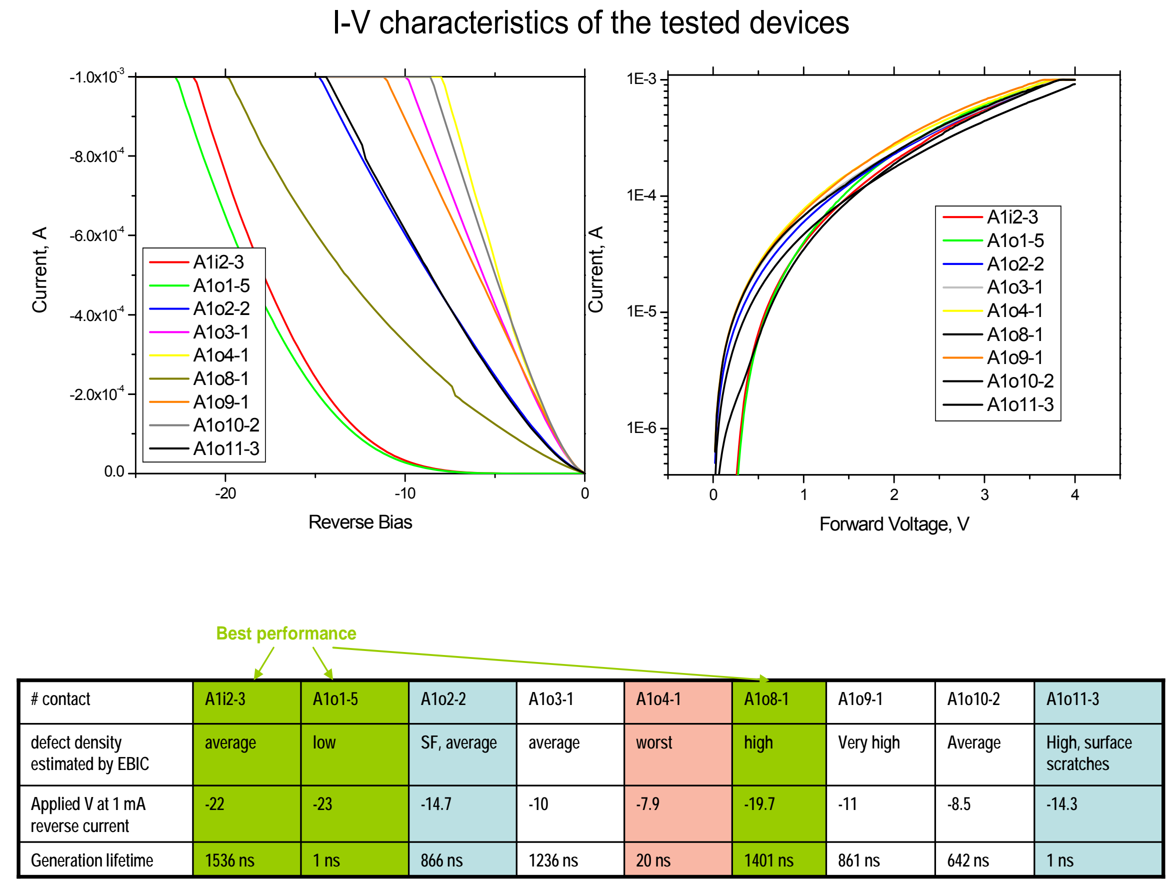

# contact	A1i2-3	A1o1-5	A1o2-2	A1o3-1	A1o4-1	A1o8-1	A1o9-1	A1o10-2	A1o11-3
defect density estimated by EBIC	average	low	SF, average	average	worst	high	Very high	Average	High, surface scratches
Applied V at 1 mA reverse current	-22	-23	-14.7	-10	-7.9	-19.7	-11	-8.5	-14.3
Generation lifetime	1536 ns	1 ns	866 ns	1236 ns	20 ns	1401 ns	861 ns	642 ns	1 ns

Figure 64: Current-voltage (I-V) characterizations of the selected devices.

The current-voltage measurements [shown in Fig. 64] of the chosen device structure did not reveal any noticeable effect due to the presence of the BP dislocations and SF on the electrical properties of the devices. a stable device performance may be achieved in lateral device. However, these defects may play a fundamental role on vertical devices, which requires current flows from top surface to bottom surface of the wafer.

5.3 Summary

Comparative studies of defect microstructures in 4H-SiC wafers have been carried out using photoluminescence (PL) imaging and grazing-incidence Synchrotron White Beam X-ray Topography. PL images of low angle grain boundaries correlate well with SWBXT observations. This validation indicates that PL imaging may provide a rapid way of imaging low angle grain boundary structures in large-scale SiC wafers. While the PL imaging is most probably capable of revealing micropipes, detailed validation of this using SWBXT could not be performed due to the overall level of distortion and misorientation associated with the low angle grain boundary structures and micropipes.

Studies performed on the device structures fabricated on SiC revealed different kinds of defects such as micropipes, SF and BP dislocations. The I-V characterization for few selected devices showed stable device performance and did not reveal any noticeable effect due to the presence of the BP dislocations and SF on the electrical properties of the devices, which may be due to the immobilization of the defects when voltage was applied. The schottky diodes made in this study are one side devices i.e., lateral device operation. For a better understanding of these defects on the performance of bulk high-power devices, transversal devices are required where current flows from top surface to bottom surface of the wafer.

6. CONCLUSIONS AND FUTURE WORK

6.1 Conclusions

Photoluminescence (PL) spectroscopy and imaging have proven to be important tools for the characterization of GaN and SiC materials. A summary of the experimental results of this work based on the optical characterization of these two wide band gap materials is given below:

High crystalline quality of thick unintentionally doped and iron doped freestanding GaN films, grown by Hydride vapor-phase epitaxial (HVPE) process was verified using PL spectroscopy. This was followed by near infrared (NIR) PL measurements, which showed the incorporation of Ga substitutional Fe^{3+} compensating centers. Results of temperature dependent Hall measurements clearly indicated the growth of semi-insulting GaN substrates by this method. High crystallinity and purity of the GaN crystals, grown from solution at moderate temperature and pressure were also confirmed by PL spectroscopy, micro-Raman scattering, and X-Ray diffraction measurements.

Detailed low-temperature PL and high-sensitivity SIMS experiments on freestanding (FS) - HVPE GaN substrates and homoepitaxial films deposited by MBE and organo-metallic vapor-phase epitaxy (OMVPE) clarify the conflict related to the

chemical identification of Si and O as the dominant pervasive shallow donors in GaN films.

PL measurements performed on GaN samples doped with Mg from 10^{17} to 10^{20} cm^{-3} showed a strong emission at ~3.462 eV, which is attributed to annihilation of excitons bound to shallow Mg acceptors. Each sample exhibited a donor acceptor pair (DAP) band (3.27 eV) with no evidence for other deep visible PL bands. Also optically detected magnetic resonance (ODMR) on this emission from the lowest Mg-doped sample revealed the first evidence for the highly anisotropic g-tensor for Mg acceptors in wurtzite GaN.

Optical studies performed on microwave annealed Mg:GaN with AlN cap showed negligible GaN decomposition at temperatures up to ~1500 ^{0}C for both in-situ doped and ion-implanted samples. An increase in the Mg acceptor activation takes place with an increasing annealing temperature. Similar PL measurements performed on Be:GaN films showed the SD-SA (DAP) recombination band is not related to the Be acceptor impurities.

Comparative studies of defect microstructure in 4H-SiC wafers and device structures have been carried out using real color / monochromic PL imaging, grazing-incidence synchrotron white beam X-ray topography, secondary electron microscopy / electron beam induced current, and color cathodoluminescence. Compared to other methods, PL imaging has proven to be the non-destructive and fastest method for the study of defects such as grain boundaries, pits, micropipes, dislocations, and polishing damage.

6.2 Future work

Controlled doping experiments with PL characterization on III-nitride semiconductors should be carried out to identify the bands associated with impurities such as Zn (acts as acceptor) and S (acts as donor).

It is important to develop highly conductive *p*-type GaN/AlGaN layers, which would lead to a drastic improvement in the performance of transistors and laser diodes. Further work in this direction would involve:

- Pulsed PL measurements should be carried out on microwave annealed Mg in-situ doped GaN to understand the nature of near-UVL band. Also microwave annealing of in-situ Mg-doped AlGaN epilayers grown on SiC/sapphire substrates should be performed to verify if high Mg acceptor activation occurs. The effect of microwave annealing on Mg-implanted AlGaN also needs to be carried out, to see if selective area Mg doping can be effectively used to obtain highly conductive p-type AlGaN layers.
- It is also interesting to investigate if co-implantation of Be acceptor with isoelectronic specie phosphorus can minimize Be fast diffusion behavior in GaN. Similar approach yield promising results in case of other III-V compounds like GaAs, InP and InGaAs.

To date PL imaging techniques has been successful used for characterizing SiC. Further extension of the PL imaging technique for characterizing nitride based compounds should be explored. Also, bandedge bandpass filters should be used to obtain information about distribution of carriers across the SiC and nitride based materials.

Appendix 1: Secondary Ion Mass Spectrometry (SIMS)

Secondary ion mass spectrometry, also known as ion microprobe and ion microscope, is one of the most powerful and versatile analytical techniques for semiconductor characterization. Among the beam techniques, it has the highest sensitivity and can detect dopant densities as low as 10^{14} cm^{-3}. It allows simultaneous detection of different elements, has a depth resolution of 1 to 5 nm, and can give lateral surface characterization on a scale of several microns. It is a destructive method since the very act of removing material by sputtering leaves a crater in the sample.

The basic set-up of the SIMS is shown in figure A.1. The ejected material from the sample, during the process of sputtering is analyzed by a mass analyzer. A primary ion beam impinges on the sample and atoms from the sample are sputtered or ejected from the sample. Most of the ejected atoms are neutral and cannot be detected by conventional SIMS, but some are positively or negatively charged. The mass/charge ratio of the ions is analyzed, detected as a mass spectrum, as a count, or displayed on a fluorescent screen.

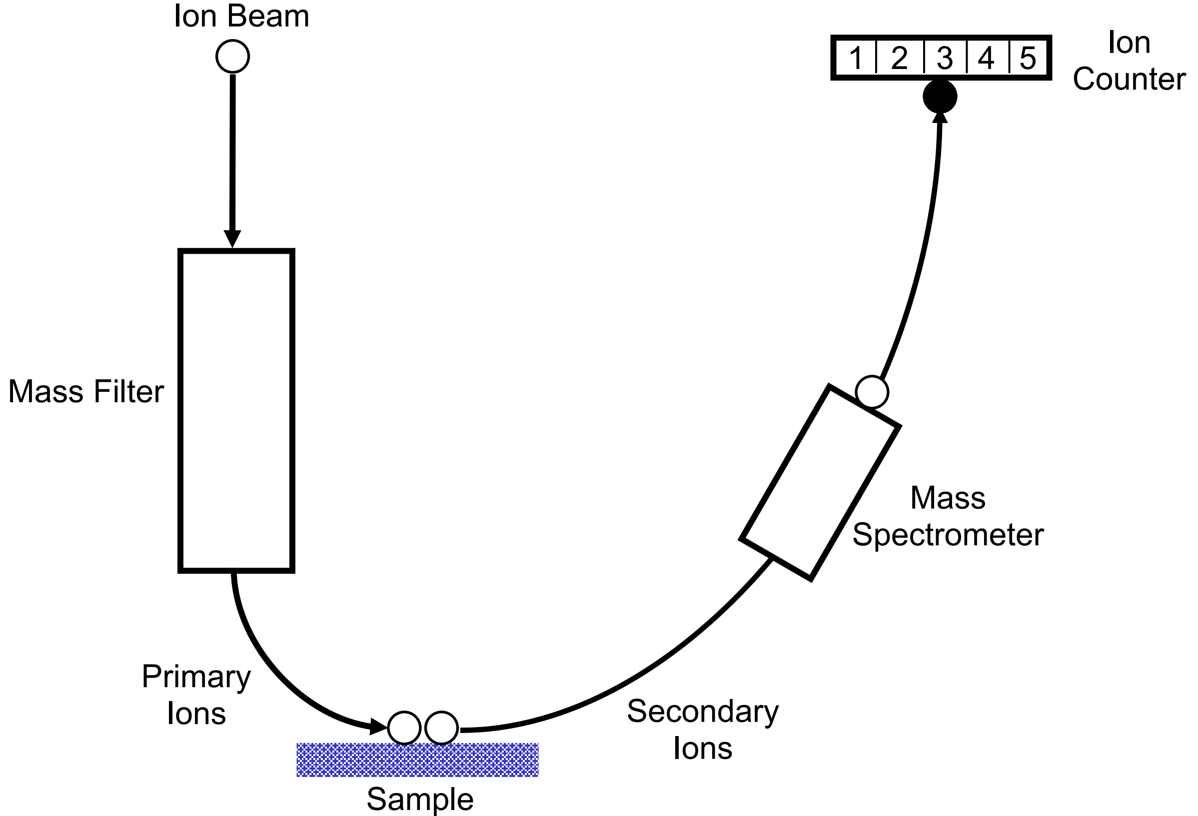

Fig. A.1: A schematic illustration of a typical secondary ion mass spectrometry [Source: D.K. Schroder, *Semiconductor Material and Device Characterization*, IEEE Press, 2006]

Few advantages of SIMS are:

- It's possible to perform small area analysis of around 10 μm.
- It's possible to detect all elements including light elements like H, C, O and N.
- It has an excellent detection limit and depth resolution.

Appendix 2: Atomic Force Microscopy

The atomic force microscope (AFM) or scanning force microscope (SFM) is a very high-resolution type of scanning probe microscope, with demonstrated resolution of fraction of a nanometer, more than 1000 times better than the optical diffraction limit.

The AFM consists of a microscale cantilever with a sharp tip (probe) at its end that is used to scan the specimen surface. The cantilever is typically silicon or silicon nitride with a tip of curvature on the order of nanometers. In tapping mode the cantilever is driven to oscillate up and down at near its resonance frequency by a small piezoelectric element mounted in the AFM tip holder. Due to the interaction of forces acting on the cantilever when the tip comes to the surface, Van der Waals force, electrostatic forces, etc cause the amplitude of this oscillation to decrease as the tip gets closer to the sample. Therefore tapping produced AFM image is based on the force of the oscillating contact of the tip with the sample surface. The piezo motion causes the cantilever to oscillate when the tip does not contact the surface. The oscillating tip is then moved toward the surface until it begins to lightly touch, or tap the surface of the sample. During scanning, the vertically oscillating tip alternately contacts the surface and lifts off, generally at a frequency of 50 to 500 kHz. As the oscillating cantilever contacts the surface intermittently, energy loss caused by the tip contacting the surface reduces the oscillation amplitude that is then used to identify and measure surface features. The tapping mode AFM overcomes the limitations of the conventional scanning modes by alternately placing the tip in contact with the surface to provide high resolution and then lifting the

tip off the surface to avoid dragging the tip across the surface damaging the surface of the sample.

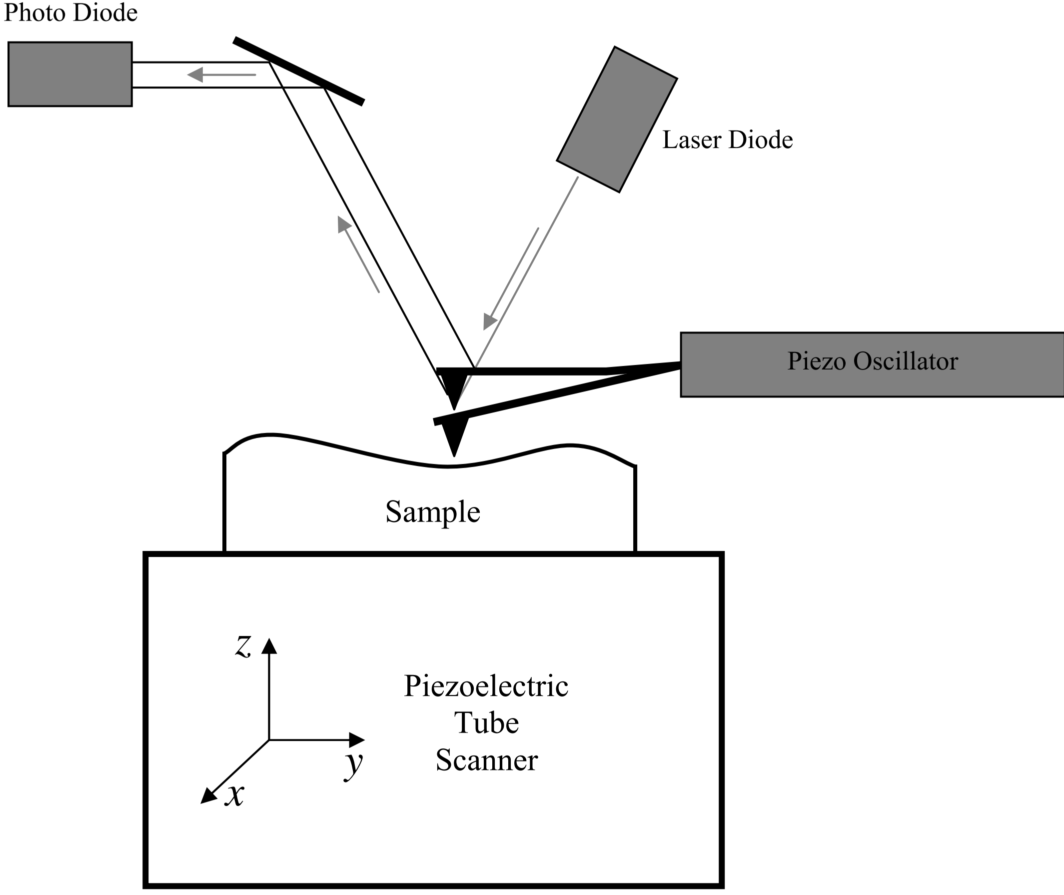

Figure A.2: A schematic illustration of a typical atomic force microscope [Source: D.K. Schroder, *Semiconductor Material and Device Characterization*, IEEE Press, 2006]

Appendix 3: Raman Spectroscopy

Raman spectroscopy (RS) is a spectroscopic technique used in condensed matter physics and chemistry to study vibrational, rotational, and other low-frequency modes in a system. It relies on inelastic scattering, or Raman scattering of monochromatic light, usually from a laser in the visible, near infrared, or near ultraviolet range. The laser light (photons) interacts with other phonons or excitations present in the system, resulting in increase or decrease of frequency of the scattering photon. This variation in the energy (Raman shift) gives information about the phonon modes in the systems.

When a sample is illuminated with a laser beam, light from the illuminated spot is collected with a lens and sent through a monochromator. Wavelengths close to the laser line, due to elastic Rayleigh scattering, are filtered out while the rest of the collected light is dispersed on a detector.

A schematic of a micro-Raman set-up is shown in Fig. A.3. The radiation from a CW laser is focused onto a sample of interest through a microscope objective, so that the incident radiation can be confined to a very small spot (~ 1-5 μm) on the sample. Radiation is introduced into the microscope optical path using an angled dielectric edge filter in the so-called injection-rejection configuration. Collected scattered radiation is delivered to a 0.5 m focal length single spectrometer, which is dispersed by the grating and recorded by a CCD operating typically at -90 ^{0}C. Typically, laser intensity is kept < 5 mW to prevent heating of the sample.

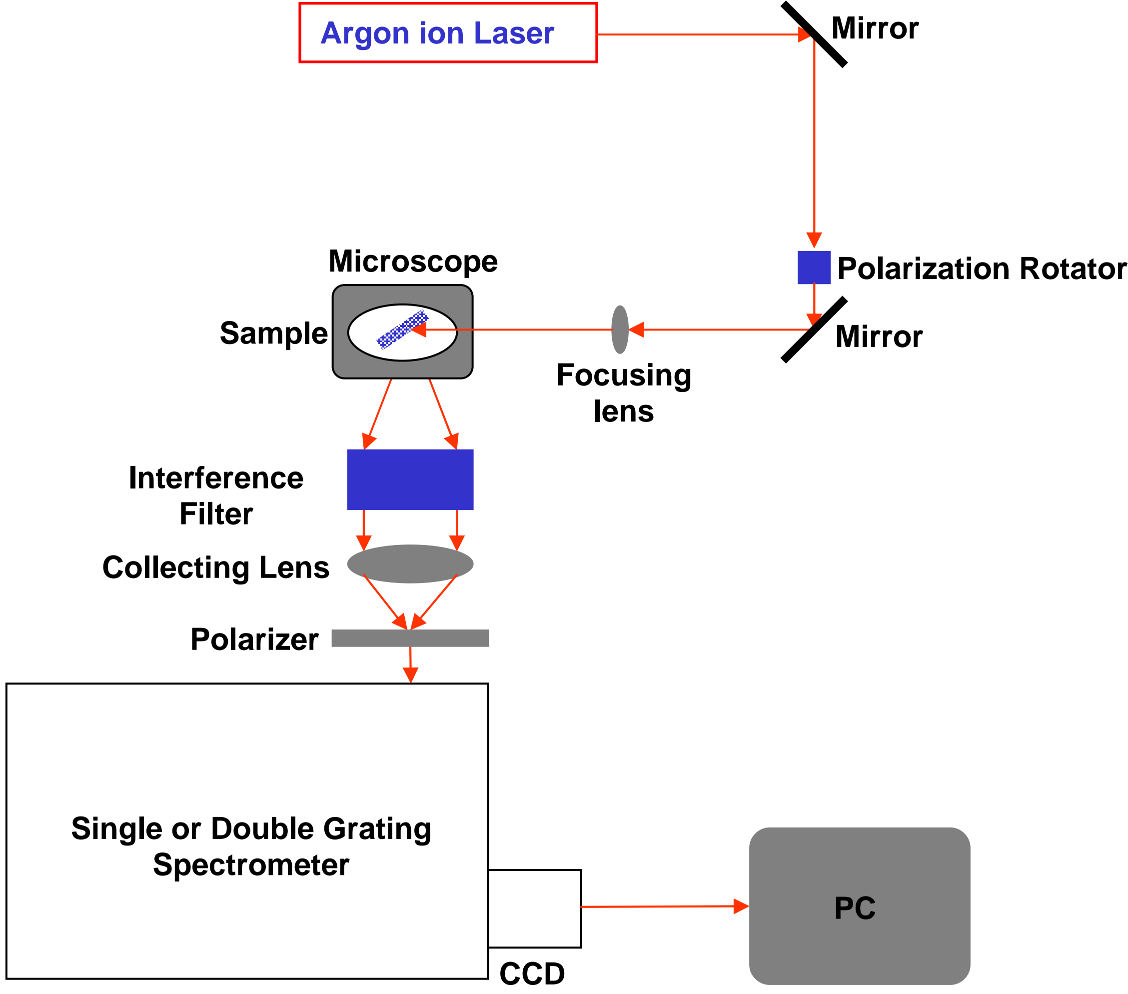

Fig. A.3: Schematic illustration of a typical Raman spectrometer

Few advantages of RS are:

- It's useful for stress measurements in semiconductor samples. Also in the identifaction of crystal structure, and study of defects, doping etc.
- It does not require vacuum environment.

Appendix 5: X-Ray Topography

X-ray topography (XRT) is a non-destructive characterization technique for imaging, by means of X-ray diffraction. XRT is a very powerful tool for the evaluation of crystals for technological applications and for characterizing crystal and thin-film growth and processing.

In X-ray topography, the crystal sample is illuminated by an X-ray beam and images of the diffracted beams are recorded. These images are generally formed from X-ray wave fields interfering with one another inside the crystal. The image from a perfect crystal is usually completely homogeneous. Changes in the image contrast are seen if there are imperfections (dislocations, stacking faults, inclusions, and surface damage) in the crystal.

Accurate structural analysis can be performed using X-ray topography including lattice parameter determination, and stress measurements.

Appendix 6: X-ray Photoelectron Spectroscopy (XPS)

XPS is a quantitative spectroscopic technique that measures the elemental composition, empirical formula, chemical state and electronic state of the elements that exist within a material. XPS spectra are obtained by irradiating a material with a beam of aluminium or magnesium X-rays while simultaneously measuring the kinetic energy (KE) and number of electrons that escape from the top 1 to 10 nm of the material being analyzed. XPS requires ultra-high vacuum conditions.

XPS is used to measure:

- Elemental composition of the surface (1-10 nm)
- Elements that contaminate a surface
- Chemical or electronic state of each element in the surface
- Uniformity of elemental composition across the top surface
- Uniformity of elemental composition as a function of ion beam etching.

Appendix 7: Optically detected magnetic resonance

Optically detected magnetic resonance (ODMR) offers a method to identify residual defects and elucidate the properties of dopants in the samples. The method relies on the spin-dependence of recombination processes and combines PL with electron paramagnetic resonance (EPR). The PL provides very high sensitivity to allow the study of defects at residual levels in state-of-the-art samples. The EPR provides very high resolution to reveal the local symmetry and hyperfine structure of the defect. Also ODMR provides information related to atomic structure and the electronic structure of defects.

Schematic diagram of the ODMR spectrometer is shown in Fig A.4, which consists of an Argon ion laser, 1.1T electromagnet, modulator, 24GHz oscillator, and silicon photo diode (Si PD). The ODMR was detected as the change in the total intensity of PL, which was coherent with the on-off amplitude modulation of 50 mW of microwave power. The samples are studied in a *K*-band (24 GHz) and *Q*-band (35 GHz) spectrometer. For the ODMR, the PL was continuously excited by 3.53 eV radiations with power densities between 0.15 and 1.5 W/cm^2. The emission was detected by a UV-enhanced Si photodiode. The samples were studied under pumped-helium conditions (T ~ 1.6 K) in commercial optical cryostats. The dc magnetic field for the 24-GHz spectrometer was provided by a 9 in. pole-face electromagnet with maximum field of 1.1T.

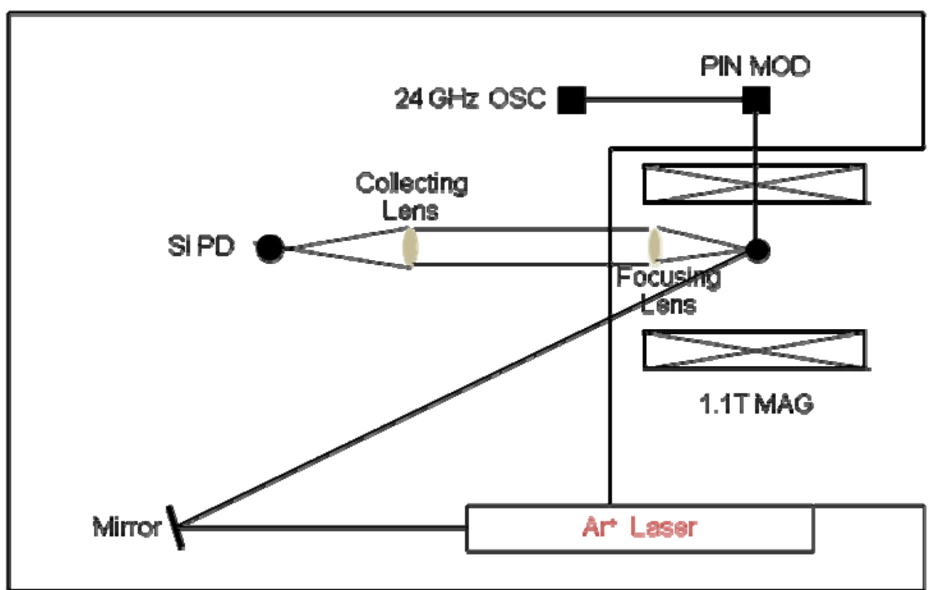

Figure A.4: A schematic diagram of the ODMR spectrometer utilizing an optical table surrounding a 9-inch electromagnet [Source: T.A. Kennedy, and E.R. Glaser, *Chapter 3: Magnetic resonance of epitaxial layers detected by photoluminescence – Semiconductors and semimetals*, Academic press, 2001].

Appendix 8: Microwave annealing technique

A schematic of microwave annealing set-up is shown in Fig. A.5., which consists of three important blocks:

1. Variable frequency microwave power source, which consists of a signal generator and a power amplifier.
2. A heating system, which consists of a tuning and coupling circuit and a heating head.
3. A measurement and control system, which consists of a network analyzer, a computer, an optical pyrometer and other equipment.

Microwave power generated by a variable frequency power source is amplified and then coupled to a sample through the heating head and the temperature is monitored by an infrared pryrometer.

This system can be tuned for efficiently heating the semiconductor samples at variable frequencies. A microwave amplifier is used, which can deliver maximum stable power (~ 150W) at a frequency range of 910-930 MHz. In this step-up the samples are placed in an enclosure chamber made out of microwave transparent, high-temperature stable ceramics (such as boron nitride and mullite), so that the microwaves can only heat the strong microwave absorbing semiconducting films. In this technique, it's possible to directly couple microwave power and heat GaN epilayers grown on sapphire, using SiC susceptor. A SiC susceptor was used in this technique to obtain a uniform distribution of heat across the GaN samples.

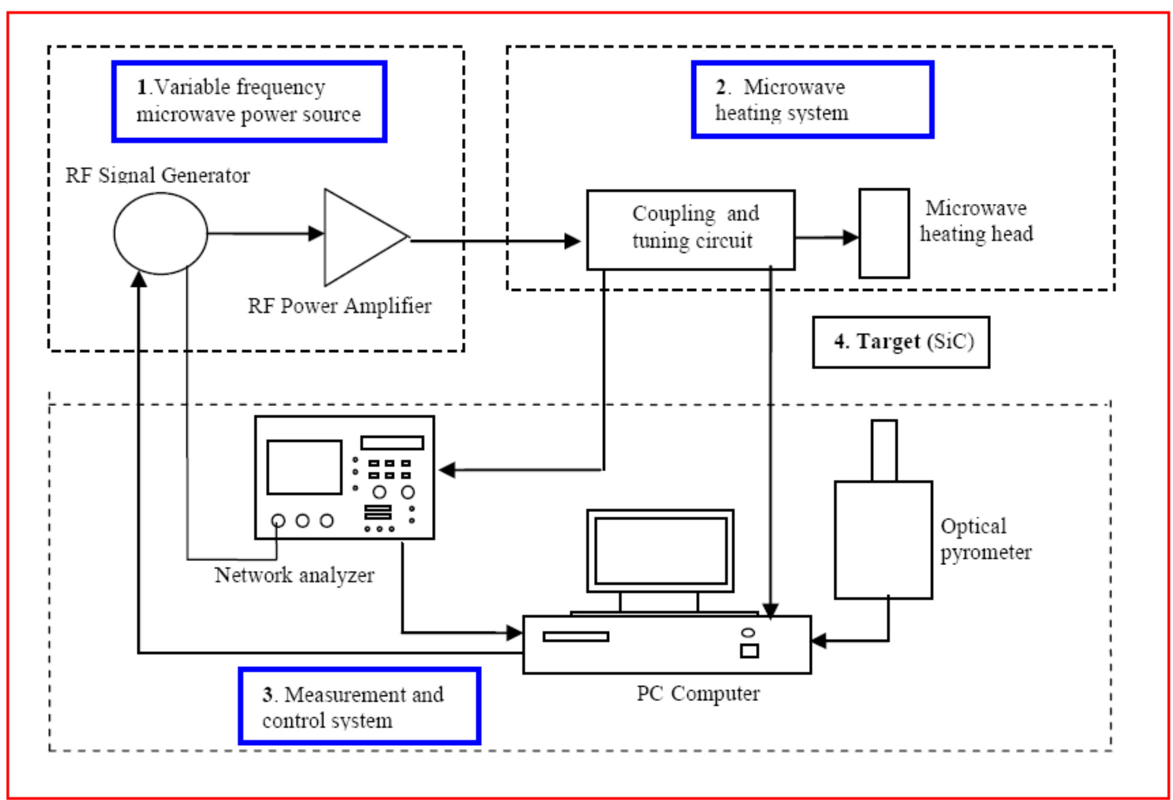

Figure A.5: A schematic diagram of the microwave annealing system [Source: Siddarth G. Sundaresan, *Ultra-fast , high temperature microwave processing of SiC and GaN*, Ph.D. Thesis, 2007].

Advantages of using microwave annealing technique over conventional annealing technique are:

- It can be used for high-temperature processing of wide bandgap semiconductors such as SiC and GaN.
- High temperature annealing of up to 2000 ^{0}C for a very short period of time (in seconds) can be performed.
- It is possible to cool down the sample at the initial rate of 400 ^{0}C/s.

REFERENCES

[1] J.H. Edgar, S. Strite, I. Akasaki, H. Amano, and C. Wetzel (Eds.), *Properties, processing and applications of Gallium nitride and related semiconductors*, Inspec publication,1999.

[2] Gary L. Harris (Ed.), *Properties of Silicon carbide*, Inspec publication, 1995.

[3] K. Takahashi, A. Yoshikawa, and A. Sandhu (Eds.), *Wide bandgap semiconductors*, Springer, 2007.

[4] D.K. Schroder, *Semiconductor material and device characterization*, IEEE press, 2006.

[5] T. Hatakeyama, T. Watanabe, M. Kushibe, K. Kojima, S. Imai, T. Suzuki, T. Shinohe, T. Tanaka, K. Arai, Mater. Sci. Forum **433-436** (2003) 443.

[6] M.A. Reshchikov, and H. Morkoc, J. Appl. Phys. **97** (2005) 061301.

[7] W.J. Moore, J.A. Freitas, Jr., G.C.B. Braga, R.J. Molnar, S.K. Lee, K.Y. Lee, and I.J. Song, Appl. Phys. Lett. **79** (2001) 16.

[8] H.C. Yang, T.Y. Lin, and Y.F. Chen, Phys. Rev. B **62** (2000) 12593.

[9] L.T. Romano, C.G. Van de Walle, J.W. Ager III, W. Gotz, and R.S. Kern, J. Appl. Phys. **87** (2000) 7745.

[10] J.B. Webb, H. Tang, S. Rolfe, and J.A. Bardwell, Appl. Phys. Lett. **78** (1999) 953.

[11] H. Amano, I. Akasaki, T.Kozawa, K. Hiramatsu, N. Sawaki, and K. Ikeda, J. Lumin. **40/41** (1988) 121.

[12] W. Gotz, N.M. Johnson, J. Walker, D.P. Bour, and R.A. Street, Appl. Phys. Lett. **68** (1996) 667.

[13] H. Amano, M. Kito, K. Hiramatsu, and I. Akasaki, Jpn. J. Appl. Phys. **28** (1989) L2112.

[14] F. Gloux, T. Wojtowicz, P. Ruterana, K. Lorenz, and E. Alves, Phys. Stat. Sol. (A) **203** (2006) 2172.

[15] V.E. Borisenko, P.J. Hesketh, *Rapid Thermal Processing of Semiconductors,* (Springer) 1997.

[16] M.A. Sanhez-Garcia, E. Calleja, F.J. Sanchez, F. Calle, E. Monroy, D. Basak, E. Munoz, C. Villar, A. Sanz-Hervas, M. Aguilar, J.J. Serizan, and J.M. Blanco, J. Electron. Mater. **27** (1998) 276.

[17] D.J. Dewsnip, A.V. Andrianov, I. Harrison, J.W. Orton, D.E. Lacklison, G.B. Ren, S.E. Hooper, T.S. Cheng, and C.T. Foxon, Semicond. Sci. Technol. **13** (1998) 500.

[18] B.G. Yacobi, and D.B. Holt, *Cathodoluminescence of inorganic solids*, 1990.

[19] H. Amano, N. Sawaki, I. Akasaki, and Y. Toyoda, Appl. Phys. Lett. **48** (1986) 353.

[20] S. Nakamura, M. Senoh, S. Nagahama, N. Iwasa et al., Appl. Phys. Lett. **72** (1998) 2014.

[21] D.F. Storm, D.S. Katzer, J.A. Roussos, J.A. Mittereder, R. Bass, S.C. Binari, D. Hanser, E.A. Preble, and K.R. Evans, J. Crystal Growth **301** (2007) 429.

[22] T. Mukai, S. Nagahama, T. Kozaki, et al., Phys. Stat. Sol. A **201** (2004) 2712.

[23] D.F. Storm, D.S. Katzer, J.A. Mittereder, S.C. Binari, B.V. Shanabrook, X. Xu, D.S. McVey, R.P. Vaudo, and G.R. Brandes, J. Crystal Growth **281** (2005) 32.

[24] A. Armstrong, C. Poblenz, D.S. Green, U.K. Mishra, J.S. Speck, and S.A. Ringel, Appl. Phys. Lett. **88** (2006) 082114.

[25] R.P. Vaudo, X. Xu, A. Salant, J. Malcarne, and G.R. Brandes, Phys. Stat. Sol. (a) **200** (2003) 18.

[26] R. Heitz, P. Maxim, L. Eckey, P. Thurian, A. Hoffmann, I. Broser, K. Pressal, and B.K. Meyer, Phys. Rev. B **55** (1997) 4382.

[27] N.I. Kuznetsov, A.E. Nikolaev, A.S. Zubrilov, Y.V. Melnik, and V.A. Dmitriev, Appl. Phys. Lett. **75** (1999) 3138.

[28] J.A. Freitas, Jr., J.G. Tischler, J-H. Kim, Y. Kumagai, and A. Koukitu, J. Crystal Growth **305** (2007) 403.

[29] D. Hanser, L. Liu, E.A. Preble, D. Thomas, and M. Williams, Mat. Res. Soc. Symp. Proc. **798** (2004) Y2.1.1.

[30] T. Paskova, R. Kroeger, S. Figge, D. Hommel, V. Darakchieva, B. Monemar, E. Preble, A. Hanser. N.M. Williams, and M. Tutor, Appl. Phys. Lett. **89** (2006) 051914.

[31] J.A. Freitas, Jr., W.J. Moore, B.V. Shanabrook, G.C.B. Braga, S.K. Lee, S.S. Park, and J.Y. Han, Phys. Rev. B **66** (2002) 233311.

[32] J. Baur, K. Maier, M. Kunzer, U. Kaufmann, J. Schneider, H. Amano, I. Akasaki, T. Detchprom, and K. Hiramatsu, Appl. Phys. Lett. **64** (1994) 857.

[33] Y. Kumagai, K. Takemoto, H. Murakami, and A. Koukitu, Jpn. J. Appl. Phys. **44** (2005) L1072.

[34] X. Xu, R.P. Vaudo, C. Loria, A. Salant, G.R. Brandes, and J. Chaudhuri, J. Crystal Growth **246** (2002) 223.

[35] M. Hermann, D. Gogova, D. Siche, M. Schmidbauer, B. Monemar, M. Stutzmann, and M. Eickhoff, J. Crystal Growth **293** (2006) 462.

[36] K. Motoki, T. Okahisa, S. Nakahata, N. Matsumoto, H. Kimura, H. Kasai, K. Takemoto, K. Uematsu, M. Ueno, Y. Kumagai, A. Koukitu, H. Seki, J. Cryst Growth **237–239** (2002) 912.

[37] S.S. Park, I.W. Park, and S. H. Choh, Jpn. J. Appl. Phys. **39** (2000) L1141.

[38] M. K. Kelly, R.P. Vaudo, V.M. Phanse, L.Gorgens, O. Ambacher, and M. Stutzmann, Jpn. J. Appl. Phys. **38** (1999) L217.

[39] T. Paskova, P.P. Paskov, E.M. Goldys, E. Valcheva, V. Darakchieva, U. Sodervall, M. Godlewski, M. Zielinski, S. Hautakangas, K. Saarinen, C.F. Carlstrom, Q. Wahab, B. Monemar, J. Cryst Growth **273** (2004) 118.

[40] S. Porowski, and I. Grzegory, J. Crystal Growth **178** (1997) 174.

[41] M. Aoka, H. Yamane, M. Shimada, S. Sarayama, F.J. DiSalvo, J. Cryst Growth **242** (2002) 70.

[42] Y.T. Song, X.L. Chen, W.J. Wang, W.X. Yuan,Y.G. Cao, X.Wu, J. Cryst Growth **260** (2004) 327.

[43] B.N. Feigelson, R.L. Henry, J. Crystal Growth **281** (2005) 5.

[44] B.N. Feigelson, R.M. Frazier, M. Twigg, J. Crystal Growth **305** (2007) 399.

[45] J.A. Freitas Jr., J. Cryst. Growth **281** (2005) 168.

[46] K. Kornitzer, T. Eber, K. Thonke, R. Sauer, C. Kirchner, V. Schwegeler, M. Kamp, M. Leszczynski, I. Grzegory, S. Porpwski, Phys. Rev. B **60** (1999) 1471.

[47] R. Liu, A. Bell, F.A. Ponce, C.Q. Chen, J.W Yang, M.A. Khan, Appl. Phys. Lett. **86** (2005) 021908.

[48] P.P. Paskov, R. Schifano, B. Monemar, T. Paskova, S. Figge, D. Hommel, J. Appl. Phys. **98** (2005) 093519.

[49] L. Bergman, M. Dutta, R.J. Nemanich, Raman Scattering in Materials Science, Springer Series, Eds. W.H. Weber, R. Merlin, **42** (2000) 273.

[50] L. Bergman, D. Alexon, P.L. Murphy, R.J. Nemanich, M. Dutta, M.A. Stroscio, C. Balkas, H. Shin, R.F. Davis, Phys. Rev. B **59** (1999) 12977.

[51] T. Suski, P. Perlin, H. Teisseyre, M. Leszcynski, I. Grzegory, J. Jun, M. Bockowski, S. Porowski, T.D. Moustakas, Appl. Phys. Lett. **67** (1995) 2188.

[52] P. Prystawko, M. Leszcynski, B. Beaumont, P. Gibart, E. Frayssinet, W. Knap, P. Wisniewski, M. Bockowski, T. Suski, S. Porowski, Phys. stat. sol. (b) **210** (1998) 437.

[53] R.P. Vaudo, V.M. Phanse, X. Wu, Y. Golan, J.S. Speck, in: Proceedings of the Second International Conference on Nitride Semiconductors, 1997, p. 442.

[54] S. Porowski, J. Crystal Growth **189-190** (1998) 153.

[55] S.S. Park, I1.-W. Park, S.H. Choh, Jpn. J. Appl. Phys. **38** (1999) L217.

[56] T. Paskova, V. Darakchieva, P.P. Paskov, U. Söderwall, B. Monemar, J. Crystal Growth **246** (2002) 207.

[57] M.K. Kelly, R.P. Vaudo, V.M. Phanse L. Gögens, O. Ambacher, M. Stuzmann, Jpn. J. Appl. Phys. **38** (1999) L217.

[58] K. Lee, K. Auh, J. Appl. Phys. **40** (2001) L13.

[59] M. Murthy, J.A. Freitas Jr., J. Kim, E.R. Glaser, D. Storm, J. Cryst. Growth **305** (2007) 393.

[60] J.A. Freitas Jr., G.C.B. Braga, W.J. Moore, J.G. Tischler, J.C. Culbertson, M. Fatemo, S.S. Park, S.K. Lee, Y. Park, J. Crystal Growth **231** (2001) 322.

[61] J.-H.Kim, JA. Freitas Jr., P.B. Klien, S. Jang, F. Ren, S.J. Pearton, Electrochem. Solid-State Lett. **8** (2005) G345.

[62] J.A. Freitas Jr., W.J. Moore, B.V. Shanabrook, G.C.B. Braga, S.K. Lee, S.S. Park, J.Y. Han, D.D. Koleske, J. Crystal Growth **246** (2002) 307.

[63] E.R. Glaser, W.E. Carlos, G.C.B. Braga, J.A. Freitas, Jr., W.J. Moore, B.v. Shanabrook, R.L. Henry, A.e. Wickenden, and D.D. Koleske, Phys. Rev. B **65** (2002) 085312.

[64] G.N. Aliev, S. Zeng, J.J. Davies, D. Wolverson, S.J. Bingham, P.J. Parbrook, T. Wang, Phys. Rev. B **71** (2005) 195204.

[65] A.V. Malyshev,I.A. Merkulov, A.V. Rodina, Physics of the Solid State **40** (1998) 917.

[66] The SIMS measurements were performed by Charles Evans and Associates (West), Inc.

[67] D.F. Storm,D.S. Katzer, S.C. Binari, E.R. Glaser, B.V. Shanabrook, J.A. Roussos, Appl. Phys. Lett. **81** (2002) 3819.

[68] R. Stepniewski,A. Wysmolek, M. Potemski, J. Lusakowski, k. Korona, K. Pakula, J.M. Baranowski,G. Martinez, P. Wyder, I. Grzegory, S. Porowski, Phys. Stat. Sol. (b) **210** (1998) 373.

[69] R. Dingle, M. Ilegems, Solid State Commun. **9** (1971) 175.

[70] E.R. Glaser,T.A. Kenedy, J.A. Freitas Jr., B.V. Shanbrook, A.E. Wickenden, D.D. Koleske, R.L. Henry, H. Obloh, Physica B **273-274** (1999) 58.

[71] E.R. Glaser,J.A. Freitas Jr., B.V. Shanabrook, D.D. Koleske, S.K. Lee, S.S. Park, J.Y. Han, Phys. Rev. B **68** (2003) 195201.

[72] S.J. Pearton, C.R. Abernathy, F. Ren, Gallium *Nitride Processing for Electronics, Sensors, and Spintronics (*Springer-Verlag, London) 2006 .

[73] S.O. Kucheyev, J.S. Williams, S.J. Pearton, Mater. Sci. Engg. **33** (2001) 51.

[74] A.V. Davydov, W.J. Boettinger, U.R. Kattner, T.J. Anderson, Phys. Stat. Solidi B **188** (2001) 407.

[75] V.E. Borisenko, P.J. Hesketh, *Rapid Thermal Processing of Semiconductors,* Springer, 1997.

[76] S.J. Pearton, J.C. Zolper, R.J. Shul, F. Ren, J. Appl. Phys. **86** (1999) 1.

[77] S-J Chang, Y-k Su, T-L Tsai, C-Y Chang, C-H Chiang, C-S Chang, T-P Chen, K-H Huang, Appl. Phys. Lett. **78** (2001) 312.

[78] S.G. Sundaresan, J.A. Schreifels, Y-L Tian, M.C. Wood, K.A. Jones, A.V. Davydov,M.V. Rao, J. Electron. Mater. **36** (2007) 324.

[79] S.G. Sundaresan, J.A. Schreifels, Y-L Tian, M.C. Ridgway, J.J. Kopanski, M.V. Rao, J. Appl. Phys. **101** (2007) 073708.

[80] S.G. Sundaresan, N.A. Mahadik, S.B. Qadri, J.A. Schreifels, E. Gomar-Nadal, J. Zhang, M.V. Rao, Solid-State Electron. **52** (2008) 140.

[81] C.R. Eddy Jr., R.T. Holm, R.L. Henry, M.E. Twigg, N.D. Bassim, L.M. Shirey, O.J. Glembocki, J.C. Culbertson, F.K. Perkins, M.C. Peckerar, Y. Ngu, F. Yan, Appl. Phys. Lett. **90** (2007) 162101.

[82] S.S. Hullavarad, R.D. Vispute, B. Nagaraj,V.N. Kulkarni, S Dhar, T. Venkatesan, K.A. Jones, M. Derenge, T. Zheleva, M.H. Ervin, A. Lelis, L.J. Scozzie, D. Habersat, A.E. Wickenden, L.J. Currano, M. Dubey, J. Electron. Mater. **35** (2007) 777.

[83] R. Dalmau, R. Collazo, S. Mita, Z. Sitar, J. Electron. Mater. **36** (2007) 414.

[84] M.E. Levinshtein, S. Rumyantsev, M.S. Shur (eds.), *Properties of Advanced Semiconductor Materials: GaN, AlN, InN, SiC, SiGe,* Wiley-Interscience, 2001.

[85] B.P. Gila, S.J. Pearton, et al. Proc. Electrochem. Soc. **4** (2005) 247.

[86] C. Kumtornkittikul, M. Sugiyama, Y. Nakano, J. Electron. Mater. **35** (2006) 744.

[87] M.G. Ganchenkova, R.M. Nieminen, Phys. Rev. Lett. **96** (2006) 196402.

[88] Y. Sun, L.S. Tan, S.J. Chua, S. Prakash, Mat. Res. Soc. Symp. Proc. **595** (200) W3.82.1.

[89] Y. Nakano, T. Jimbo, Appl. Phys. Lett. **81** (2002) 3990.

[90] K. Lee, B.L. VanMil, M. Luo, L. Wang, N.C. Giles, and T.H. Myers, Phys. Stat. Solidi C **2** (2005) 2204.

[91] T. Ohno, H. Yamoguchi, S. kuroda, K. Kajima, T. Suzuki, K. Arai, J. Crystal Growth **260** (2004) 209.

[92] K. Koga, Y. Fujikawa, Y. Ueda, T. Yamaguchi, Springer Proc. Phys. **71** (1992) 96.

[93] H. Chen, B. Raghothamachar, W. Vetter, M. Dudley, Y. Wang, B. Skromme, Mater. Res. Soc. Symp. Proc. **911** (2006) B05-24.

[94] R.E. Stahlbush, M. Fatemi, J.B. Fedison, S.D. Arthur, L.B. Rowland, S. Wang, J. Elec. Mater. **31** (2002) 370.

[95] Y. Chen, G. Dhanaraj, w. Vetter, R. Ma, M. Dudley, Mater. Sci. Forum **556-557** (2007) 231.

[96] S. Ha, M. Skowronski, H. Lendenmann, J. Appl. Phys. **96** (2004) 393.

[97] H. Lendenmann, F. Dahlquist, N. Johansson, R. Soderholm, P. A. Nilsson, J. P. Bergman, P. Skytt, Mater. Sci. Forum **353–356** (2001) 727.

CURRICULUM VITAE

Madhu H. Gowda was born in Bangalore, India. She received her Bachelors degree in Computer Science and Engineering from Bangalore University in June 2002. She then received her Masters in Electrical Engineering from Tuskegee University in June 2005 and in December 2008, she received her Ph.D. in Electrical and Computer Engineering from George Mason University.